56

A Feasibility Study of Solidification Front Monitoring via Tomographic Imaging

by

Mark Matthew Hytros

S.B. Massachusetts Institute of Technology (1994)

Submitted to the Department of Mechanical Engineering
in partial fulfillment of the requirements for the degree of

Master of Science

at the

MASSACHUSETTS INSTITUTE OF TECHNOLOGY

June 1996

Author .....
Department of Mechanical Engineering
March 25, 1996

Certified by .....
Jung-Hoon Chun
Edgerton Associate Professor of Mechanical Engineering
Thesis Supervisor

Accepted by .....
Ain A. Sonin
Chairman
Departmental Committee on Graduate Students

A Feasibility Study of Solidification Front Monitoring via Tomographic Imaging

by

Mark Matthew Hytros

Submitted to the Department of Mechanical Engineering
on March 25, 1996, in partial fulfillment of the
requirements for the degree of
Master of Science

Abstract

A feasibility study was performed to assess the use of γ-ray computed tomography (CT) as a method of distinguishing the liquid and solid phases of a metal during solidification. Since the liquid and solid phases of a metal differ in density from 4% to 12%, CT may be a viable method of differentiating the two states. The motivation of this work is the development of a real-time sensor to detect and monitor the solidification front in the continuous casting process.

A preliminary experiment was conducted to examine the attenuation behavior of γ-rays through solidifying metal. The test material was pure tin melted in a crucible. By means of active heating and cooling, the tin existed in both liquid and solid phases with a stable solidification front. The location of the solidification front was monitored using thermocouples. A photon beam of γ-rays from a collimated Co^{60} radioisotope was projected through the crucible, encountering a combination of liquid and solid tin. The number of photons transmitted through the crucible were measured over a 100 second time interval. Ten experiments were performed, with each experiment having the photon beam pass through a different fraction of liquid and solid tin. Using the measured photon count and the material properties of the experiment, the liquid tin thickness through which the photon beam passed was calculated and compared to the liquid tin thickness based on the thermocouple measurements. The two techniques compared favorably, validating the use of radiation transmission measurements to determine the location of the solidification front.

A first-generation CT system for reconstructing two-dimensional images of solidifying tin was developed. The performance of the CT system was evaluated by reconstructing images of objects with known geometries and densities. A maximum spatial resolution of 3.2 mm and a contrast resolution of 6% were achieved. CT experiments were performed on an actively heated and cooled crucible filled with pure tin. The tin existed in both liquid and solid phases, with the solidification front position tracked by thermocouples. The crucible was scanned and a CT image was reconstructed. The images of the two-phase tin object show a distinct low density core surrounded by a high density region. The interface of the two areas is the solidification front. Much temperature fluctuation occurred within the crucible during data acquisition, resulting in a time-averaged image. Consequently, the solidification front position could not be adequately confirmed with the thermocouple measurements. However, the image of the averaged liquid/solid interface appears to be genuine since the surrounding materials are clearly detected and previous baseline tests of the CT system found it to be working properly.

Thesis Supervisor: Jung-Hoon Chun
Title: Edgerton Associate Professor of Mechanical Engineering

Acknowledgments

The most formidable part of this entire thesis is thanking all of the individuals who, in some way, shape, or form, have contributed to its completion. First, I would like to thank Professor Jung-Hoon Chun for giving me the opportunity to begin this research project. I very much enjoy working under his guidance, and hope that I will continue to be a valuable contributor to his lab.

I would like to thank all of the organizations who have funded this project. These include the National Science Foundation, the American Iron and Steel Institute and the member companies, the Aluminum Company of America, the Department of Energy and the Idaho National Engineering Laboratory – University Consortium, and the MIT Manufacturing Institute and Dr. Andre Sharon.

I would like to thank the various MIT faculty and staff who have helped me on this project, including Dr. Richard Lanza, Dr. Nannaji Saka, Jeff DiTullio, Fred Cote, Gerry Wentworth, Kevin Baron, Norman Berube, Bob Kane, Leanna Harada, Julie Drennan, and Leslie Regan. I would like to thank my various outside contacts on the project, including Julian Sparrow of the National Institute of Standards and Technology.

I would like to thank the students of LMP for their knowledge, help, and support, including Pyongwon Yim, Chen-An Chen, Tom Nowak, Sukyoung Chey, Ho-Young Kim, Jeanie Cherng, and Wes Williams. I would like to thank my partner-in-crime on this project, DongSik Kim – I will always remember the Million Dollar Cowboy Bar, Jackson Hole, Wyoming. I would like to thank my roommate, Terence Y. Chow, without whom I would have no one to appreciate NBC Must-See-TV and TBS James Bond marathons with. I would like to thank the 1995-96 Chicago Bulls for kicking ass. I would like to thank ESPN, Sportscenter, Dan Patrick, and Keith Olbermann, for giving me something to do between 11pm and midnight.

I would like to thank God for giving me the strength to persevere. Finally, I would like to thank my parents, Lottie and Richard Hytros, for all of their continued support, encouragement, kindness, and love.

I believe that man will not merely endure: he will prevail. He is immortal, not because he alone among creatures has an inexhaustible voice, but because he has a soul, a spirit capable of compassion and sacrifice and endurance.

-William Faulkner

Did you exchange a walk-on part in the war for a lead role in a cage?

-Pink Floyd

Nomenclature

Symbol	Definition
α	Photon energy to electron rest-mass energy ratio
BW	Photon beam width
$BW_{crossover}$	Photon beam width at the crossover point
c	Speed of light
CONTRAST%	Contrast resolution
D	Detector size or collimation
E	Electromagnetic radiation photon energy
E_{rm}	Electron rest-mass energy
$f(x,y)$	Distribution of linear attenuation coefficients within an object
$g(s,\theta)$	Line integral measurement
$g_\theta(s)$	Line integral measurement for a given view angle
h	Planck's constant
I	Transmitted photon intensity; transmitted photon count
I'	Transmitted photon count through test-object and all solid tin for an incident I_o
I_o	Incident photon intensity; incident photon count
i	Current
κ	Probability, per atomic cross-section, of pair production
λ	Radioactivity decay constant
L	Distance from source to detector
L	Total traversed path length through tin
L_{liq_γ}	Traversed path length through liquid tin calculated by the γ-ray attenuation method
$L_{liq_{TC}}$	Path length of liquid tin calculated by the location of the solidification front
L_{liquid}	Traversed path length through liquid tin
L_{solid}	Traversed path length through solid tin
m_o	Electron rest-mass
μ	Mass attenuation coefficient
$\mu_{background}$	Linear attenuation coefficient of background material
μ_{exp}	Experimentally determined mass attenuation coefficient for tin at the mean Co^{60} energy
μ_o	Linear attenuation coefficient
μ_{object}	Linear attenuation coefficient of object of interest
μ_{other}	Lumped mass attenuation coefficient of non-tin materials in the test-object
μ_{tin}	Mass attenuation coefficient of tin
ν	Frequency of electromagnetic radiation
$\bar{n}$	Mean value of a distribution
n_{count}	Number of photons incident over a given period
N	Number of radioactive nuclei in a source
N	Number of atoms, per unit volume, of material traversed by a photon

Symbol	Definition
N_s	Number of transverse measurements
N_θ	Number of view angles
ω	Fourier frequency variable
P	Photon non-interaction probability
p	Photon non-interaction probability per unit length
$p_\theta(x,y)$	Filtered projection data for a given view angle
PDF	Probability distribution function
Q	Charge
$q(s)$	Filtering operator for filtered back projection
r_o	Classical electron radius
ρ	Material density
ρ_{liquid}	Density of liquid tin
ρ_{other}	Lumped density of non-tin materials in the test-object
ρ_{solid}	Density of solid tin
s	Projection coordinate position
S	Source size or collimation
SNR	Signal–to–noise ratio
σ	Probability, per atomic cross-section, of Compton Scattering
σ	Standard deviation of a distribution
t	Time
t_c	Photon detection time
T_{high}	Temperature of first thermocouple in liquid tin
T_{low}	Temperature of first thermocouple in solid tin
T_{melt}	Melting temperature of pure tin at standard temperature and pressure
τ	Probability, per atomic cross-section, of photoelectric absorption
θ	Inclination angle relative to the horizontal of the γ-ray attenuation experiment
θ	Projection coordinate position
u	Path length through object
$W(\omega)$	Fourier integral window function
x	Photon path length through a material
x	Object coordinate position
x_{offset}	Position error between photon beam and thermocouples
x_{other}	Traversed path length through non-tin materials in the test-object
x_{sf}	Solidification front position in test-object relative to thermocouple number one
x_{tin}	Solid tin thickness used for system calibration
$x_{T_{high}}$	Length of first thermocouple in liquid tin
$x_{T_{low}}$	Length of first thermocouple in solid tin
y	Object coordinate position
Y	Distance from the source to the object
$Y_{crossover}$	Half-power crossover point from the source
Z	Atomic number

Contents

List of Figures

List of Tables

Chapter 1

Introduction

In the aluminum and steel industries, commercial-sized metal strands are cast by the direct-chill or the continuous casting process. In both of these processes, there is always an interface between the liquid and solid phases of the metal known as the solidification front. The heat flow rate into the mold, secondary cooling system, and extraction rate of the strand all influence the shape and position of the solidification front. In turn, the geometry and stability of the solidification front determine the production rate and quality of strand. Consequently, the ability to track the solidification front in real-time will have a significant economic impact on production.

While the economic necessity of monitoring the solidification front is obvious, presently there is no on-line sensor to perform this function. A sensor of this kind is crucial for real-time control and further process development and optimization.

1.1 Scope of Research

This thesis seeks to test the feasibility of and to address the issues associated with monitoring the solidification front in metal casting by transmission of gamma radiation. In particular, the application of computed tomography (CT) for identification of density variations, as encountered in the medical field, is examined. To analyze this problem, two main experiments were conducted. The first experiment tested the principle of gamma radiation attenuation through material of different densities. The second experiment involved the development, testing, and application of a two-dimensional CT system to a metal as it solidifies. The thesis had three goals:

- to construct a gamma radiation-based transmission CT system,
- to identify, analyze, and characterize the critical parameters of the CT system for successful performance, and
- to test the feasibility of using CT to identify the liquid/solid interface in metal solidification process.

1.2 Outline

This chapter provides an introduction to the project, its goals, and motivation. Chapter 2 discusses the bulk manufacture of metal by means of the continuous casting process. In addition, a description of the solidification process is presented, along with current methods to monitor casting quality. Finally, a proposed concept for tracking the solidification front in real-time is described. Chapter 3 offers background on the fundamentals of radiation, its behavior, generation, and detection. In addition, an overview of the principles of CT, equipment, scanning techniques, algorithms, and performance criteria is given. The γ-ray attenuation experiment, conducted to confirm the gamma ray attenuation interaction with matter, is described in Chapter 4. The various performance experiments conducted using the laboratory CT system are detailed in Chapter 5. Chapter 6 reviews the results of the experiments, analyzes the feasibility of the process, and offers recommendations for future development. The appendices provide a description of the interaction mechanisms for gamma radiation, a discussion of various algorithms for CT reconstruction, engineering drawings of various experimental apparatus components, supplemental experiment data, and the source code for the CT data collection program.

Chapter 2

Solidification Process Monitoring

The casting of liquid metal into molds to attain a finished product after solidification is one of the oldest and most useful manufacturing processes. It offers a tremendous amount of versatility in terms of the size and shape of the final object, allowing complex shapes, internal geometries, or very large products. There are several categories and subdivisions of casting process; the main divisions being discrete casting and continuous casting. Discrete casting involves the manufacture of single or multiple near-net-shape parts from either a permanent or expendable mold. Continuous casting differs greatly from discrete casting. It resembles extrusion or rolling processes in that the output of the operation is not a near-net-shape part, but a continuous strand of metal of a given cross-section. The primary purpose of continuous casting is the bulk production of metal, such as steel or aluminum, in finite geometries such as billets or slabs, for use in secondary manufacturing operations. In all casting operations, continuous or discrete, the primary physical phenomenon occurring is solidification. The solidification of the molten metal involves complex fluid flow and heat and mass transfer phenomena, which ultimately influence the finished state of the solid product.

This chapter focuses on a single category of metal casting: the continuous casting of steel. A brief explanation of this process is presented, along with the its benefits over earlier production techniques. Next, the solidification phenomena which occur during continuous casting are analyzed. An overview of the current work in the field of continuous casting and solidification research is presented, and a method of monitoring the solidification front within continuous castings is described.

2.1 Continuous Casting

The process of continuous casting has become one of the most significant technological breakthroughs in the steel industry over the past half-century. By incorporating the various separate steps of ingot casting into a single operation, the continuous casting process allows significant savings in energy and capital while increasing product yield and quality. Although first patented by Bessemer in 1856, the continuous casting process did not achieve significant commercialization within the metal producing industry until equipment problems were overcome in the early 1940s. Since that period, the process has received enormous attention and undergone extraordinary growth. In 1970, the amount of steel continuously cast in the world in relation to the amount of liquid steel produced was 5%. By 1984, it had grown to 47%. By 1991, the continuous casting ratio was 83% for the Western world and 90% for the European Community [34]. In the United States in 1994, there were 129 continuous casters in operation in 92 plants, producing an annual yield of over 113 million short tons of steel [9].

2.1.1 Process Description

Prior to widespread acceptance of the continuous casting process, ingot casting was the main technique used to manufacture steel slabs (rectangular cross-section, 51 mm to 229 mm thick, 610 mm to 1524 mm wide), blooms (square cross-section, 152 mm to 305 mm) and billets (square cross-section, 51 mm to 127 mm). In ingot casting, molten steel is prepared in a furnace and transferred by ladle to a rectangular mold. The molten steel cools within the mold. After solidification is complete, the mold is stripped away and the steel ingot is heated in a soaking pit. Once a proper uniform temperature is achieved within the steel ingot, it is removed from the soaking pit and rolled into the final desired shape. The time required to produce a semi-finished shape by the ingot casting process is seven or more hours [50].

Continuous casting consolidates all the separate steps of ingot casting into a single process. The principle behind this technology relies on the extraction of an indefinite-length strand of steel from the bottom of a vertically supported tundish through a water-cooled copper mold (Figure 2-1 and Figure 2-2). The tundish is continuously replenished with molten steel via a turret-ladle system which receives the steel from a furnace. Heat transfer

from the molten steel through the water-cooled copper mold initiates solidification as a solid skin is formed around a liquid core. Typically, the copper mold is lubricated and oscillates sinusoidally to prevent the solidifying steel from sticking. When the solid skin, supported by rollers, is thick enough to contain the liquid core, the strand is slowly extracted from the mold and further cooled by water jets. As a steady state is reached, the solidifying strand is continuously withdrawn by rollers at a constant speed. The strand is typically withdrawn in the vertical direction initially. As the strand enters the secondary cooling zone, it gradually curves towards the horizontal and straightens. Once solidification is complete, a torch unit cuts the strand transversely and the finished product is taken away for any further operation. The final product shape is controlled by the copper mold geometry, the rolling process during withdrawal, and any post-cut-off processing. For increased production capacities, several strands of steel are typically cast in parallel from the same tundish with "on-the-fly" ladle replenishment.

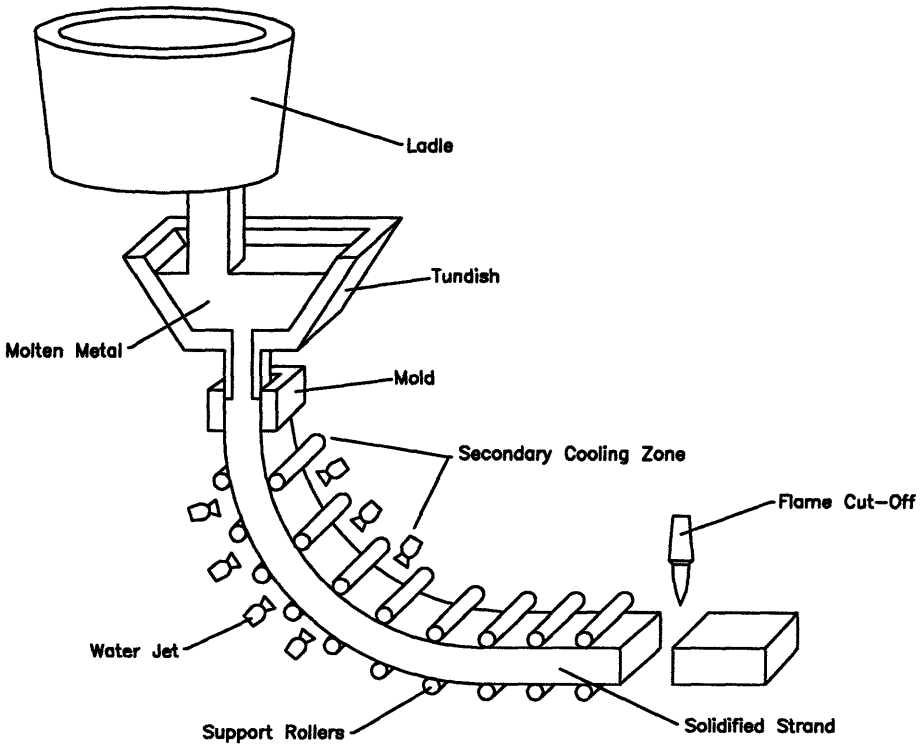

Figure 2-1: Schematic of a Continuous Casting Machine

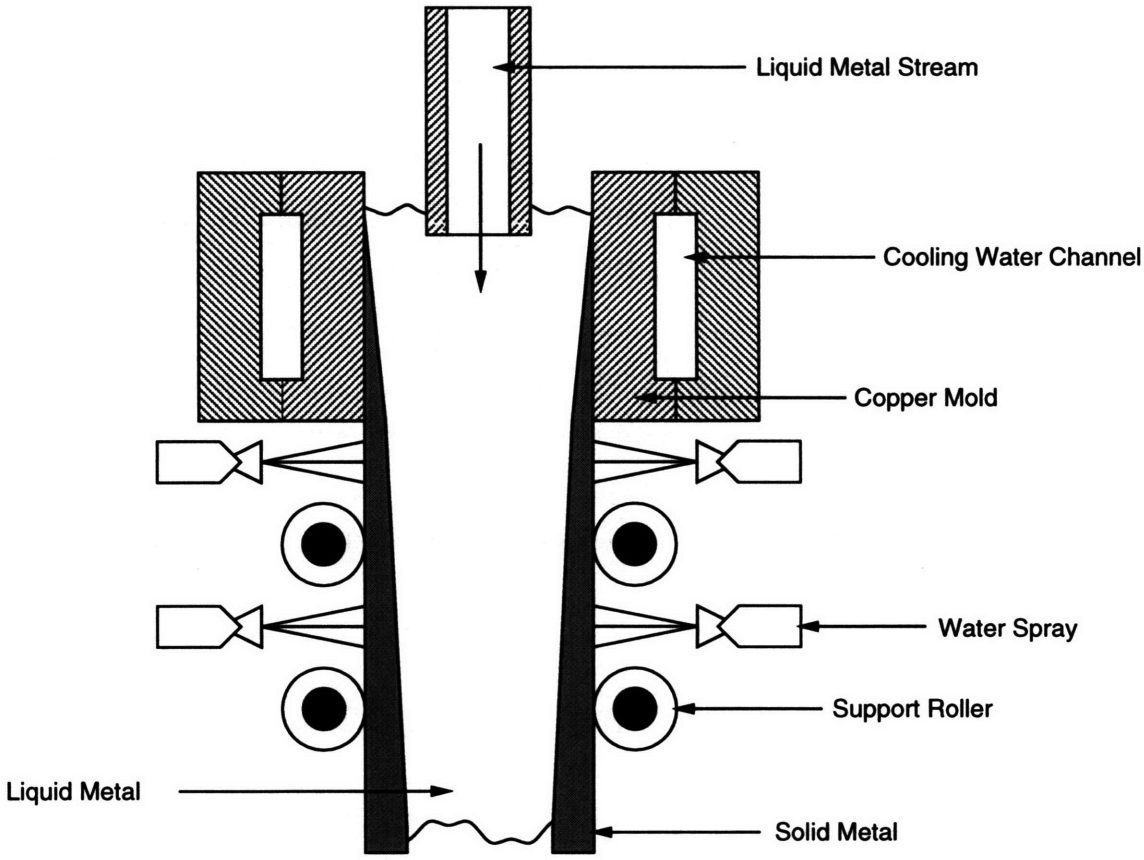

Figure 2-2: Diagram of the Continuous Casting Process

2.1.2 Industrial Significance

As mentioned previously, continuous casting technology has had a major impact on the production of steel over the last half-century. Its chief advantages [34] [50] over ingot casting include:

- **Improved Yield.** Through the reduction of scrap generation, the continuous casting process improves production yield over that of ingot casting. End losses and oxidation losses common in ingot casting are reduced or virtually eliminated. Efficiency is improved through overall better process control. Yield improvements have been consistently reported between 10% to 12%, and as high as 15% to 20%.

- **Reduced Energy Consumption.** By eliminating the intensive steps of ingot casting, such as the soaking pits and primary rolling mills, the continuous casting process generates an net energy savings through reduction of consumption of fuel and electricity. In addition, energy savings is generated directly by the increased production

yield. This energy savings is approximately one million BTUs per ton of cast steel [50], or about 25% that of the ingot casting process [34].

- **Improved Labor Productivity.** By eliminating steps in the ingot casting process which require direct labor input, labor productivity is directly increased. The U.S. Department of Labor reports that 10% to 15% less labor is required for continuous casting than ingot casting. In addition, continuous casting also benefits from the reduction of production time from seven to one or two hours and improved working conditions.

- **Improved Product Quality and Consistency.** Steady improvements in overall product quality and consistency have been made through use of continuous casting. Reduction in the number of production stages results in a more robust process.

- **Reduced Pollution.** In the continuous casting process, hot steel is exposed to the atmosphere for less time than in ingot casting, reducing the amount of airborne particles generated. In addition, the increased yield reduces the amount of primary steelmaking required, reducing the amount of coke manufactured.

- **Reduced Capital Costs.** Capital costs are reduced because of the elimination of molds, stripping equipment, soaking pits, reheating furnaces, and primary rollers.

2.1.3 Future Challenges

Due to its many significant benefits over ingot casting, continuous casting has quickly become the standard manufacturing process of the steelmaking industry, as indicated by production trends over the last two decades. However, the continuous casting process still faces two main challenges [3]:

- The permanent demand from customers for higher quality steels, and

- The need for an increase in productivity to reduce production costs.

In the continuous casting process, as in all casting processes, the quality of the finished product as well as its production rate depends on the solidification rate.

From a quality perspective, it is well documented that solidification mechanics (heat and mass transfer, fluid flow, microstructure formation) influence the final properties of the product [15] [23] [24]. In metal casting, product shortcomings such as surface defects, cracks, inclusions, and macrosegregation are all controlled by the solidification process. By understanding the role solidification plays in the casting process, product quality may be dramatically increased through reduction of undesirable product characteristics.

From a production standpoint, the rate at which a solidifying strand can be extracted from a continuous caster is largely limited by the thickness of the solid shell and, consequently, the solidification process within the strand. If the extraction velocity is too high, the thin, partially solidified shell will rupture, resulting in a "breakout" accident, whereby molten metal spills from the strand and the tundish into the equipment and workplace. Breakout accidents are particularly costly since they require production shutdown during the cleanup period. If the extraction velocity is too low, the continuous caster operates at a low productivity, thus increasing production costs. If accurate control of the solidification process within the strand could be maintained, the continuous caster would run at optimum production rates while avoiding the possibility of breakouts.

2.2 Casting Deficiencies

Deficiencies in metal castings manifest themselves in several forms. In continuous casting, there are two principal types of surface defects, slivers and microcracks, and three principle types of internal defects, axial macrosegregation, V-shaped segregates, and segregated cracks [3]. The surface defects are typically located in the vicinity of oscillation marks. These oscillation marks result from strand solidification within the copper mold. Slivers appear like open oxidized tears of the surface, and their formation has been attributed to the entrapment of inclusions during early solidification in the mold. Microcracks are a very fine network of small tears on the casting's surface, resulting from segregation. The internal defects in continuous casting are chemical heterogeneities, and they are sometimes associated with residual porosity. Porosity is caused by shrinkage of the molten metal as it solidifies or by the entrapment of gases in the casting. Macrosegregation is the separation and disproportionate redistribution of species or solute in a casting as it solidifies, usually involving the movement of the liquidus and solidus within the mushy zone. In the case of continuous casting, disproportionate species transfer to the central core region during longitudinal solidification creates axial segregation. For equiaxed solidification, V-shaped segregates occur along the product axis. Tensile strains imposed on the solidification front by the caster machinery result in internal cracks. These cracks have a random distribution and variable length, from 1 mm to half the strand thickness.

Currently, industrial operations employ three different methods to control the solidifica-

tion structure in the central portion of continuous castings. The first method is to cast the steel with a low superheat. This aids in obtaining a large equiaxed zone around the strand axis while minimizing axial segregation. The second method involves electromagnetic stirring of the liquid steel in the mold or the secondary cooling region. This technique also reduces axial macrosegregation through creation of a large equiaxed solidification zone. The last technique involves maintaining the surface of the cast strand below 800°C to promote high rates of cooling. A rapid solidification rate is developed in the strand, producing a fine columnar microstructure while limiting macrosegregations and V-shaped segregates.

2.3 Current Research In the Field

The drive to produce higher quality castings and to simultaneously increased production rates has fueled various areas of research and innovation. As discussed previously, knowledge of the solidification front in metal casting processes is of great importance to the casting industry. The locations of the solidus/liquidus temperature gradients and local cooling rates at appropriate time intervals provide information which correlates to void formation, cracks, microsegregation, macrosegragation, porosity, and microstructure development. Significant research has been carried out, experimentally, computationally, and microstructurally, to obtain information about solidification phenomena.

2.3.1 Experimental Research

The variety of techniques to experimentally measure or detect the solidification front is quite diverse. These methods are both direct, where the solidification front is tracked in a pseudo-on-line manner, and indirect, where the solidification front is measured after the process is completed. Bakken et al. describe a technique where temperatures are measured using a tree of thermocouples placed within a solidifying aluminum strand [1]. Although the results of this experiment are useful for calculating heat transfer in the shell, the intrusive nature of the method is not applicable in a production environment. Nichols et al. describe an alternate technique of using thermocouples to track the solidification front [48]. A breakout detection system was developed and implemented on a continuous steel caster by incorporating thermocouples into the mold. A control system measured temperature rises in the mold, indicating strand sticking and solidified shell thickness loss. This system was quite

successful in reducing breakout accidents, but the data generated by the process offer little information on the mechanics of the solidification process. Ozgu et al. implemented a similar mold wall thermocouple system for the purpose of measuring mold wall deflection and gap formation [52]. Their work led to improvements in mathematical modeling techniques.

Both Story et al. and Schade et al. document the use of a liquid core detection system by using segment load measurements [54] [62]. This technique involves using strain gauges to measure the ferrostatic pressure inside the solidifying strand at a set location. This pressure is associated with the amount of liquid core present. By tracking the load response during transition from the liquid to solid phase, the location of the final solidification point could be monitored on-line. The segment load measurements provided useful information for increasing the productivity of the continuous casting machine, but little extension of the application is possible. The process is rather inflexible to changes in both strand geometry and casting process. In addition, the technique does not provide any information regarding solidification front geometry or structure.

The *in situ* observation of the solidification of steel using x-ray topography is given by Matsumiya et al. [43]. In their experiments, radiographic images of grain growth in thin slices of steel were taken as the steel was reannealed in a controlled heating/cooling unit. Highly magnified images of grain growth were achieved using this technique. However, its applications at a larger scale are limited. In an intriguing experiment, Deryabina et al. measured the solidification phase thickness in a continuously cast steel ingot using the transmission of gamma radiation [18]. A beam of radiation was directed through a section of solidifying strand. The thicknesses of the liquid and solid sections were calculated based on the attenuation properties of gamma radiation through steel. Although performed in only a single direction, this experiment lays the groundwork for applying CT to the detection of the solidification front.

The examples described here are only a few of the experimental techniques which have been applied to measure the solidification process in metals. Other techniques include liquid metal doping, solid metal doping, and crude liquid pool-depth measurements. Although they provide more information than was known previously, most of these experimental techniques have some shortcoming. They offer only limited information, interfere with the solidification process, do not have on-line measurement capability, or do not scale up from a laboratory system to a production environment.

2.3.2 Computational Models

Computational models offer an economical solution to analyzing the liquid/solid phase change phenomenon in metal solidification processes. The complex geometries and boundary conditions exclude the practical use of analytical techniques. Over the past decade, many numerical simulation and mathematical modeling techniques of solidification processes have been developed [11] [17] [40] [42]. The results of simulations are validated by comparing them to experimental data or other simulation programs. For example, Dalhuijsen et al. document a finite-element formulation of phase change with appropriate latent-heat effects and time stepping and compare a variety of solution methods [17]. Certain solution methods performed quite favorably. However, as model complexity increased, the time for solution convergence increases dramatically and temperature and freezing point positions becomes less accurate. Another finite-element technique was proposed by Chidiac et al. The model predictions were compared to experimental data collected during the casting of zinc, aluminum, and steel [11]. The experimental data were collected using several different techniques, including the measurement of thermocouple temperatures, the analysis of tracer elements by sectioning and etching, and the use of a dip-stick technique to determine pool depth. The authors achieved good results when comparing their finite-element model with the experimental data. Some inaccuracies were present at the mold bottom, which were attributed to the loss of accuracy of the surface heat flux formula, the use of constant value material properties, and a large element size. In addition, the authors express the need for judicious selection of time step and element sizes in the finite-element model due to the transient nature of the problem.

Although numerical simulations offer a significant breakthrough in understanding the evolution of the solidification process, they have many shortcomings. First, the points in time and space at which data are available for computational models and for experimental techniques are not generally the same. As a consequence, comparison is done by interpolation, introducing a source of uncertainty. Second, there is a lack of thermophysical data for many commercial alloys with respect to heat, mass, and fluid flow, resulting in inaccurate data for simulation models. Third, as more detailed and complex geometries and boundary conditions are introduced, solution convergence time can increase dramatically. This is not to say that computational solidification models are not beneficial. Every comparison

of experimental result to simulation has led to either code improvements or the development of better sensors or measurement techniques [25]. However, simulations must still be validated.

2.3.3 Mushy Zone Research

At a microstructural level, much research has focused on the mechanics of the mushy zone, the region where the solid and liquid phases coexist when alloys solidify. Heat transfer, mass transfer, and fluid flow in the mushy zone contribute to casting defects such as segregation, porosity, and hot tears [24]. Mushy zone researchers include Diao and Tsai, who developed a mathematical model to predict the formulation of macrosegregation for unidirectional solidification of aluminum copper alloys [19]. Two mechanisms which occur in the mushy zone contribute to macrosegregation. These are the floating or settling of precipitated phases during solidification, and the flow of either solute-rich or solute-poor liquid into the mushy zone. The authors' study incorporated species equations to investigate solute redistribution in the mushy zone. They report that their model can accurately predict the formation of inverse segregation. Another research project, conducted by Glicksman et al., involves the description of the microscopic evolution of the lengthscales within the mushy zone and the influence of macroscopic transport processes [26]. Theoretical outcomes of this work were the development of temporal scaling laws for the lengthscales and determination of coarsening dependencies on material parameters and solid volume fraction. The theory was verified using thermal decay experiments on pure mushy zone materials. These examples are indicative of the type of research being performed with regard to the mushy zone. The motivation is to better understand the relationships between macroscopic heat, mass, and momentum transport during solidification and the dynamics of microstructural development in the mushy zone.

2.4 Proposed Solidification Process Monitor

As an alternative to current numerical simulations and invasive experimental methods, a real-time non-destructive sensor to monitor the solidification front is being developed at the Massachusetts Institute of Technology [13] [14]. Its application is well suited for the continuous casting process; it offers the possibility of closed-loop process control. The

method is based on the attenuation of γ-rays of sufficient energy through the solidifying strand as well as any surrounding equipment. A schematic of this sensor as applied to continuous casting is shown in Figure 2-3. Radiation from a source is collimated to produce a narrow beam. The beam exits the aperture of the collimator and traverses the path S-1-2-3-4-D from the source (S) to the detector array (D). Along this path, the γ-ray beam travels through the air, the solidified metal shell (1-2), the liquid metal core (2-3), the solidified metal shell again (3-4), and finally through the air to the detector. As it travels, the γ-ray beam interacts with the matter it encounters and is attenuated by the solid and liquid metal. Thus, the incident beam intensity at point 1 will be greater than the transmitted beam intensity at point D. Since the mass attenuation coefficients of liquid and solid metals are the same, while their densities are different [22], it is possible to calculate the thickness of the liquid and solid phases of the metal which the γ-ray beam encounters. By translating and rotating the source and detector about the cast strand (Figure 2-4), a complete profile of the density distribution within the strand can be mapped. This is accomplished through application of the principles of computed tomography. If the scanning and processing is done rapidly, a real-time, two or three-dimensional image of the solidification front within the strand may be generated. This information can be used within a feedback loop for continuous caster process control, all with the benefit of non-interference to the solidifying strand. The advantages of such a sensor include:

- complementing and verifying current modeling techniques,
- providing insight into the fundemental process of solidification,
- providing a process and product design tool,
- reducing the occurance of breakout accidents,
- improving the metal casting quality and production rate.

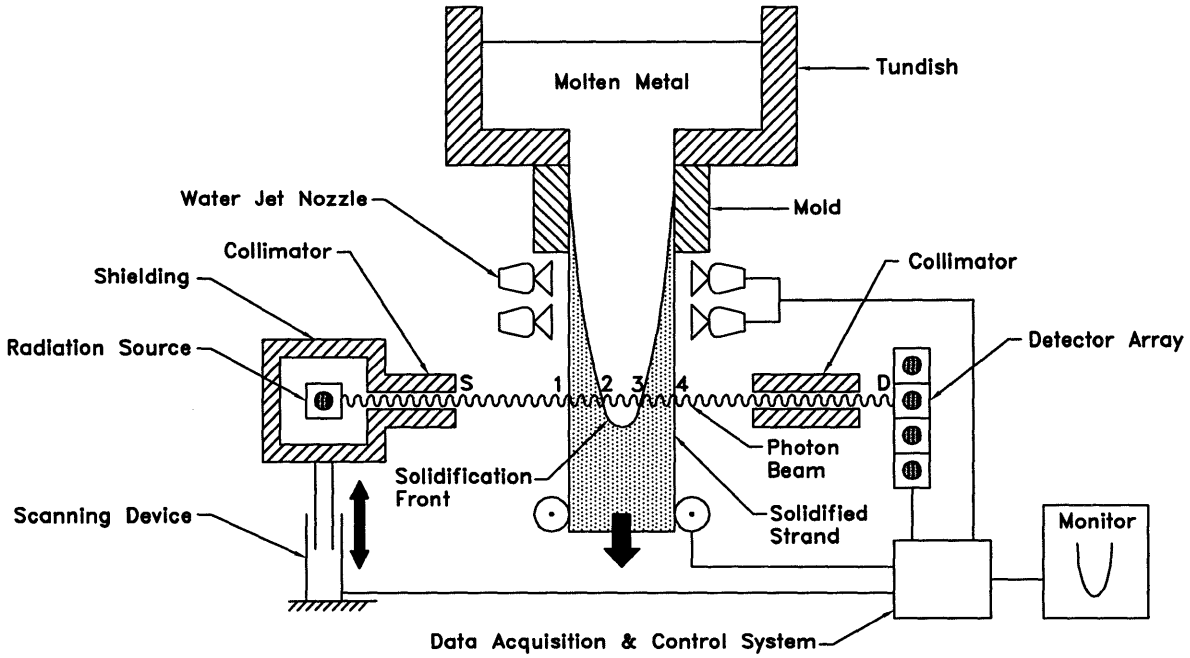

Figure 2-3: Schematic of Solidification Front Detection System for Continuous Casting

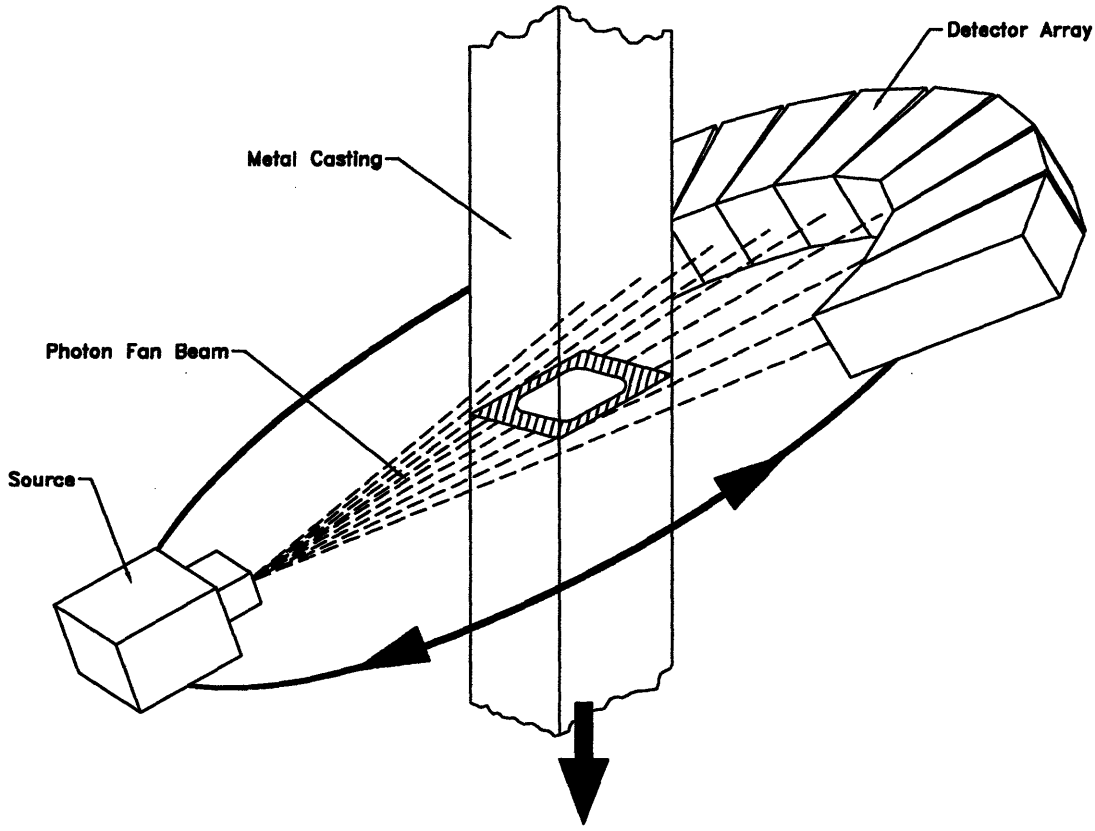

Figure 2-4: Perspective of Tomographic Sensor Applied in Continuous Casting

Chapter 3

Background on Gamma Radiation and Computed Tomography

This chapter introduces the characteristics of radiation and reviews the principles and applications of CT. The reader will thus have a general exposure to radiation and CT principles and mechanics. The information provided here will serve as a foundation and reference for the chapters that follow. If more rigorous discussion on radiation or CT is desired, the reader is directed to the appendix and references at the conclusion of this work.

3.1 Background on Radiation

Radiation originates primarily from atomic and nuclear interactions or processes. Its energy range of interest spans from 10 eV to about 20 MeV. The decay rate of a radioactive source is defined as:

$$\frac{dN}{dt} = -\lambda N \tag{3.1}$$

where N is the number of radioactive nuclei in the source and λ is the decay constant of the material. The value of N is typically measured in curie (Ci) or becquerel (Bq). The half-life of a radioisotope is the time in which the number of radioactive nuclei decreases by half. The value of λ is the disintegration rate of the source material, which is not necessarily representative of the emission rate of radiation. In order to determine the radiation emission rate, one must have a knowledge of the decay scheme of the radioisotope in question. The energy of radiation is typically measured in electron volts (eV), defined as the kinetic energy

gained by an electron as it accelerates through a potential difference of 1 volt. The different categories of radiation can be classified by their ability to penetrate material. The three main types are alpha, beta, and gamma radiation.

3.1.1 Alpha Radiation

An alpha particle is the nucleus of a helium atom. Consequently, there is a positive electric charge associated with it. Alpha radiation is monoenergetic and has a strong correlation between particle energy and source half-life. Alpha particles with the highest energies are produced by sources with the shortest half-lives, typically a few days. As a result, the upper limit on alpha particle energy is around 6 MeV.

Alpha radiation interacts with matter via coulomb forces between the positively charged particles and the electron shells of the incident atoms. Due to the significant number of interactions during its travel, the energy of an alpha particle is quickly lost at the expense of velocity. This affinity for rapid energy loss, as well as its relatively large mass, results in poor material penetration ability, usually only on the order of micrometers.

3.1.2 Beta Radiation

Beta particles are otherwise known as electrons. As such, they carry a negative electric charge. Beta particle sources can be readily created with various half-lives through the neutron bombardment of stable materials. Typically, beta particles are produced when an excited atom loses energy and returns to a de-excited state. During this de-excitation, the beta particle emission is often accompanied by release of gamma radiation as well. The energy of the beta particle varies from decay to decay, having a minimum value of zero to a maximum of the decay energy.

Since the mass of beta particles is equivalent to that of the orbital electrons in an atom, during their interactions with matter beta particles may undergo extensive energy losses and path deviations. In addition to these coulomb losses, beta particles also lose energy by radiative processes during acceleration. The penetration ability of beta particles is about a hundred times greater than of alpha particles. General estimates give penetration ranges of 2 mm per MeV for low-density materials and 1 mm per MeV for moderate density materials [38]. Although significantly larger than that of alpha particles, the penetration ability of beta particles is still only on the order of centimeters even for a source with high energies.

As a result, both alpha and beta particles can be absorbed by materials of meager density and thickness.

3.1.3 Gamma Radiation

Gamma radiation is electromagnetic in nature. It has a shorter wavelength and higher frequency than other types of photons, such as radio waves, light, and x-rays. As expressed by the basic equation for all electromagnetic radiation, the energy, E, of gamma radiation is directly proportional to its frequency, ν:

$$E = h\nu \tag{3.2}$$

where h is Planck's constant. Since the energy of γ-rays can vary significantly, there is considerable overlap in its lower bound and the upper bound of x-ray energy. In fact, the true delineation between γ-rays and x-rays is the origin, not the energy, of the particle. In contrast to both alpha and beta radiation, gamma photons do not carry a charge and have excellent penetrating ability through various media. These properties make gamma radiation ideally suitable for use in tomographic imaging.

There are two main physical processes which generate either characteristic γ-rays or bremsstrahlung γ-rays. Characteristic gamma radiation is produced during nuclear transitions. If an atom has reached an excited state and cannot undergo fission or emit particles, it must attain a more stable state by losing energy though electron shell transition. In the process, a gamma photon is released. These gamma photons have an energy characteristic of the difference between the upper and lower states of the electron, independent of the manner by which it was excited. Since these energy states are sharply defined, the energy of the gamma radiation lies in a very narrow band, uniquely associated with the parent material. Bremsstrahlung, or continuous, γ-rays, result when an electron experiences a near-collision with the nucleus of an atom. As the electron decelerates and loses energy, a gamma photon is emitted. The energy of the photon is dependent on the characteristics of the electron/atom interaction. For many interactions of this kind, the energy of the γ-rays forms a continuous band ranging up to a maximum at the energy of the incident electrons.

3.2 Quantitative Relations for Gamma Radiation

As described by Evans, there are twelve different interactions which gamma radiation may have with matter [22]. These are represented by the type of interaction and the result of the interaction, as shown in Table 3.1. Of these interaction combinations, most occur very infrequently in the energy range of interest to this thesis, 0.01 MeV to 10 MeV. Over this band, three interaction processes dominate: photoelectric absorption (1A), pair production (3A) and the Compton Effect (1C). A more detailed discussion of the three principle interaction mechanisms is presented in Appendix A.

Type of Interaction	Effect of Interaction
1. Electron Interaction	A. Complete Absorption
2. Nucleus Interaction	B. Elastic (Coherent) Scattering
3. Electric Field Interaction	C. Inelastic (Incoherent) Scattering
4. Meson Field	

Table 3.1: Interaction Mechanisms between Matter and Gamma Radiation

As opposed to alpha and beta particles, which slow down gradually through continuous atomic interactions, γ-ray photons are absorbed or scattered in a single event. The photons which undergo an interaction are completely removed from a γ-ray's path-of-travel. As a result, γ-ray photons display an exponential attenuation in matter. The probability, P, that a single gamma photon will *not* undergo a particular interaction (Compton scattering, photoelectric effect, or pair-production) while traversing through a path length, x, is:

$$P = e^{-px} \tag{3.3}$$

where p is the probability of the particular interaction per unit length. When all three interaction mechanisms are considered, the probability of interaction per unit length is known as the linear attenuation coefficient, μ_o, defined as:

$$\mu_o = N(\tau + \kappa + Z\sigma) \tag{3.4}$$

where N is the number of atoms per unit volume of the traversed material. As a result, the

amount of photons, I, which pass through a material is:

$$I = I_o \, e^{-\mu_o x} \tag{3.5}$$

where I_o is the number of photons incident to the material. When calculating the γ-ray attenuation, the mass attenuation coefficient, μ, is often used. It is *independent* of the density and physical state of the absorber and varies only as a function of photon energy. The mass attenuation coefficient is defined as:

$$\mu = \frac{\mu_o}{\rho} \tag{3.6}$$

where ρ is the density of the material. The values of the mass attenuation coefficient for several different materials are plotted in Figure 3-1. By substituting Equation 3.6 into Equation 3.5, we find:

$$I = I_o \, e^{-\mu \rho x} \tag{3.7}$$

For an incident γ-ray beam that penetrates several different materials of various thicknesses, the transmitted amount of photons is:

$$I = I_o \left[\prod_{i=1}^{n} e^{-\mu_i \rho_i x_i} \right] \tag{3.8}$$

Equation 3.7 is the γ-ray attenuation equation for a single absorber material. Equation 3.8 is the γ-ray attenuation equation for n different absorber materials.

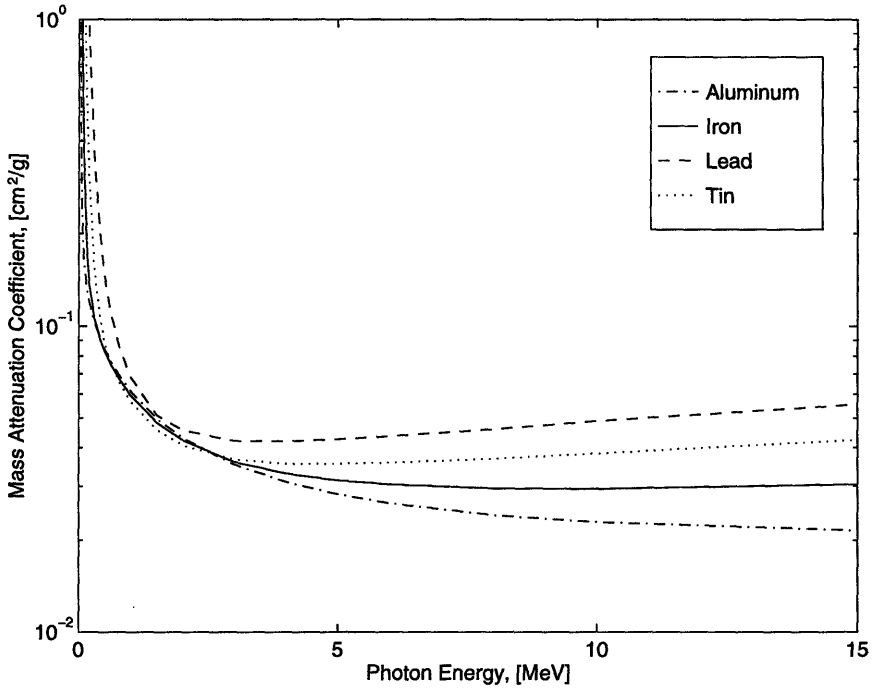

Figure 3-1: Plot of Mass Attenuation Coefficient of Various Elements vs. Photon Energy

3.3 Sources of Gamma Radiation

For the purpose of tomographic imaging, there are several methods for generating gamma radiation. These include electronic sources (x-ray tubes, x-ray microfocus tubes, and linear accelerators (linacs)), radioisotopes, and synchrotrons. On an industrial scale, the thickness and density of the object to be imaged create significant penetration problems. Therefore, several of these sources are eliminated from consideration. Tubes, microfocus tubes, and synchrotrons do not produce gamma radiation at an energy high enough to justify their use. For tomographic imaging on an industrial scale, only linacs or high-energy radioisotopes produce γ-rays of sufficient energy.

3.3.1 Radioisotopes

A radioisotope, as indicated by its name, is the radioactive isotope of a stable chemical element. These isotopes occur naturally as the atoms of normally radioactive elements spontaneously decay into new elements, emitting alpha particles, beta particles, and gamma photons. Radioisotopes may be produced artificially, by such means as bombardment of

a stable isotope with neutrons to create an unstable emitter. By definition, radioisotopes produce characteristic γ-rays. Some common γ-ray radioisotope sources are shown in Table 3.2 [16]. Radioisotopes which emit γ-rays do so as a secondary process after initially undergoing an alpha or beta particle emission, as seen in Figure 3-2 for cobalt-60 (Co^{60}). The primary emission typically has such low energy that it is reabsorbed into the source. Therefore, the only detectable product is the generation of gamma photons.

In general, there is a trade-off between the energy of a radioisotope and its half-life. With the exception of cobalt-60, radioisotopes with long half-lives do not have high energies. This tends to limit the use of radioisotopes in industrial tomographic imaging applications. In addition, their use tends to become cumbersome for large source sizes because of the necessary shielding. Also, the poor flux as compared with electronic sources limits the speed of tomographic imaging. However, radioisotopes do offer the advantage of being relatively inexpensive and monoenergetic. Monoenergetic sources do not beam-harden, a tomographic imaging problem encountered when using electronic sources.

Isotope	Energy [MeV]	Half-Life
Cobalt-60	1.33, 1.17	5.25 years
Cesium-137	0.66	30 years
Iridium-192	0.31, 0.47, 0.60	74 days

Table 3.2: Table of Common Gamma-Ray Radioisotopes

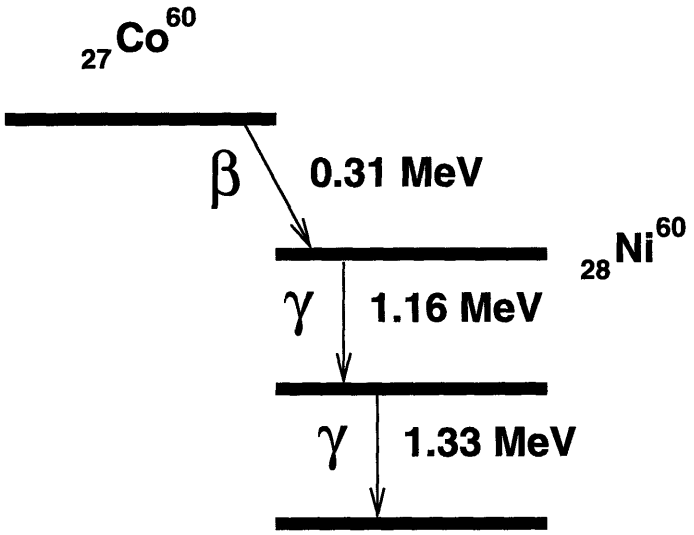

Figure 3-2: Diagram of Radioactive Decay of a Cobalt^{60} Radioisotope

3.3.2 Linear Accelerators

Linacs operate on the same principle as low-energy electronic sources such as x-ray tubes and x-ray microfocus tubes. The linac creates an energetic electron beam which is directed at a target. As the electron beam collides with the target, energy is dissipated through the production of both characteristic and bremsstrahlung γ-rays. The energy spectrum of the gamma photons is highly dependent on the material and geometry of the target. As the output energy of linacs is increased, so too is the efficiency. For a 100 keV beam, less than 1% of the energy of the incident beam is converted to γ-rays, whereas for a 10 MeV beam, the efficiency is about 50% [16]. The energy losses are converted to heat. As a consequence, the flux rate of a linac is limited to the amount of heat which the system can safely dissipate.

The performance characteristics of a linac are its spot size, flux, and energy; these characteristics are dependent. As a result, trade-offs occur between system performance specifications such as spatial resolution, contrast resolution, noise, and penetration depth. When the spot size is decreased, the spatial resolution of the system increases, sacrificing contrast resolution. When the flux is increased, the contrast resolution increases, sacrificing spatial resolution. When selecting the proper spot size, flux, and energy of a linac, the desired performance of the tomographic imaging system must also be addressed.

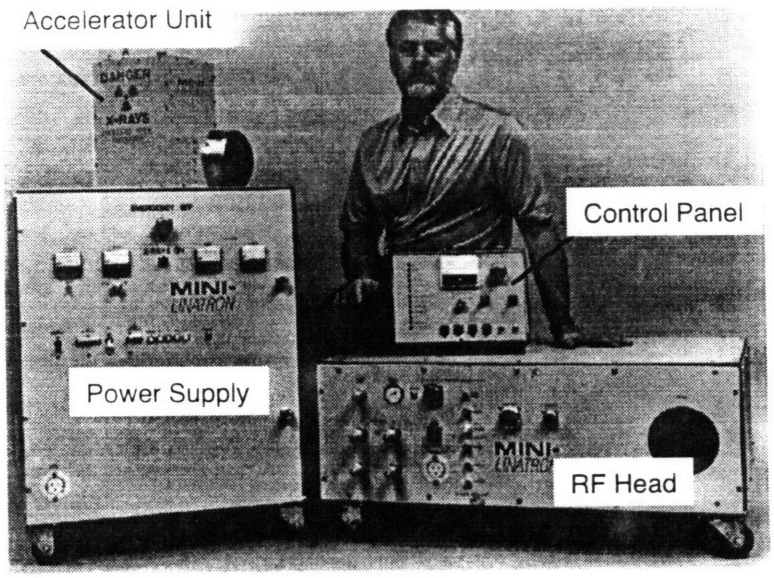

Figure 3-3: Photograph of a Portable Industrial 6 MeV Linear Accelerator

Linacs typically operate in the energy range from 1 MeV to 20 MeV, with fluxes ranging from 100 rad/min @ 1 m to 10,000 rad/min @ 1 m. There are several benefits of using a linac instead of radioisotopes for tomographic imaging. The high energy of a linac gives it the ability to penetrate thick or highly absorbing cross-sections of material. Unlike radioisotopes, an accelerator can be turned on and off, allowing for precise control of dose. In addition, the latest generations of linacs offer a great deal of portability and flexibility [45]. A portable linac system is shown in Figure 3-3 [35]. This particular system has four major components: a 6 MeV accelerator head; a power supply; a control console; and a radio frequency head component.

3.4 Detection of Gamma Radiation

The detection of gamma radiation is simplified when cast in terms of the detection of a single gamma photon. This photon creates a charge, Q, within the detector at a time $t = 0$. The charge is collected in the detector over a time t_c. The detector response to this event is the generation of a current, which is the time derivative of the charge. Restating this relation:

$$\int_0^{t_c} i(t)\, dt = Q \tag{3.9}$$

For single photon interactions the current will appear as a pulse, varying in width and height for different collection times and charges.

3.4.1 Detection Methods

There are three general operating modes for radiation detectors: pulse mode; current mode; and mean-square voltage mode. The pulse mode operation is the simplest and most common. Each individual γ-ray photon which interacts with the detector is registered by measuring the charge associated with the event. This method is only practical when the number of photon interactions is low. At large fluxes, the time between events may be very short or events may overlap, complicating the count measurement. In this case, it becomes necessary to take a time average over many events. Current mode and mean-square voltage mode are both suitable for this task. Current mode is the more common approach, averaging out event interval fluctuations by recording an average current over a given period. The long time interval reduces the statistical fluctuations in the signal, but slows the response to rapid changes in the rate of interactions. The mean-square voltage mode is a specialized operation most often used in mixed radiation environments. This detection mode produces a mean square signal which is proportional to the square of the charge per event. This allows for differentiation between dissimilar radiation types based on their different charge production.

3.4.2 Detector Types

The detection of gamma radiation for the purpose of CT is performed using two main types of detectors, gas-ionizing and scintillation. The gas-ionizing detector consists of a chamber containing a particular ionizable gas. Also inside the chamber are two electrodes maintained at a high voltage. The gas acts as an insulator between the two electrodes and no current is allowed to pass between them. When γ-rays impinge on the detector chamber, energy is transferred to the gas, causing ionization to occur. The ions are attracted to the charged electrodes, causing a current to be produced proportional to the intensity of the event.

A scintillation detector works according to a similar principle. The detector consists of a scintillation crystal and a photomultipier tube or photodiode. As the γ-rays impinge on the detector, energy is transferred to the scintillation crystal and ionization occurs. As the ions and electrons recombine in the crystal, photons with a visible spectrum wavelength

are released. The light produced by these photons is measured by the photodetector, which generates a current proportional to the intensity of the event.

3.5 Background on Computed Tomography

CT provides the ability to visualize a two-dimensional cross-section through the interior of an object at a chosen view-plane, or slice. By combining multiple two-dimensional slices, a three-dimensional image of the object can be reconstructed. CT was originally developed for use in the field of medicine in the 1970s, where it revolutionized the process of diagnostic imaging by its ability to provide detailed information in a non-invasive manner. This ability to investigate the interior of a material non-destructively has led to increasing applications of CT within industry.

The basic principles of CT are best understood when compared to the technique of radiography, such as the common medical x-ray. A simple example of the differences in imaging ability between radiography and CT are shown in Figure 3-4. In radiography, radiation is directed perpendicular to a test object at a single view angle. The reproduced image represents the total radiation attenuation through the thickness of the object. As a result, the difference between object density and object thickness through a particular path from source to image cannot be resolved. In contrast, in CT , radiation is directed through a test object at in a single plane *at multiple view angles*, as depicted in Figure 3-5. The attenuation of the radiation at multiple positions is recorded. Using the attenuation data from these multiple view angles, the local attenuation value for a small volume element within the object is calculated. As discussed previously, the local attenuation value is a material-dependent property, independent of object geometry. Consequently, the distribution of local attenuation values reconstructs to an image of the interior of the object. The image is representative of a thin slice parallel to the incident radiation beam.

The development of CT as a viable method of non-destructive evaluation was driven by several factors: the discovery of crystal scintillation in the presence of x-rays, the development of electronics, the work of Radon, and the dawn of the computer age. The first x-ray radiographs were produced by Roentgen in 1895; the principles of the technique remained unaltered for the next seventy years. In 1917, the mathematical analysis which forms the basis of CT was performed by Radon. He showed that is is possible to determine the value

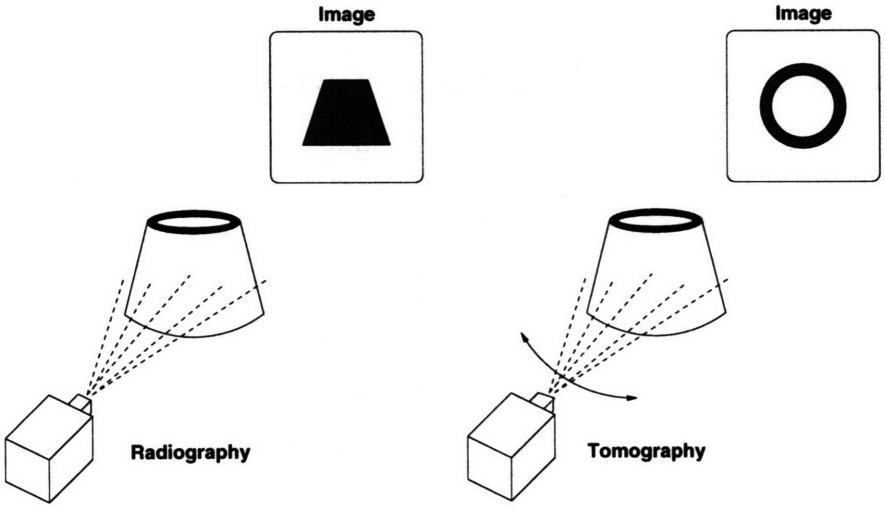

Figure 3-4: Comparison between Radiography and Tomography

of a function over a region of space if the set of line integrals is known for all ray paths through the region [16]. However, the complexity and intensity of the calculations needed to carry out the analysis was unachievable until the advent of computers forty years later. In the late 1960s, higher quality radiographs and the ability to differentiate between superimposed features were necessitated by the medical field. Spurred by this demand, the first work on what later became known as CT was performed by Hounsfield.

Hounsfield, working for EMI Limited in England, broke the perceived wisdom that a radiograph must be produced on film. Originally focusing on pattern recognition studies and information interpretation systems, Hounsfield worked with γ-ray absorption experiments. This led to his "discovery" of the technology of CT–the computer analysis of radiation attenuation data to create a three-dimensional image of a black-box object. Settling on the medical field as the primary beneficiary of this technique, Hounsfield built an experimental system using an Americium radioisotope source and sodium crystal detectors in 1968. The first experiments took nine days to complete data acquisition and two and a half hours to complete image reconstruction. Image quality was poor, but the fundamental principles of the technique were proven. After the initial investigations, significant interest was generated within the medical community and Hounsfield received support from the British Department

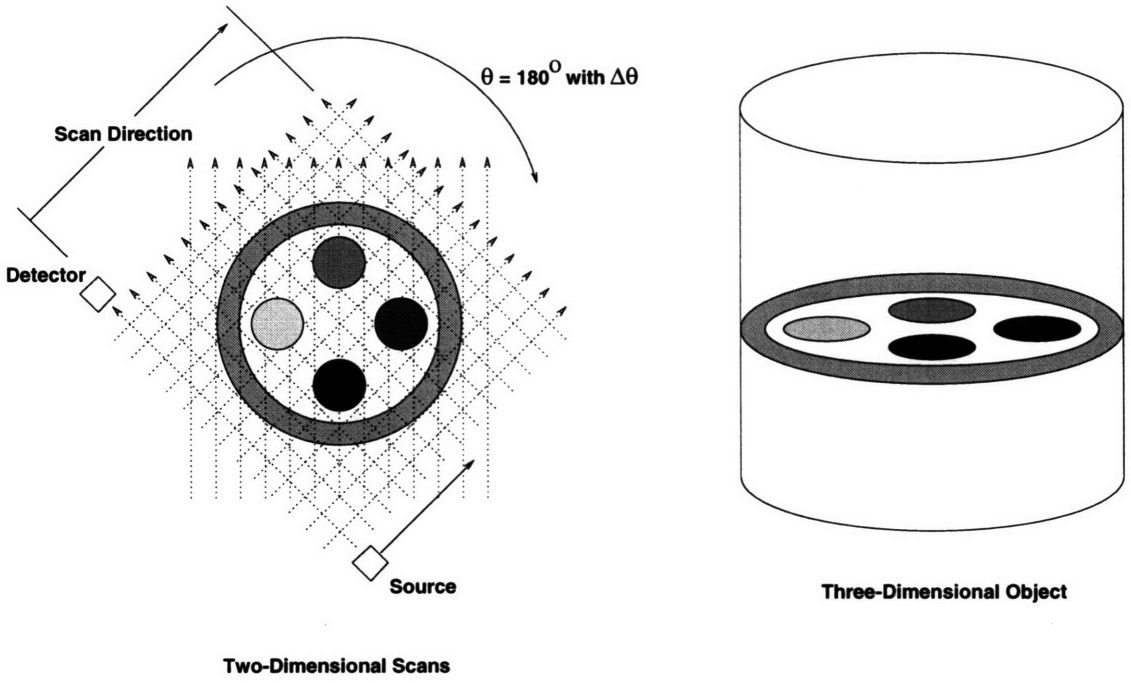

Figure 3-5: Schematic of Tomographic Imaging Technique

of Health. A prototype machine was developed by 1971, and medical testing was carried out by Hounsfield and Ambrose, a neuroradiologist. The scanning time of the machine had been reduced to four minutes. Experiments were conducted on seventy patients and the findings were reported at the Annual Congress of the British Institute of Radiology in London in 1972. CT was immediately recognized as a revolutionary discovery in the area of medical diagnostic imaging, and its application and development gained widespread interest. Hounsfield won the 1979 Nobel prize in medicine for his work.

3.6 Scanning Techniques for Computed Tomography

A typical CT system consists of six components: a radiation source; a radiation detector or detectors; a motion/position system; an operations console; control and processing software; and a test specimen [8]. As CT systems have developed over time, multiple equipment configurations have arisen. Although each has its own advantages, the successive "generations" of scanners have improved upon prior shortcomings, primarily by decreasing the data acquisition time. Examples of four generations of CT scanners are shown in Figure 3-6.

A first-generation scanner is the simplest and least expensive system to implement. It

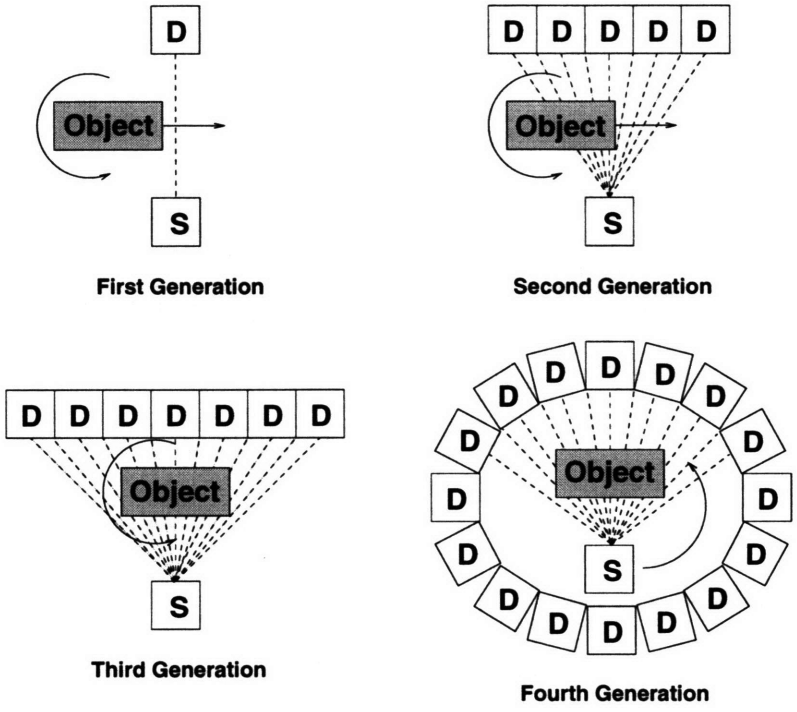

Figure 3-6: Schematic of Several Generations of CT Scanning Methods

incorporates a single pencil-beam source and single detector component. At a given view angle, the object is moved transversely across the path of the source/detector, perpendicular to the photon beam. A parallel beam data set is acquired in a point-by-point manner. After a transverse scan is complete, the object is rotated to another view angle and the process is repeated over a 180^o field of view. A second-generation system is identical to that of its predecessor with the exception of having a fan-beam style source and multiple detectors. The object is still translated and rotated through the path of the photon beam. The fan-beam source and multiple detectors reduce the number of view angles needed. Second-generation systems are quite common in industrial applications because of their flexibility in accommodating different objects, changing source/detector distance, and optimizing spatial resolution. Third-generation systems eliminate the need for object translation by using a wide fan-beam source and multiple, narrowly-spaced detectors. All the data for a view angle are acquired simultaneously, with object rotation the only positioning required. Third-generation systems are used in almost all medical imaging applications, where throughput and speed is critical. Fourth-generation systems improve on the third-generation by incor-

porating a 360^o ring of detectors encompassing the object. The fan-beam source rotates about the object, breaking the fixed geometric relationship between it and the detectors. Although mechanically complex, this system effectively reduces some types of artifacts by averaging out anomaly phenomena over many detectors. However, in a fourth-generation system, the direction of radiation into the detector components changes continuously during measurement, making such a system unsuitable for many industrial applications where a large amount of scatter is present [45].

3.7 Principles of Computed Tomography

In CT , the line integrals of the attenuation measurements over various angles about an object are reconstructed into a single-plane image of the object. A single two-dimensional plane through an object must first be chosen. This image plane has two coordinate systems, as shown in Figure 3-7. The first is the object coordinate system (x, y), defined in the plane of the object. The second is the projection coordinate system (s, θ), which describes the line integrals of the attenuation measurement through the object. The origin of both coordinate systems is specified as the center of rotation of the object.

The reconstruction of a two-dimensional image involves transforming the line integral measurements into the object coordinate system. By generalizing the notation of Equation 3.7, the line integral, $g(s, \theta)$, for a particular transverse position, s, and view angle, θ, takes the form [55]:

$$g(s, \theta) = \ln \frac{I_o(s, \theta)}{I(s, \theta)} = \int_L f(x, y) du \tag{3.10}$$

where L is the path over which the line integral is evaluated, and $f(x, y)$ is the distribution of linear attenuation coefficients within the object. Mapping the distribution of the linear attenuation coefficient from a rectangular coordinate plane in the object to an angular coordinate plane is done via the Radon transformation:

$$g(s, \theta) = \int_{-\infty}^{\infty} f(s \cos\theta - u \sin\theta, s \sin\theta + u \cos\theta) du \tag{3.11}$$

The coordinate system (s, θ) is known as the Radon domain. For a fixed view angle, θ, the value of $g(s, \theta)$ is known as a projection. The reconstruction of images from projections is based on the solution of Equation 3.11. The distribution of the linear attenuation coeffi-

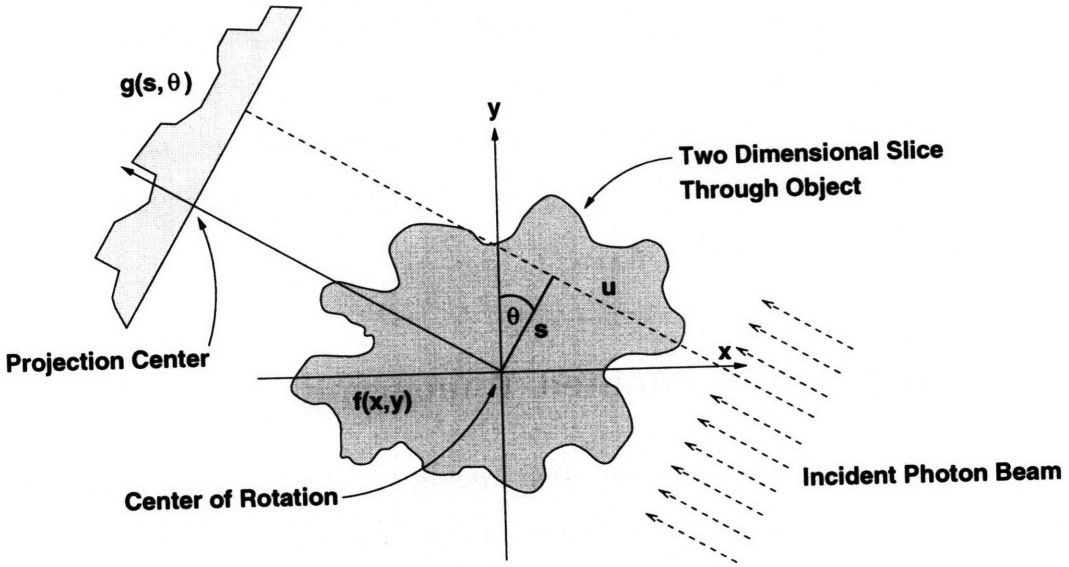

Figure 3-7: Layout of Coordinate Systems of Tomographic Imaging System

cients, $f(x, y)$, within the object is attained by solving the Radon transform for its inverse. Consequently, the density through a two-dimensional plane can be determined.

The inverse of the Radon transform can be obtained by applying one of several mathematical methods, including summation, series expansion, analytical solutions, or Fourier transformations. Budinger and Gullberg [6] describe thirteen different solution methods. These include such techniques as direct matrix inversion, back-projection, simultaneous iterative reconstruction (SIRT), algebraic reconstruction (ART), iterative least-squares, and filtered back-projection (FBP). From method to method, there are trade-offs between accuracy, computation time, view angle requirements, and noise rejection. In the majority of today's commerical CT scanning and reconstruction equipment, the FBP algorithm is the predominant choice due to its efficient hardware implementation, flexibility, robustness to noise, and model application ability. A discussion of the Radon transformation and several solution algorithms is presented in Appendix B.

3.8 Computed Tomography Performance Parameters

By the very nature of a CT system, its primary performance specification is the ability to detect a defect or anomaly within an object of interest, it be a tumor in a human being, a crack in a turbine blade, or a density deviation in a solidification process. The anomaly detection capability is linked directly to the overall quality of the generated CT image, in addition to how well the image accurately represents the properties of the real object. The quality of the CT image is defined by four main parameters: noise; spatial resolution; contrast resolution; and artifacts [8] [16] [58]. Since these parameters are not mutually independent, performance trade-offs must often be made based on individual system needs. In general, those factors that increase spatial resolution also increase noise and decrease contrast resolution.

3.8.1 Noise

Some form of noise is present in all CT imaging systems. Elements such as electronic noise and scatter noise can be minimized through careful planning. However, the quantum nature of electromagnetic radiation dictates that there will be a statistical variation in the number of photons which are detected. This statistical noise follows a Poisson distribution, whereby the variance of the signal is equal to the mean:

$$\sigma = \bar{n} \tag{3.12}$$

For a confidence interval of one standard deviation, if an average number of photons, $\bar{n}$, strike a detector over a given sample time, the number of photons recorded will vary as:

$$n_{count} = \bar{n} \pm \sqrt{n} \tag{3.13}$$

The propagation of this noise to the final image is complicated by the various component geometries and reconstruction algorithms which can be used. To analyze the degree to which noise degrades a particular system parameter such as contrast resolution, one can use the probability-distribution function (PDF). Although the statistical variation of photons behaves as a Poisson distribution, the PDF is usually approximated by a normal distribution

in practice [58]. It is expressed as:

$$PDF(n) = \frac{1}{\sigma\sqrt{2\pi}} \exp\left[\frac{-(n-\bar{n})^2}{2\sigma^2}\right] \tag{3.14}$$

For the measurement of the linear attenuation coefficient at a particular translational and rotational position, the PDF would have a value of one in the ideal case. In reality however, the statistical variations in the photon count propagate to the calculation of the linear attenuation coefficient. The PDF takes the shape of the familiar bell-curve.

Since the deviation of the photon count is equal to the square root of the mean, it is evident that the noise in a single measurement can be reduced by increasing the number of photon counts:

$$SNR = \frac{n}{\sqrt{n}} = \sqrt{n} \tag{3.15}$$

where SNR is the signal-to-noise ratio. Increasing the photon count can be accomplished by either increasing the photon flux through the material or increasing the measurement time for a given position.

3.8.2 Spatial Resolution

The scale on which shapes in a CT image are faithful reproductions of an object is the measure of the spatial resolution of a system. Due to the discrete sampling and the width of the γ-ray beam, features become blurred. This blurring effect alters such characteristics as the shape of a feature, the resolution of multiple features, and the overall contrast of the system. The spatial resolution is primarily determined by the size of the γ-ray focal spot, the collimation of the detector, and the scanner geometry. Accordingly, a specified spatial resolution defines the geometric configuration of the system. In addition, the mechanical accuracy of the positioning system also affects the spatial resolution. An image cannot be reconstructed to an accuracy greater than that of the positioning mechanism.

Spatial resolution is often measured by means of the point-spread function (PSF) of a uniform object with a thickness less than that of the pixel size. The PSF can be determined by scanning a object such as a wire lying perpendicular to the image plane. The width of the PSF function at half its maximum (FWHM) provides an estimate of the image sharpness, and thus spatial resolution. Alternatively, taking the Fourier transform of the PSF provides the modulation transfer function (MTF). The MTF is a measure of the frequency response

of the CT system. That is a ratio of the output to input modulation intensities as a function of spatial modulation frequency. In general, large homogeneous features (low frequencies) are reproduced accurately and small features (high frequencies) are not. For display, the pixel size of an image is usually chosen as slightly less than half of the spatial resolution of the system. This strikes a compromise between image quality and reconstruction time.

3.8.3 Contrast Resolution

The ability of a CT system to faithfully reproduce material variations in an object is the measure of the contrast resolution of a system. In the simplest sense, contrast resolution is a measure of the overall noise of an images, reflected in the graininess of the image. The contrast resolution is a function of the amount of variation between the linear attenuation coefficient of two different materials. The contrast resolution can be defined as:

$$Contrast\% = \frac{|\mu_{object} - \mu_{background}|}{\mu_{background}} \times 100\% \tag{3.16}$$

where $\mu_{background}$ is the linear attenuation coefficient of a background object and μ_{object} is the linear attenuation coefficient of the object of interest. Since the linear attenuation coefficient is energy-dependent, contrast resolution is dependent directly on the energy of the γ-ray source. In addition, it is affected by the measurement time per position, since noise and contrast are correlated. As a result, there is a trade-off between using a low-energy source and a high-energy source. At low energies, the contrast resolution is high since there is a large variation between the linear attenuation coefficients of different materials. The drawbacks are that photon transmission is poor and noise is high. Thus, a longer measurement time is necessary to reduce noise. With a high-energy source, transmission is improved, noise is reduced and measurement time can be shortened. However, the linear attenuation coefficients between different materials do not vary tremendously, and as a result, contrast resolution is poor. As discussed previously, the extent to which noise degrades the contrast resolution of an image can be determined by computing the PDF of the linear attenuation coefficients μ_{object} and $\mu_{background}$.

3.8.4 Artifacts

Artifacts are systematic variations or correlated noise which cause the appearance of features in an image which are not present in the object. Artifacts are present in all CT images to some degree. They can be described by their cause and effect. The performance of a CT system is characterized by the degree to which artifacts are suppressed or reduced in the final image. Processes such as beam-hardening, radiation scatter, equipment misalignments or inappropriate configurations, insufficient data, improper sampling, or incorrect reconstruction algorithm selection cause image artifacts to be produced. Artifacts manifest themselves in the reconstructed image in many forms, including streaks, rings, noise, blurring, and distortion. McFarland [44] classifies reconstruction artifacts into four categories, as shown in Table 3.3.

System and Data Acquisition	Algorithm Artifacts	Photon Spectrum Effects	Object Effects
1. Beam Alignment 2. Detector Alignment 3. Beam Uniformity 4. Detector Uniformity 5. Insufficient Angles 6. Insufficient Sampling	1. Filter Effects 2. Partial Volume Effects	1. Over-Attenuation 2. Beam-Hardening 3. Scatter	1. Motion

Table 3.3: Classification of Reconstruction Artifacts

Although a complete discussion of all artifacts is impractical, some of the more common types include centering errors, singular bad rays, insufficient data, filter effects, beam hardening, scatter, and object motion [44] [55] [56]. When the object projection is incorrectly centered relative to the source/detector array, the artifacts are edge streaks from the perimeter of the image. A single streak through the reconstructed image is indicative of a bad ray measurement. The artifacts resulting from insufficient data vary. They include image distortion, blurring, and streaks, depending on the quantity of missing data. Inappropriate selection of the reconstruction filter generally causes artificial smoothing in the image, degrading spatial resolution, or causing edge streaks in the case of dense objects with straight edges. Beam hardening occurs when polychromatic radiation is used, such as a linac. Since the linear attenuation coefficient is energy-dependent, using a broad energy spectrum has an averaging effect. The inaccuracy results in a cupping effect in the reconstructed image,

whereby the linear attenuation coefficient is highest at the object's perimeter and lowest in the center. Excess scattered radiation results in a higher than normal count for a given projection position, which manifests itself as noise in the case of uniform scatter, or as a cupping effect in the image, if the scatter is non-uniform. Object motion results in a time average of the linear attenuation values, resulting in blurring of the final image. In general, artifacts can be minimized and controlled through careful system design, appropriate image reconstruction, and proper data compensation and adjustment.

3.9 Industrial Applications of Computed Tomography

As discussed in Section 3.5, CT scanning and reconstruction systems were originally developed for diagnostic imaging in the medical field. The ability to provide detailed, useful information about a patient in a non-invasive manner revolutionized the field of medicine. With the hope of producing the same type of impact, CT systems have found their way to industrial applications over the past fifteen years. Current applications of CT systems in industry are primarily for the non-destructive inspection and evaluation of manufactured component parts [4] [21]. However, potential for this technology stretches into the areas of industrial design and manufacture as well.

As described by Ross et al., General Electric Company has applied CT to a wide variety of inspection applications for products such as helicopter rotors, rocket propulsion systems, composite structures, electronic assemblies, castings, welds, ceramics, computer chips, and automobile components. For example, CT systems have been applied to reverse-engineer an aircraft engine turbine blade based on digital replica data. Also, CT systems are currently used to generate two-dimensional finite element models, speeding up structural analysis by a factor of ten. In the way of process control, data collected using CT technology in casting and machining operation allow for abnormality correction and material waste minimization. Process savings of up to 30% of scrapped parts have been reported [53].

The development of a mobile CT inspection system for industrial applications has been reported by Munro et al. [45]. The motivation for this system was to provide service inspection for the detection and prevention of manufactured component damage in field locations. Suggested applications for the system include testing stationary parts of complex systems such as pipes and tubes for wall thickness wear, the examination of corrosion

damage in steel within concrete support structures, the analysis of utility pole degradation by insect damage and rot, and the diagnostic imaging of tree cross-sections for environmental research.

In the manufacture of complex composite materials, conventional non-destructive evaluation techniques such as ultrasonics or radiography do not provide adequate information to detect internal flaws or defects. London et al. [41] document the use of CT for defect inspection in continuous-fiber-reinforced metal-matrix composites (MMC) and glass-coated carbon-carbon composites. Important details such as fiber alignment and spacing, fracture surfaces, and delamination of composite materials can be resolved using CT reconstructions. In addition, CT images have aided in the development of tensile deformation models for MMCs.

Stock et al. recount the use of CT for the analysis of fatigue crack closure in material testing. By studying crack propagation and morphological modifications during various phases of material loading and fatigue, improvements in fracture mechanics and finite element analysis will result. CT systems are uniquely suited to this task by their two- and three-dimensional imaging ability, the lack of which is a shortcoming with other inspection methods [61].

3.10 Computed Tomography Using Limited Data

An area of current interest in CT is the development of image reconstruction techniques based on limited data. Many industrial situations are not suitable for CT data collection over the required number of projections. Physical limitations may prohibit scanning over certain ranges, or time constraints for image generation may require selected data to be sampled. As noted previously, undersampled data lead to artifacts in the reconstructed image. For proper image reconstruction using the FBP reconstruction algorithm, the relationship between the number of view angles, N_θ, and the number of transverse measurements, N_s, is [60]:

$$N_\theta \geq \frac{\pi}{2} N_s \tag{3.17}$$

Alternate algorithms are being developed for use when a complete data set is unavailable. For example, Bhatia [2] documents a wavelet transform-based algorithm suitable for reconstructing limited data CT images. Work is currently being performed using limited data in

conjunction with *a priori* information about the object [16] [55]. Various sources of *a priori* knowledge can be used to create limited data models. These include the incorporation of known noise PDFs, beam profile shapes, detector profile shapes, global data consistency, extent or bandlimits, object boundaries, expected object densities, object symmetries, or stochastic information. Limited data reconstruction techniques use the projection data over whatever range is available together with a theoretical, complete data set based on the object and scanner characteristics. The limited data may be in the form of limited angles, limited views, insufficient sampling, or truncated sampling. A complete reconstruction is performed by correlating and synthesizing the information between the two sets and filling in the missing projection data.

Numerous limited data algorithms have been developed with varying degrees of success, but care must be taken to insure that results are not misinterpreted. The main issues for this process involve noise sensitivity, model-to-process mismatches, and algorithm convergence properties. In addition, many additional resources are necessary to perform limited data analysis and interpretation. Currently the focus of significant development, limited data reconstruction offers an important tool for CT where standard techniques would otherwise fail.

Chapter 4

Gamma-Ray Attenuation Experiments

To verify the attenuation mechanism of gamma radiation through matter, an experimental study was conducted to measure the gamma photon path length [14]. A collimated beam of gamma radiation was passed through a test object and the attenuation of the beam was measured. The test object consisted in part of pure tin in a two-phased state. By varying the heating and cooling of the tin, the γ-ray beam could be directed through different fractions of liquid and solid tin. The liquid path length of the photon through the tin was calculated based on the fundamental attenuation law of gamma radiation. This was compared to the liquid path length calculated from the solidification front position based on thermocouple measurements. The results compare favorably, confirming the attenuation phenomenon of gamma radiation through material of varied density, in particular, a metal existing in a two-phase state.

4.1 Experimental Apparatus

The basic components of the experiment were a radiation source, detector, photon count measurement system, temperature measurement system, and a test-object. A description of the first four components follows, with the test-object described in the next section.

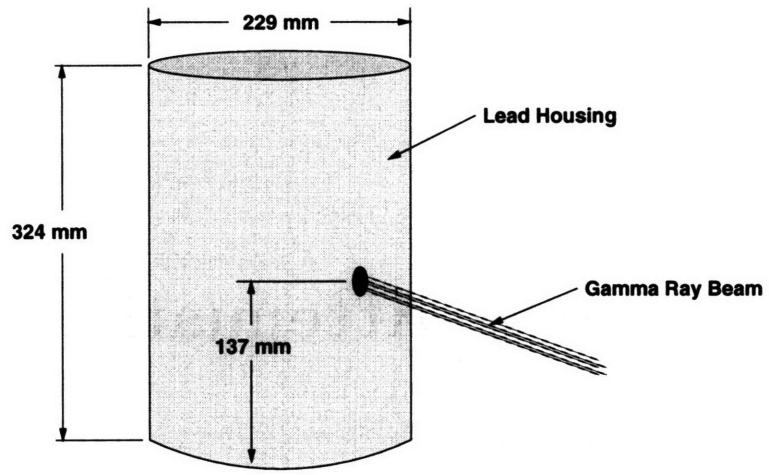

Figure 4-1: Schematic of Radioisotope Source Used for Tomographic Experiments

4.1.1 Radiation Source

A Co^{60} radioisotope was used to generate the gamma radiation. The source size was 7 mCi, producing gamma photons at two distinct energies, 1.16 MeV and 1.33 MeV. The radioisotope was shielded in a cylindrical lead housing with a 229 mm diameter and a 324 mm height. The housing had a 6 mm diameter hole drilled through its side, which served as a pencil-beam style collimator and aperture for the gamma photons. The aperture was located 137 mm from the base of the cylindrical shielding. Figure 4-1 shows a schematic of the source.

4.1.2 Radiation Detector

A single Rexon Technologies model NAI4-4MX4-3 sodium-iodide (NaI) scintillation detector was used to measure the γ-ray intensity. The sodium-iodide crystal was a 100 mm cube. The detector output was passed to a Canberra model 1412 research amplifier and a Canberra model 2037A edge/crossover timing counter. A Bertan Associates model 313A DC power supply operating at 1300 volts powered the detector. The detector was collimated and shielded using several layers of lead, each 51 mm thick. Several collimators were tested with various aperture sizes, including a 14 mm diameter and a 9 mm diameter. The best results were achieved with a collimator with a 2 mm diameter aperture size.

4.1.3 Data Acquisition and Control

There were two main parts of the data acquisition system, the photon count measurement program and the temperature measurement program.

Photon Count Measurement Program

The photon count measurement program was written by DongSik Kim in Microsoft C and executed on a Gateway 2000 Model P5-100 100 MHz Pentium PC compatible computer. Because the photon flux from the Co^{60} source was relatively low, the photon count measurements were performed in pulse mode. The signal output from the Canberra edge-crossover timing counter was connected to a Keithly-Metrabyte DAS-1601 analog-digital input-output board with 12-bit resolution. The intensity of the γ-ray beam was determined by measuring the photon count over a chosen count time and recording it with the control program.

Temperature Measurement Program

To perform temperature measurements, required to locate the position of the solidification front, the data acquisition was performed using Omega chromel-alumel (K-type) thermocouples in conjunction with a Keithly-Metrabyte DAS-TC data temperature measurement board. The software supplied with the DAS-TC board was used to record the thermocouple temperatures. The temperatures were measured over the same time interval as the photon count and recorded using the control program. The thermocouples had a diameter of 1.6 mm and a length of 203 mm. The thermocouple accuracy was 2.2^{o}C and the DAS-TC board accuracy was 0.05^{o}C.

4.2 Experimental Setup

The setup for the γ-ray attenuation experiment is shown in Figure 4-2. The Co^{60} radioisotope was mounted on a steel platform at a 45^{o} angle relative to the horizontal. The NaI scintillation detector was also mounted at a 45^{o} angle, in line with the photon beam emitted from the Co^{60} source. The photon beam incident to the detector was not collimated.

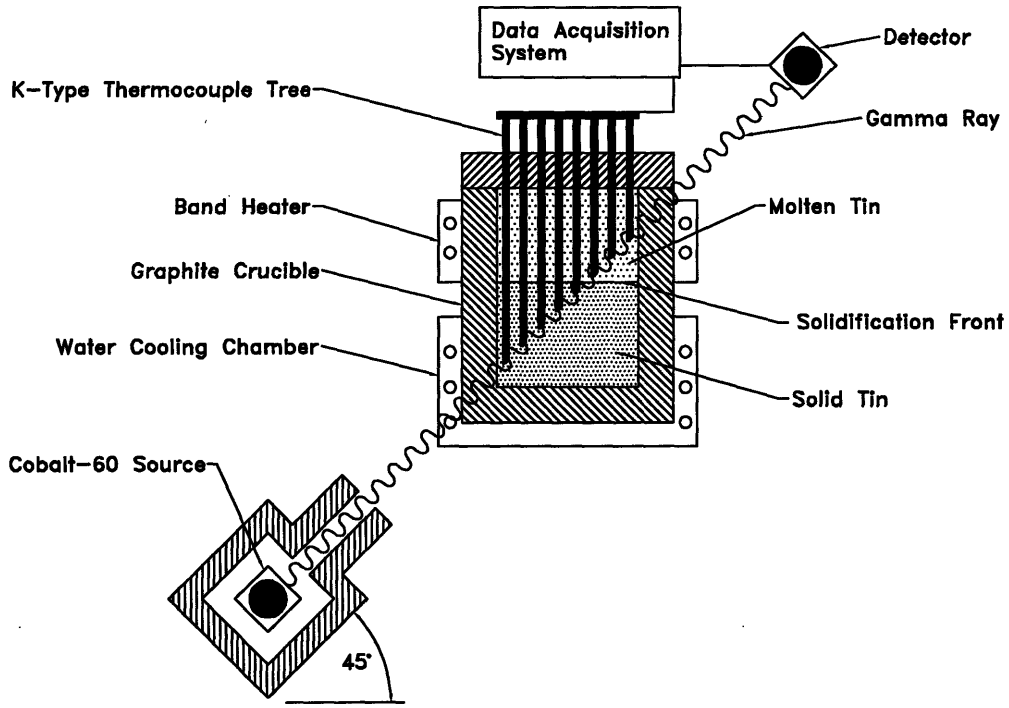

Figure 4-2: Schematic of Solid/Liquid Path Length Experiment

As seen in Figure 4-2, a test-object was mounted between the Co^{60} source and the detector. The test-object consisted of a 51 mm ID by 64 mm OD by 152 mm long cylindrical graphite crucible. The crucible contained 25.7 cm^3 of pure tin. A band heater attached to the top portion of the crucible, allowing the upper portion of tin to be heated above its melting point. The crucible rested in a water-cooled aluminum chamber. The circulating water cooled the bottom of the crucible, allowing the lower portion of tin to remain at a temperature below its melting point. This selective heating and cooling kept the tin in a steady two-phase state. Since the thermal conductivity of the tin and graphite is relatively high, a horizontal solidification profile was maintained. By varying the combination of heating and cooling, the solidification profile could be moved vertically by several centimeters.

A tree of eight chromel-alumel thermocouples was mounted inside the crucible. These were used to measure the temperature at various points, allowing the position of the solidification front to be monitored. The horizontal spacing between the thermocouples was 5.6 mm, with the thermocouple tree having a 45^o inclination with respect to the horizontal, as shown in Figure 4-3. This positioning had the tip of each thermocouple in line with the γ-ray beam as it penetrated the crucible.

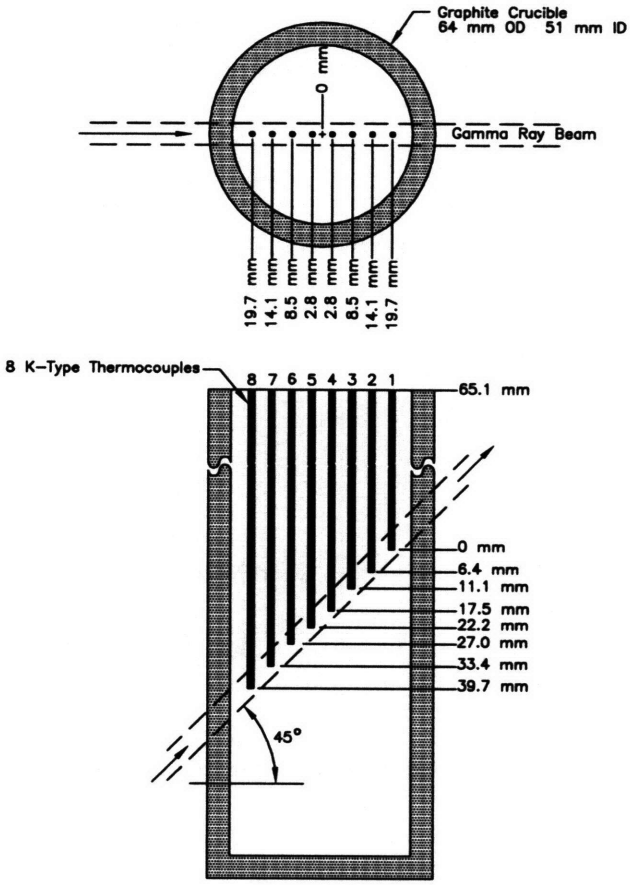

Figure 4-3: Schematic of Thermocouple and Gamma-Ray Positions relative to Crucible

Pure tin was chosen as the test medium for four principal reasons. First, the melting temperature of tin is 232°C. This relatively low temperature allows for simpler hardware design and power requirements. Second, pure tin is a relatively stable and non-reactive element, again simplifying the hardware and control of the experiment. Third, the solidification front in pure tin exists as a discrete interface between the liquid and solid phases. The absence of a mushy zone reduces the uncertainty and error in any measurements. Finally, the density difference between the liquid and solid phases of pure tin is approximately 4%, as seen in Figure 4-4 [59]. The resolution of such a small density variation serve as a excellent system benchmark. If the density variation between the liquid and solid phases of pure tin can be determined, the transition to more common engineering materials–such as steel or aluminum with much larger (6% to 12%) variations–should not be difficult.

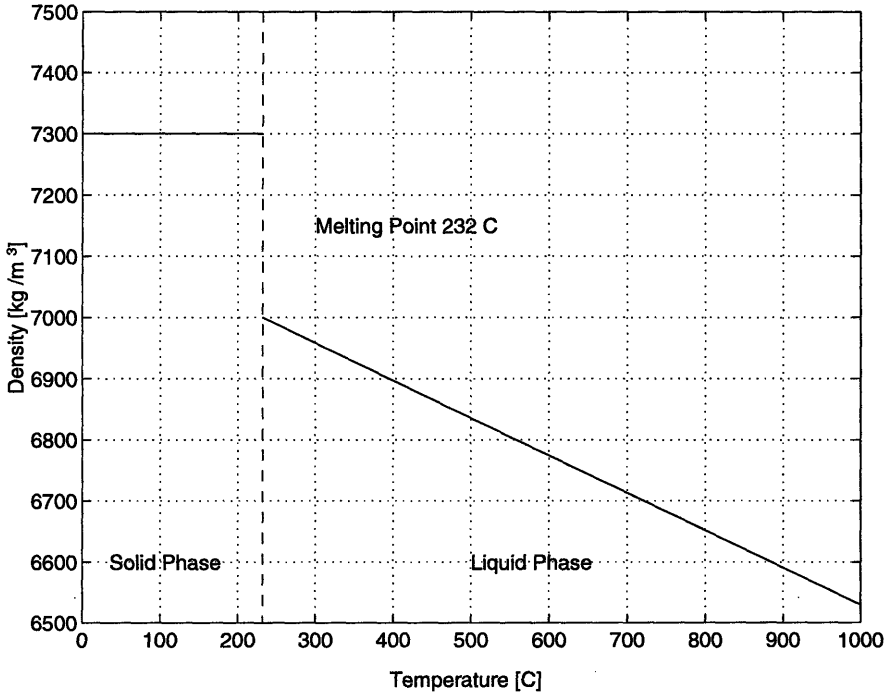

Figure 4-4: Plot of Pure Tin Density vs. Temperature

4.3 System Calibration

System calibration was conducted by removing the test-object and measuring the γ-ray attenuation through various known thicknesses of solid tin. Four trials were performed. The photon count was measured for an "open-beam" condition, and beam attenuation though 10 mm, 20 mm, and 30 mm of tin. For each trial, five samples were recorded, each over a 10 second time interval, and averaged. The results of the calibration are shown in Table 4.1.

Thickness, t [mm]	Mean Count, I	Deviation, σ
Free Beam	150,579	190
10	107,188	242
20	78,910	238
30	56,499	331

Table 4.1: Gamma-Ray Photon Count for Various Solid Tin Thicknesses

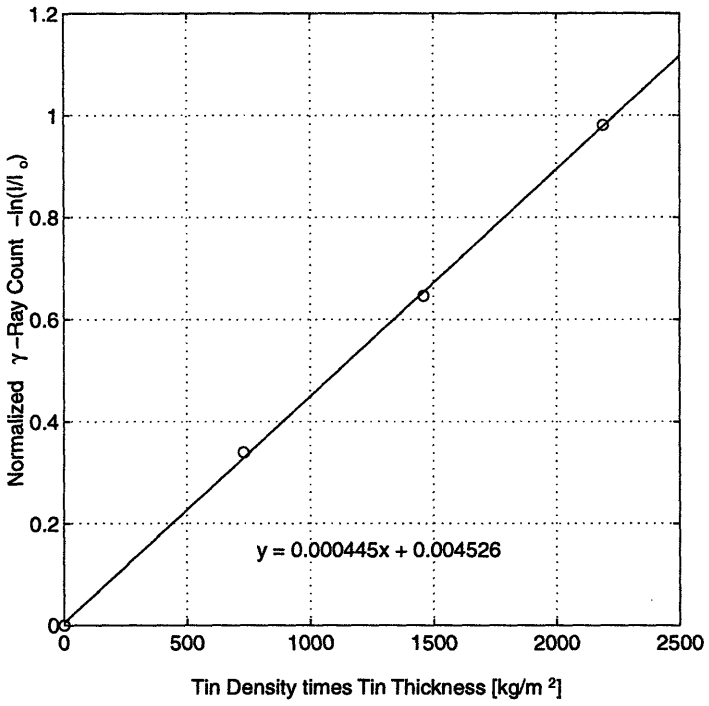

Figure 4-5: Data from Gamma-Ray Attenuation Calibration

Using the calibration data and rearranging Equation 3.7, the mass attenuation coefficient was experimentally measured:

$$\mu_{exp} = \frac{\ln\left(\frac{I_o}{I}\right)}{\rho x_{tin}} \tag{4.1}$$

The free beam count was taken as the value of the incident photon flux, I_o. For a solid tin density of 7300 kg/m^3, appropriate values of tin thickness, x_{tin}, and transmitted photon count, I, the natural logarithm of the normalized frequency count versus tin thickness time density were plotted in Figure 4-5. More detailed data are presented in Appendix C.

The linear relationship between these data is expected; the slope of the line is the mass attenuation coefficient of tin at a mean Co^{60} energy of 1.25 MeV. Experimentally, the mass attenuation coefficient was found to be 0.00445 m^2/kg. The expected value of the mass attenuation coefficient of tin at this energy is 0.00502 m^2/kg. This is an error of 11.4%. The lower than expected value for the mass attenuation coefficient is attributed to the detection of an excess of forward scattered radiation due to the use of an uncollimated detector. If scattered radiation were present in the measurement, a higher than normal transmitted photon count would result. If the value of I is higher than expected, the

value of $\ln(I/I_o)$ is lower than expected, resulting in a lower value for the mass attenuation coefficient.

4.4 Gamma-Ray Attenuation Method

4.4.1 Theoretical Analysis

The liquid path length is the thickness of the liquid tin through which the γ-ray photons travel. This length was calculated by using the basic γ-ray attenuation relations (Equations 3.7 and 3.8). However, since the γ-ray beam encountered other materials along its path, the transmitted photon count represented the total attenuation of the γ-ray beam through *all* these materials, including the graphite crucible, the aluminum cooling unit, the solid tin, *and* the liquid tin. Equation 3.8 was rearranged to compensate for this fact and to calculate the liquid path length, L_{liq_γ} using the γ-ray attenuation method. To begin, the transmitted photon count through the test-object with the crucible filled entirely with solid tin was defined as:

$$I' = I_o e^{(-\rho_{other}\mu_{other}x_{other} - \rho_{solid}\mu_{tin}L)} \tag{4.2}$$

Since the non-tin components of the test-object remain constant, their respective parameters can be lumped together. Thus, ρ_{other} is the lumped density of the non-tin components, μ_{other} is the lumped mass attenuation coefficient of the non-tin components, x_{other} is the lumped thickness of the non-tin components, ρ_{solid} is the density of solid tin, μ_{tin} is the mass attenuation coefficient of tin irrespective of phase, L is the total path through the crucible, and I_o is the free-beam or incident photon count. For the two-phase system, Equation 3.8 gives:

$$I = I_o \exp[-\rho_{other}\mu_{other}x_{other}] \exp[-\rho_{solid}\mu_{tin}L_{solid}] \exp[-\rho_{liquid}\mu_{tin}L_{liquid}] \tag{4.3}$$

where ρ_{liquid} is the density of liquid tin, L_{solid} is the solid phase thickness, and L_{liquid} is the liquid phase thickness. From the geometry of the system:

$$L_{solid} = L - L_{liquid} \tag{4.4}$$

By substituting Equation 4.2 and Equation 4.4 into Equation 4.3, we find:

$$I = I' e^{(\rho_{solid} - \rho_{liquid})\mu_{tin} L_{liquid}} \tag{4.5}$$

As a result, the liquid path length based on the γ-ray attenuation method is:

$$L_{liq_\gamma} = \left[\frac{1}{(\rho_{solid} - \rho_{liquid})\mu_{tin}}\right] \ln\left[\frac{I}{I'}\right] \tag{4.6}$$

So, the liquid path length can be calculated, given the density of the solid and liquid phases of tin, the mass attenuation coefficient of tin, and the transmitted photon count through a crucible filled with solid tin.

4.4.2 Experimental Results

Ten different sets of experiments were conducted. For each experiment, a different solidification front position was set, altering the liquid/solid fraction through which the γ-ray beam traveled. In addition, the transmitted photon count was averaged over a series of 10 samples for each experiment. For each sample, the photon count was measured over a 10 second time interval. The results of the experiments are presented in Table 4.2, with data presented in detail in Appendix C.

Experiment No.	Mean Count, I	Deviation, σ
1	7824.0	61.4
2	8359.0	78.9
3	7961.4	97.3
4	7917.3	75.2
5	7998.3	105.9
6	8125.1	87.7
7	8146.2	90.8
8	8013.1	95.4
9	7984.5	78.4
10	7978.1	58.9

Table 4.2: Gamma-Ray Photon Count for Various Liquid Tin Path Lengths

The value of I' was 7824, the experimentally determined value for a complete path of solid tin, as measured in experiment 1. The value of ρ_{solid} was 7300 kg/m^3. The value of μ_{tin} was 0.00445 m^2/kg, the experimentally determined value from the system calibration. Since the value of ρ_{liquid} is dependent on temperature, it varied from experiment to experiment since different fractions of liquid tin were present. As a result, an average value of ρ_{liquid} was calculated for each experiment, based on the average liquid tin temperature measured by the thermocouples. The average liquid temperature and liquid density for each experiment are shown in Table 4.3. Using these values, the liquid path lengths via the γ-ray attenuation method were calculated using Equation 4.6. These results are shown in Table 4.4. The average error in the liquid path lengths calculated using the γ-ray method was 6 mm. A breakdown of the raw data and intermediate calculations is presented in Appendix C.

Experiment No.	Average Liquid Phase Temperature [^{o}C]	Average Liquid Phase Density [kg/m^3]
1	42.0	N/A
2	384.5	6906.6
3	276.9	6972.5
4	274.8	6973.8
5	286.2	6966.8
6	301.7	6957.3
7	290.9	6963.9
8	281.0	6970.0
9	276.7	6972.6
10	276.6	6972.7

Table 4.3: Average Tin Density in Liquid Phase during Path Length Experiment

Experiment No.	Liquid Path Length, L_{liq_γ} [mm]
1	0.0
2	61.9
3	36.0
4	32.3
5	39.0
6	48.9
7	51.1
8	40.4
9	38.0
10	37.5

Table 4.4: Liquid Path Length Calculations based on Gamma-Ray Attenuation

4.5 Thermocouple Method

To confirm the liquid path lengths calculated using the γ-ray attenuation method, they were also calculated using the location of the solidification front and the crucible geometry. The vertical position of the solidification front was monitored by means of the thermocouple tree. The length, $x_{T_{high}}$, and temperature, T_{high}, of the first thermocouple located in the liquid phase were recorded. Likewise, the length, $x_{T_{low}}$, and temperature, T_{low}, of the first thermocouple located in the solid phase were recorded.

For example, if for a particular experiment the solidification front was located between thermocouples number 4 and 5, as shown in Figure 4-3, the value of T_{high} would be the temperature at thermocouple number 4. The value of T_{low} would be the temperature at thermocouple number 5. The value of $x_{T_{high}}$ would be 17.5 mm and the value of $x_{T_{low}}$ would be 22.2 mm. The position of the solidification front relative to thermocouple number 1, x_{sf}, was determined by interpolation:

$$x_{sf} = \left(\frac{T_{high} - T_{melt}}{T_{high} - T_{low}}\right)(x_{T_{low}} - x_{T_{high}}) + x_{T_{high}} \tag{4.7}$$

where T_{melt} is the melting temperature of pure tin. Once the position of the solidification front was determined, the liquid path length was calculated based on the geometry of the

crucible:

$$L_{liq_{TC}} = \frac{x_{sf}}{\sin\theta} + \frac{5.6}{\cos\theta} \quad [mm] \tag{4.8}$$

where θ is the thermocouple inclination angle relative to the horizontal. A simple schematic of the liquid path length relative to the crucible geometry is shown in Figure 4-6. For each experiment, the liquid path lengths were calculated using the thermocouple method. These values and relevant measured parameters are shown in Table 4.5. The average error in the liquid path lengths calculated using the thermocouple method was 0.46 mm. A breakdown of the raw data and intermediate calculations is presented in Appendix C.

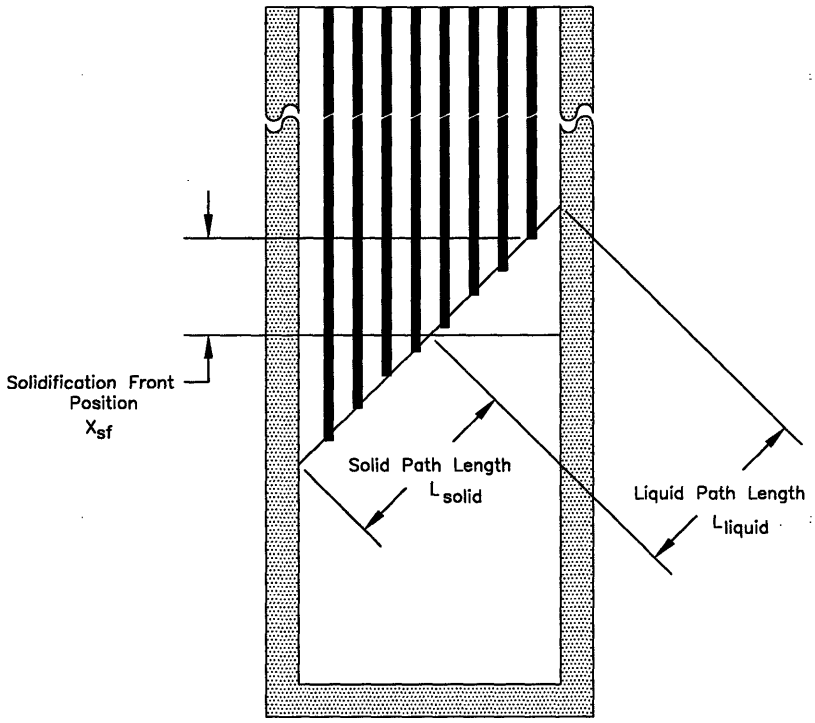

Figure 4-6: Diagram of Liquid/Solid Path Lengths based on Thermocouple Measurements

Experiment No.	High Thermocouple Value, T_{high} [°C]	Low Thermocouple Value, T_{low} [°C]	High Thermocouple Length, $x_{T_{high}}$ [mm]	Low Thermocouple Length, $x_{T_{low}}$ [mm]	Solidification Front Position, x_{sf} [mm]	Liquid Path Length, $L_{liq_{TC}}$ [mm]
1	42	42	N/A	N/A	All Solid	0
2	439	330	N/A	N/A	All Liquid	71.8
3	258.7	226.0	17.5	22.2	21.3	38.0
4	253.3	223.3	17.5	22.2	20.8	37.3
5	247.1	223.9	22.2	27.0	25.3	43.7
6	232.4	214.6	33.4	39.7	33.5	55.3
7	232.1	217.5	27.0	33.4	27.0	46.1
8	234.3	218.5	22.2	27.0	22.9	40.3
9	258.1	226.8	17.5	22.2	21.4	38.2
10	257.7	226.6	17.5	22.2	21.4	38.2

Table 4.5: Liquid Path Length Calculations based on Thermocouple Temperature and Position

Figure 4-7 plots the liquid path lengths measured using the γ-ray attenuation method against those measured using the thermocouple method. The theoretical prediction is a one-to-one correlation between the two measurements, indicated by the 45^o line in the plot. Taking into account the statistical error in the γ-ray count technique, the results of the experiment are very good. The measurement technique correctly predicted the liquid path length and showed the proper trend. These data are extremely good in light of the large amount of error present in the system, including misalignments of the γ-ray beam with the thermocouple tree and the use of an uncollimated detector. These positive results validate the use of photon attenuation through two-phase metals to distinguish density differences. Consequently, the results of this experiment provide the groundwork and motivation for further work using this technique–the application of CT.

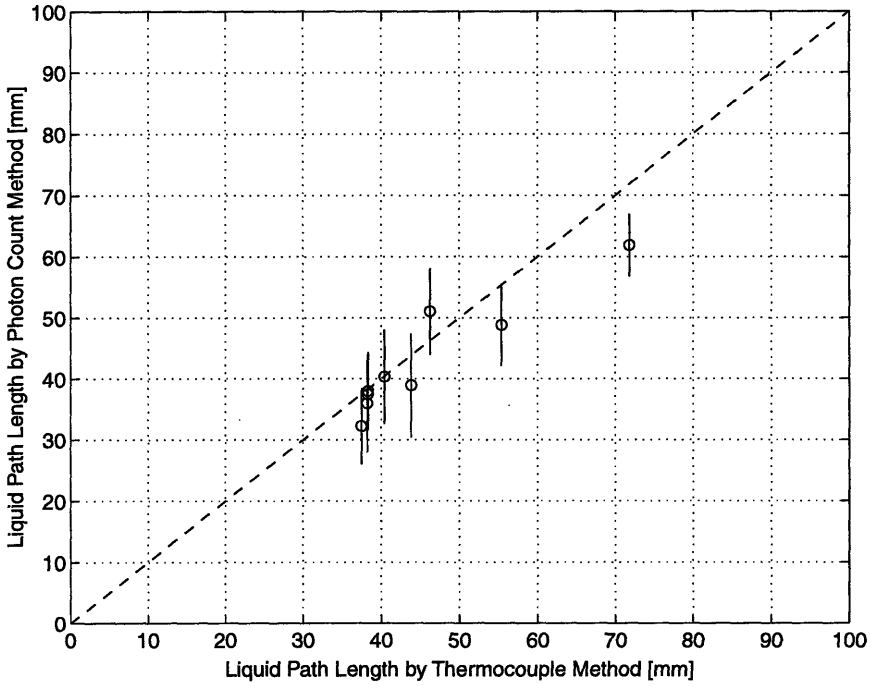

Figure 4-7: Comparison of Liquid Path Length Calculations

Chapter 5

Tomographic Imaging Experiments

Several experiments were carried out to increase understanding of the performance characteristics of a tomographic imaging system. They also addressed the feasibility of using this technology to monitor the solidification front in metal castings. The same equipment was used to conduct all the experiments, as shown in Figure 5-1. It was comprised of the Co^{60} radioisotope and NaI detector, described in Chapter 4, in addition to a positioning stage and data acquisition program, forming a first-generation tomographic imaging system. The source collimation was 6 mm and the detector collimation was 2 mm. The equipment was mounted on a three-tiered table. This allowed the location of the positioning stage to be changed relative to the source and detector, which were fixed. The FBP algorithm was used to reconstruct the tomographic images from the projection data. Unless specifically noted, a ramp filter with a cutoff frequency of 0.9 was used in all the image reconstructions. This choice of filter and high cutoff frequency gives the best edge detection and spatial resolution. Five main experiments were conducted using this tomographic system. The experiments were performed in progression. The first three tests attempted to define the performance parameters of the system, as well as to identify the basic relationships of these parameters and their limits or trade-offs. The final two tests used this system to monitor solidification in metals, and illustrate various consequences and drawbacks of such a system.

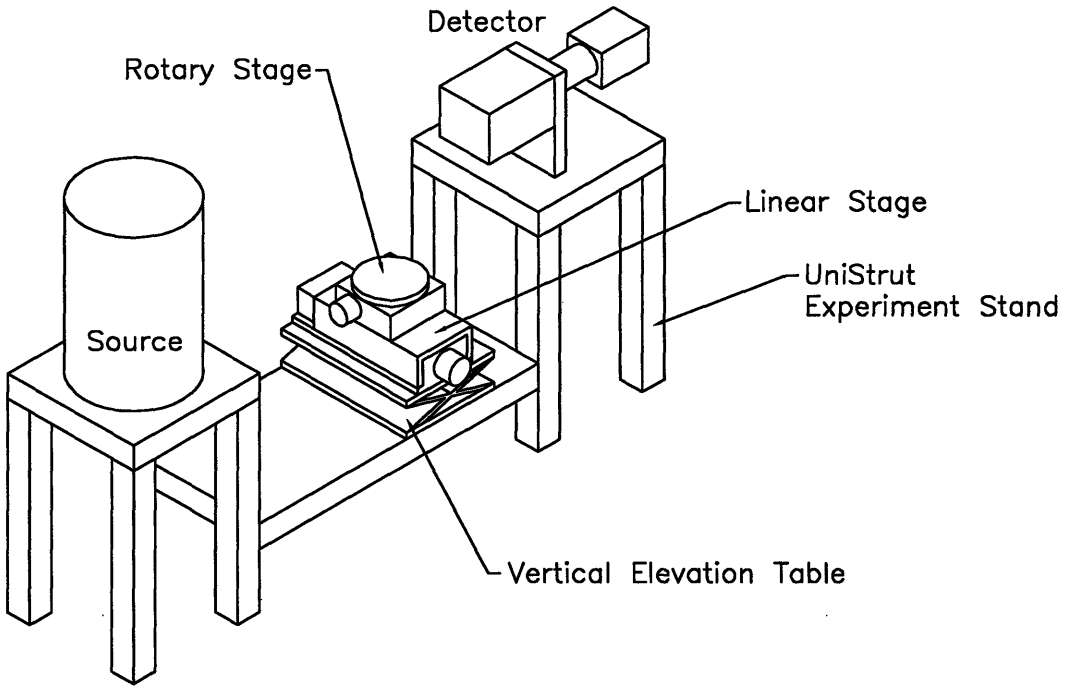

Figure 5-1: Schematic of Equipment Layout for Tomographic Imaging Experiments

5.1 Experimental Apparatus

The experimental first-generation CT system was comprised of a radiation source and detector, a position stage, and a data acquisition and control system. The source and detector were identical to those used for the γ-ray attenuation measurement experiments, as described in the previous chapter. The photon count measurement system and temperature measurement system for the tomography system were integrated into a single data acquisition program. In addition, the program had a motor control system to move an integrated positioning stage and manipulate a test-object for CT scanning. The components of the CT system are described in this chapter.

5.1.1 Positioning Stage

To conduct the data acquisition for the tomographic imaging experiments, a positioning stage was used to move the test-object relative to the γ-ray source and detector. The stage was composed of a motorized rotary table mounted to a motorized horizontal translation

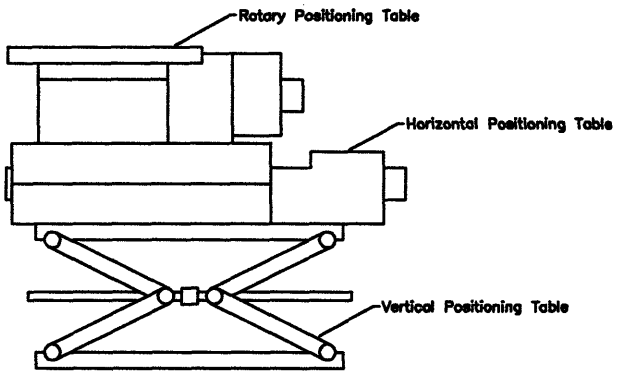

Figure 5-2: Schematic of Positioning Stage Used for Tomographic Experiments

table mounted to a manual vertical translation table, as shown in Figure 5-2. The rotary table was a New England Affiliated Technologies RT-4-SM model with a 99 mm diameter platform. The minimum angular step size was 0.02^o, with an accuracy of 3.0 minutes and a repeatability of 0.6 minutes. The table was driven by a 5 volt, 50 oz-inch stepper motor operating at 200 steps per revolution. The horizontal translation table was a New England Affiliated Technologies TM-800-SM model with a travel span of 203 mm. The table was also driven by a 5 volt, 50 oz-inch stepper motor operating at 200 steps per revolution. The lead screw had a pitch of 2 mm. The horizontal translation table had a resolution of 0.01 mm. The vertical translation table was a Newport model 281 laboratory jack with a range of 76 mm and 3 mrad parallelism. Positioning was performed by manually turning the table's leadscrew. There was no need to automate the vertical positioning since only two-dimensional tomographic cross-sections through a single set height were recorded. The positioning stage was leveled and mounted so that the test-object could be moved perpendicular to the path of the γ-ray beam.

5.1.2 Data Acquisition and Control

There were three main parts of the data acquisition and control system, as shown in Figure 5-3. They were the positioning stage control subsystem, the photon count measurement subsystem, and the temperature measurement subsystem. All three subsystems were incorporated into a single control program written in Microsoft C and executed on a Gateway 2000 Model P5-100 100 MHz Pentium PC compatible computer. The code for the control

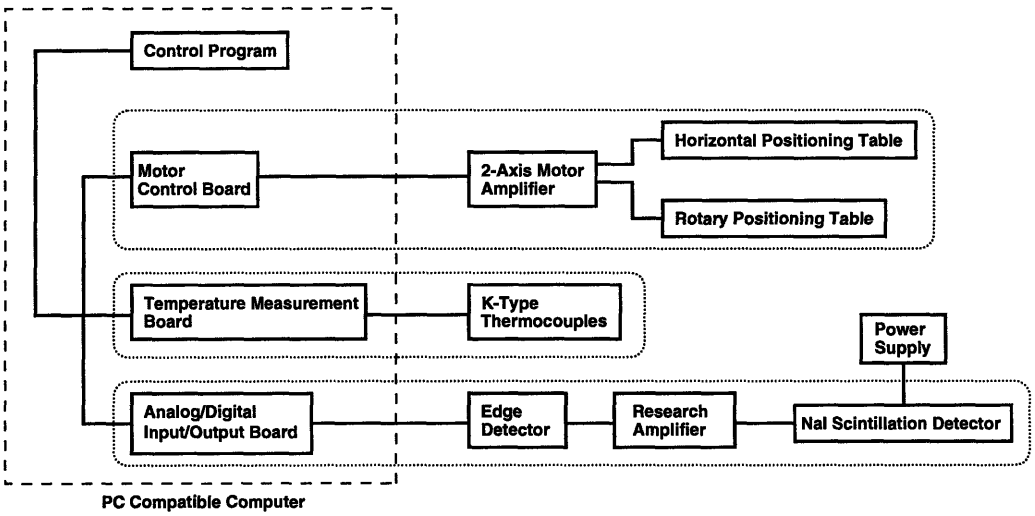

Figure 5-3: Diagram of the Components of the Data Acquisition and Control System

program is documented in Appendix E.

Positioning Stage Control Subsystem

The positioning stage control subsystem was composed of a NuLogic 2-axis NuDrive stepper motor amplifier, a NuLogic PCStep motion control board, and the aforementioned control program. The two stepper motors driving the rotary and horizontal positioning tables were connected to the amplifier and operated with the motor controller card. An open-loop control scheme was used. A travel distance was specified by the operator in either inches or degrees, depending on the motor axis, and was converted to steps by the control routine. The appropriate motor was incremented by this amount at a preset velocity and acceleration. The system allowed the positioning stage to be moved in well-defined increments with respect to a fixed origin.

Photon Count Measurement Subsystem

Since the same radioisotope source was used, the photon count measurements were again performed in pulse mode using the Keithly-Metrabyte DAS-1601 analog-digital input-output board. The intensity of the γ-ray beam was determined by measuring the photon count over a chosen count time and recording it using a separate function within the customized control program.

Temperature Measurement Subsystem

The data acquisition for temperature measurements was again performed using Omega chromel-alumel (K-type) thermocouples in conjunction with a Keithly-Metrabyte DAS-TC data temperature measurement board. However, the software supplied with the DAS-TC board was not used. The temperatures were measured over the same time interval as the photon count and recorded using a separate function within the customized control program.

5.1.3 Tomographic Reconstruction Algorithms

The two-dimensional tomographic images of the test-objects were reconstructed using a FBP algorithm written in Fortran. The tomographic images were displayed and analyzed using the Matlab matrix manipulation software package. Both programs were executed on a Sun Sparcstation 5 computer with a UNIX operating system. The FBP algorithm and image processing routines were developed by Shi [57]. The reconstruction program allows the user to specify the cut-off frequency and the mathematical order of one of five filters (ramp, hamming, hann, Parzen, or Butterworth) for the FBP algorithm.

5.2 Object Position Effects on System Performance

The first experiment carried out using this tomographic imaging system was a simple scan across a rectangular aluminum block. Figure 5-4 shows a schematic of the experimental setup. The aluminum block was 24 mm wide by 53 mm long, with the incident photon beam perpendicular to the 24 mm face. Four different scans were carried out using different source-to-object positions. For each scan, a single projection was recorded by moving the block across the beam in 0.25 mm increments over a 51 mm span. The photon attenuation at each of these 200 positions was recorded, with each measurement taken over a 240 second count time. The four source-to-object positions used were 367 mm, 292 mm, 194 mm, and 118 mm. The results of this experiment provided information regarding the spatial and contrast resolution capabilities of the CT system.

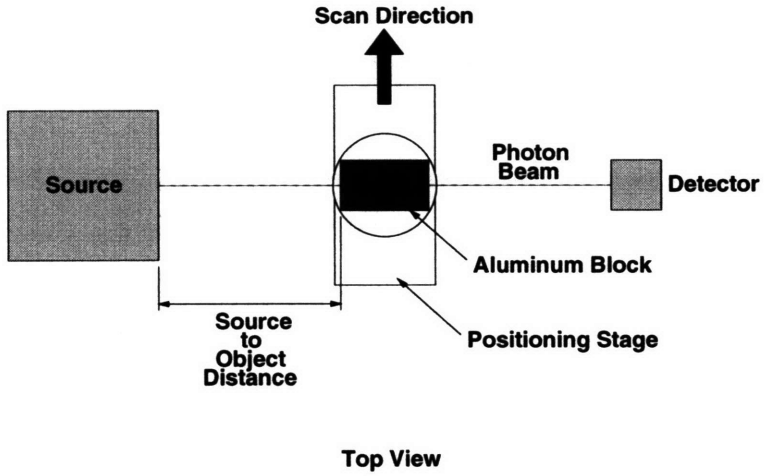

Figure 5-4: Schematic of Experimental Setup for Scans Across Aluminum Block

5.2.1 Experimental Results

The photon attenuation versus position, defined as a projection, for the four scans is shown in Figure 5-5. The photon attenuation has been normalized according to Equation 3.10. The average maximum and minimum values of each projection are shown. The maximum value represents the normalized photon attenuation through the aluminum block, while the minimum value represents the normalized photon attenuation through air. In addition, the slope of the edge response rise and fall is indicated. Figure 5-6 compares the results of the four experimental scans to the theoretical response across an aluminum block with the same given dimensions. The theoretical response was calculated using Equation 3.7. Rearranging reveals:

$$g(s,0) = \ln \frac{I_o}{I} = \rho \mu x \tag{5.1}$$

For the open beam position, the incident photon count is the same as the transmitted photon count, since attenuation through air is negligible. As a result, the normalized projection value is zero. For the beam position through the aluminum block, the density ($\rho = 2.780$ g/cm^3), the mass attenuation coefficient ($\mu = 0.0550$ cm^2/g), and the thickness ($x = 53.3$ mm) of the aluminum block are all known. As a result, the normalized projection value through the block was calculated to be 0.795. The theoretical response is approximately 16% higher than the largest maximum average response for the four scans. The primary source of this error is attributed to the detection of systematic background radiation and scattered radiation, both of which would lower the normalized projection value.

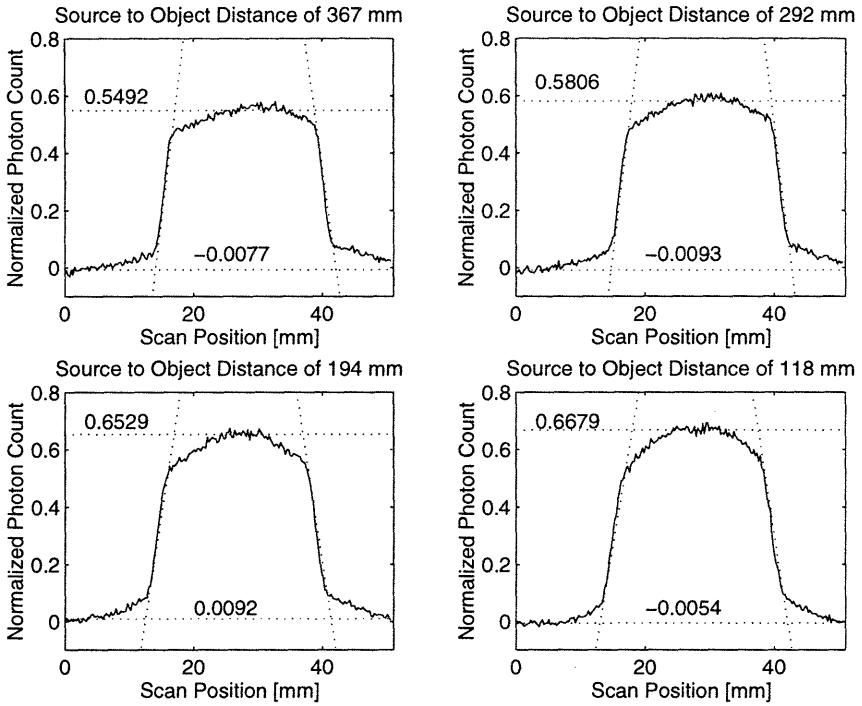

Figure 5-5: Edge Response Across Aluminum Block for Various Source-to-Object Positions

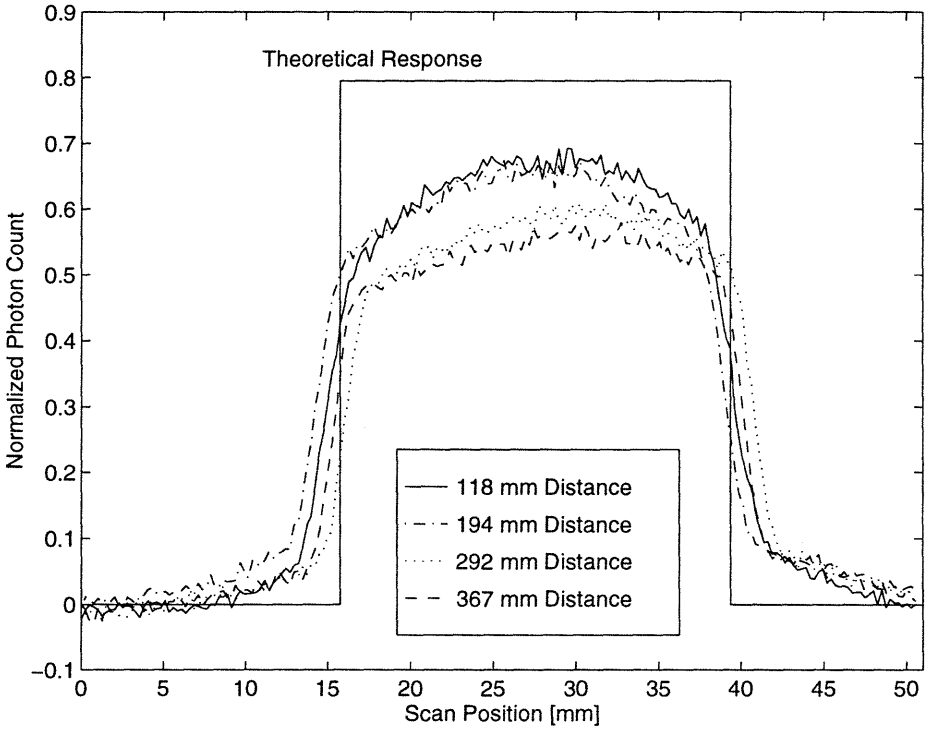

Figure 5-6: Comparison of Edge Responses with Theoretical Prediction

5.2.2 Spatial Resolution Effect

The spatial resolution of the CT system was estimated by analyzing the edge response–the scan distance over which the photon attenuation rises or falls from its minimum value to its maximum value–across the aluminum block. For the theoretical response, the spatial resolution is infinitely small because an infinitesimal beam width was assumed. This results in a completely vertical edge response rise. In reality of course, the photon beam has a finite width. Thus, the experimental results shown an edge response rise with a finite slope. The spatial resolution of the system was calculated using this slope.

A linear curve fit was performed to find the line which best matches the slope of the edge response rise and fall. The step size required to rise from the minimum average projection value to the maximum average projection value was calculated from the curve fit for the leading edge. Likewise, the step size required to fall from the maximum average projection value to the minimum average projection value was calculated from the curve fit for the trailing edge. The average of these step sizes represents an average spatial resolution for the system. This method of calculating the spatial resolution was performed for each of the four scans. The results are shown in Table 5.1.

Source-to-Object Position [mm]	Leading Edge Rise Size [mm]	Trailing Edge Fall Size [mm]	Average Spatial Resolution [mm]
367	3.0	3.4	3.2
292	3.2	3.2	3.2
194	4.4	4.3	4.4
118	5.0	4.5	4.8

Table 5.1: Measured Spatial Resolution for Various Source-to-Object Positions

As evident from the experimental data, the spatial resolution predictably increases as the source-to-object distance increases. As described by Hughes [32], the profile of the photon beam defines the spatial resolution of a CT system. The spatial resolution is roughly equivalent to the beam width at the point at which it is incident to the object. This beam profile is a function of the collimation of the source and detector. Considering the geometry and collimation of the source and detector, there is a position of minimum beam width between the source and detector, known as the half-power crossover point, as shown in Figure 5-7. Hughes argues that the half-power crossover point is the position which has the

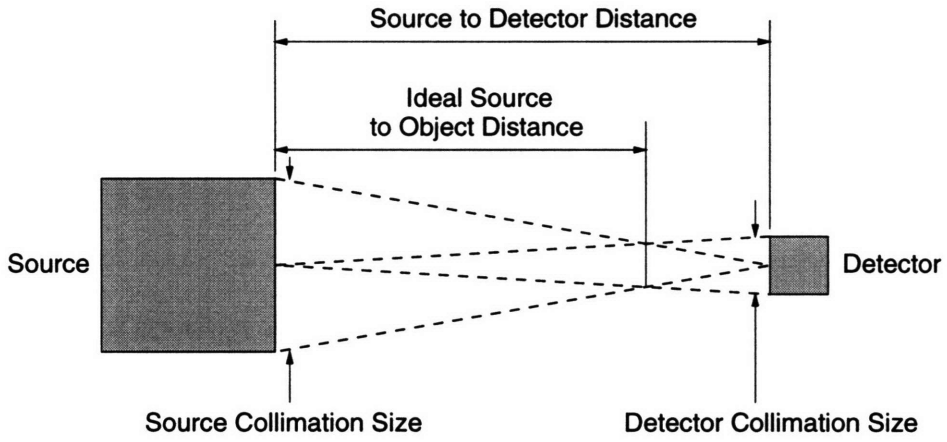

Figure 5-7: Source/Detector Geometry Effect on Photon Beam Width

best beam sensitivity profile, and that it is, consequently, the optimum object position to maximize spatial resolution.

As presented by Hughes, the beam width at the half-power crossover point, $BW_{crossover}$, is:

$$BW_{crossover} = \left(\frac{S}{S+D}\right) D \tag{5.2}$$

and the location of the half-power crossover point from the source, $Y_{crossover}$, is:

$$Y_{crossover} = \left(\frac{S}{S+D}\right) L \tag{5.3}$$

where S is the source size or collimation, D is the detector size or collimation, and L is the distance from source to detector. In addition, the beam width at any position between the source and detector is:

$$BW = \left(\frac{L-Y}{L}\right) S \tag{5.4}$$

$$\text{for } Y < Y_{crossover}$$

and:

$$BW = \left(\frac{Y}{L}\right) D \tag{5.5}$$

$$\text{for } Y > Y_{crossover}$$

For the CT system in question, the source collimation was 6 mm and the detector

collimation was 2 mm. The distance from source to detector was 600 mm. Using Equations 5.2 and 5.3, the optimum beam width for the experimental system was found to be:

$$BW_{crossover} = 1.5 \text{ mm}$$

and the optimum source-to-object position for the experimental system was found to be:

$$Y_{crossover} = 450 \text{ mm}$$

In addition, by using Equations 5.4 and 5.5, the theoretical beam width as a function of source-to-object position was compared to our experimental measurements. This result is shown in Figure 5-8. The experimental measurements of the spatial resolution compare well with the theoretical prediction.

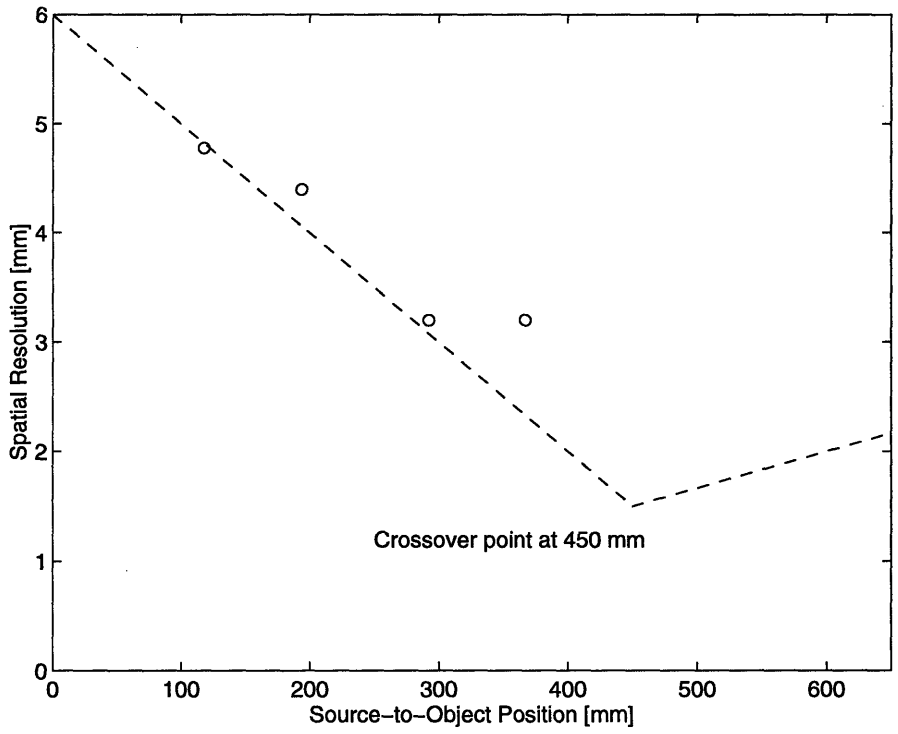

Figure 5-8: Comparison of Experimentally Determined Spatial Resolution with Theoretical Prediction

5.2.3 Contrast Resolution Effect

The contrast resolution of the experimental CT system was calculated using Equation 3.16. For our case, $\mu_{background}$ is the linear attenuation coefficient through air and μ_{object} is the linear attenuation coefficient through aluminum. As shown in Figure 5-6, the photon attenuation through the aluminum block decreases as the source-to-object distance increases. Consequently, the linear attenuation coefficient of aluminum will also decrease as the source-to-object distance increases. The experimentally determined linear attenuation coefficients through the aluminum for each of the four scan positions, as well as the contrast resolution percentage, are shown in Table 5.2. The linear attenuation coefficient through air was taken to be 6.918×10^{-5} cm^{-1}.

The extremely large values for the contrast resolution percent are to be expected since the difference in density between aluminum and air is extremely high. Ignoring the magnitude of the figures, it is evident that the contrast resolution of the system decreases as source-to-object distance increases. The contrast resolution is proportional to the linear attenuation coefficient of aluminum. The decrease in the linear attenuation coefficient with position is a direct result of the detection of a larger fraction of scattered radiation. This phenomenon is shown in Figure 5-9. At long source-to-object distances, a larger fraction of scattered radiation will intercept the detector and thus lower the contrast resolution of the system.

Source-to-Object Position [mm]	Linear Attenuation Coefficient for Aluminum [cm^{-1}]	Contrast Resolution [%]
118	0.1030	148,787
194	0.1088	157,171
292	0.1224	176,830
367	0.1252	180,877

Table 5.2: Measured Linear Attenuation Coefficient for Aluminum for Various Source-to-Object Positions

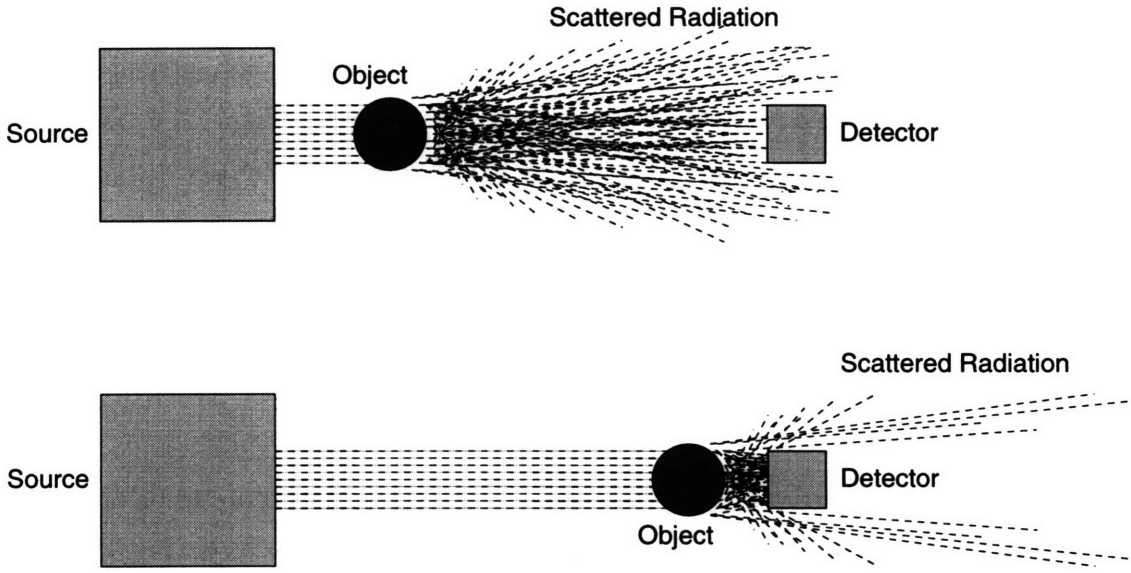

Figure 5-9: Object Position Effect on Detected Scattered Radiation

There is an obvious trade-off between spatial resolution and contrast resolution of the CT system based on the source/detector/object position and geometry. As determined by the edge response experiments, a short source-to-detector distance produces better contrast resolution because of the lower amount of scattered radiation incident to the detector. However, a long source-to-detector distance produces better spatial resolution because of the crossover point of the photon beam, which is based on source/detector geometry.

5.3 Image Reconstruction of an Aluminum Block

Once the spatial resolution and contrast resolution capabilities of the experimental system were evaluated, a tomographic image of the aluminum block was reconstructed. The block from the previous experiment was used in the reconstruction. The system setup is shown in Figure 5-10. The source-to-object distance was 194 mm. This position gave a reasonable trade-off between the spatial and contrast resolutions of the system. Projection measurements were taken at a height through the middle of the block. A step size of 2.4 mm was used for the transverse measurements and a step size of 2.5^o was used for the view angles. There were 32 transverse steps and 72 view angles. The ratio of N_θ to N_s was 2.25, sufficient for application of the FBP algorithm, as determined by Equation 3.17. The photon count

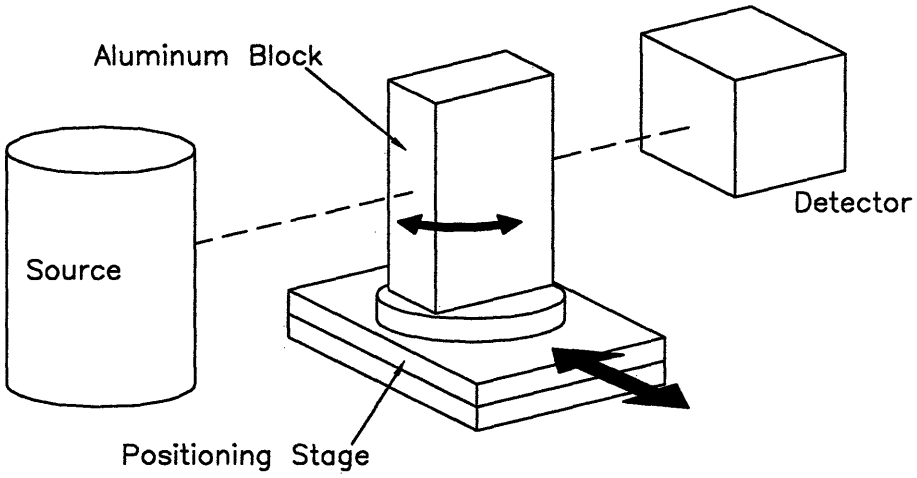

Figure 5-10: Schematic of Setup for Imaging of Aluminum Block

time for each measurement was 240 seconds. This count time produced a photon count range within the data set of 21884 to 10820. The overall data acquisition time for the entire data set was approximately 7 days.

5.3.1 Experimental Results

The reconstructed image of the aluminum block is shown in Figure 5-11. The block geometry is defined by some blurring along the edges. The dimensions of the block image are roughly 9 to 11 steps by 20 to 24 steps. This translates to a size of 23.8±2.4 mm by 52.4±4.8 mm. This compares quite well with the actual block size of 24 mm by 53 mm, and the expected spatial resolution of 4.4 mm. Based on the high photon count, the noise in the image is relatively low. The main problem with the image is the streaking at the top and bottom edges of the block. These are an artifact, generated by an improperly centered rotation plane, which can be corrected.

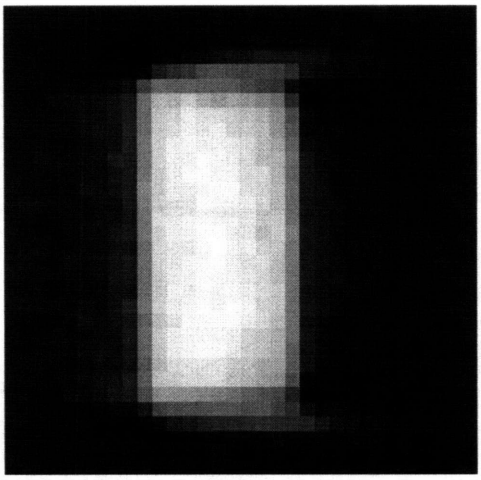

Figure 5-11: Reconstructed Image of an Aluminum Block. Parameters: 240 second count time, 32 transverse steps, 2.4 mm transverse step size, 72 view angles, first order ramp filter, 0.9 cutoff frequency

5.3.2 Sampling Size Effects

With the data set generated using a scan with 32 transverse steps and 72 view angles, the effect of data set size on image quality was examined. As mentioned previously, proper reconstruction using the FBP algorithm requires that the ratio of the number of view angles to the number of transverse steps be greater than or equal to $\pi/2$, as given by Equation 3.17. The given data set was manipulated using software (see Appendix E) to produce data sets with fewer view angles. The number of transverse steps was maintained at 32. Five different undersampled data sets were produced, having 9, 12, 18, 24, and 36 view angles. These represented a view angle step size of 20^o, 15^o, 10^o, 7.5^o, and 5^o, respectively. None of the altered data sets satisfied the FBP criterion of Equation 3.17. The FBP reconstruction was performed, and the five undersampled images are shown in Figure 5-12 along with the original image having 72 view angles.

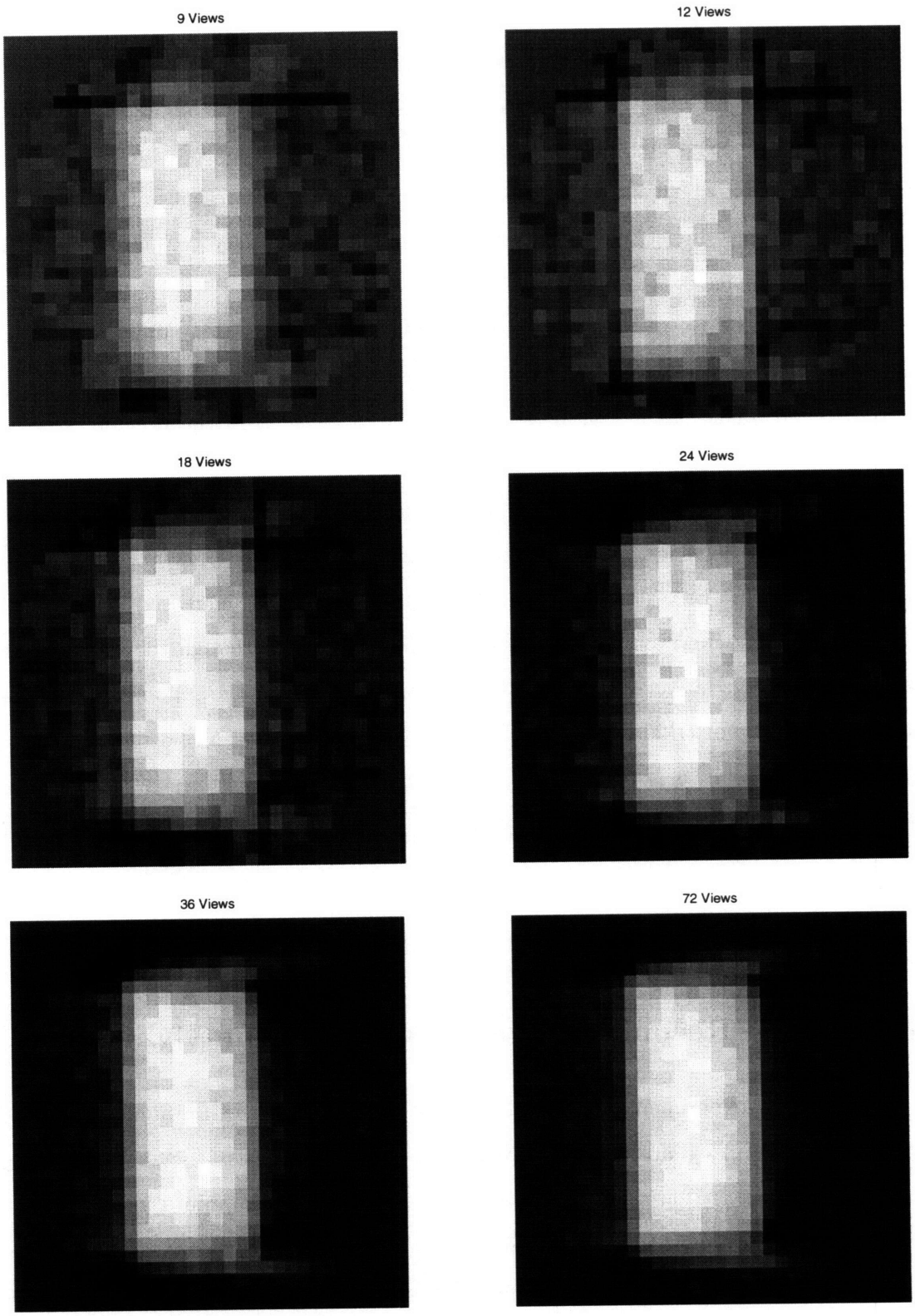

Figure 5-12: Effect of Changing Number of View Angles on Reconstructed Image of Aluminum Block. Parameters: 240 second count time, 32 transverse steps, 2.4 mm transverse step size, first order ramp filter, 0.9 cutoff frequency, number of view angles as indicated.

Figure 5-12 illustrates that as the number of view angles decreases, so does the overall image quality. When only 9 view angles were used, the aluminum block geometry is undefined and the edges are undetectable. With 12 and 18 view angles, the block edges become defined, but a high degree of noise and streaking is present. Using 24 view angles, the image streaking begins to disappear, but some noise is still present in the interior of the block. At 36 view angles, although still undersampled, the image compares well with the fully sampled image of 72 view angles.

This initial CT reconstruction of an aluminum block verifies the ability of the experimental system to adequately reproduce an object of known size and shape. In addition, the reconstructed image has a spatial resolution in accordance with the previous experimental analysis. This experiment proves the functionality of the experimental CT system and provides the groundwork for further object imaging.

In addition, the effects of using data sets with undersampled view angles were seen to be detrimental to the overall image quality, producing steaks, increased noise, and poor object definition. However, a good image was produced even though the ratio of number of view angles to transverse steps was lower than the required $\pi/2$. A undersampled data set having a ratio of 1.125 produced an image of similar quality to that of a fully sampled data set. As a result, it is evident that undersampling the number of view angle to a small degree would save on overall data acquisition time and system performance speed, while still producing images of adequate quality. In this case, reducing the amount of view angles from 72 to 36 resulted in data acquisition time being cut in half.

5.4 Image Reconstruction of an Aluminum Cylinder

The second CT experiment performed was the reconstruction of an aluminum cylinder. Imaging a uniform cylindrical object was important since it has the same geometry as future test objects. However, future test objects, such as a graphite crucible filled with two-phase tin, have more complicated internal structures. Consequently, performing a CT reconstruction of a simple, uniform, solid aluminum cylinder establishes a system performance baseline. As was the case with the reconstruction of the aluminum block, this experiment served to test that the CT system functioned properly.

The setup of this experiment is shown in Figure 5-13. The aluminum cylinder had

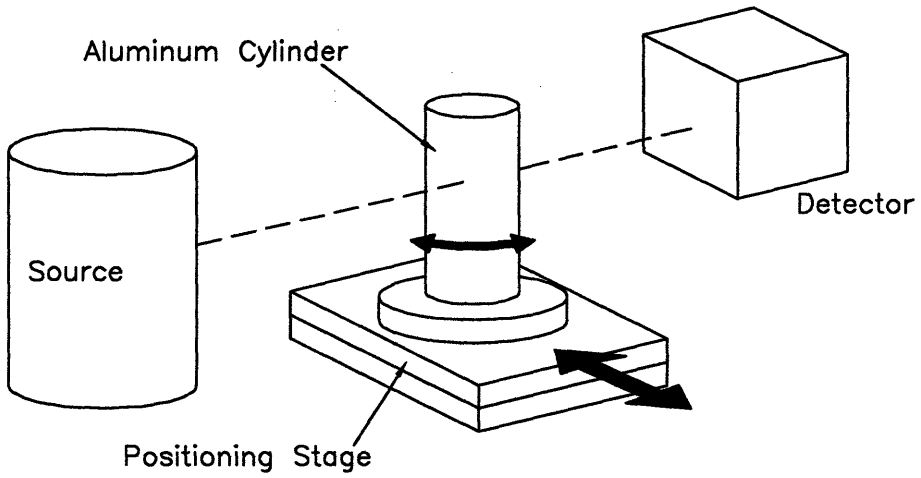

Figure 5-13: Schematic of Setup for Imaging of Aluminum Cylinder

an outside diameter of 64 mm. The source-to-object distance was 215 mm. Projection measurements were taken at a height through the middle of the cylinder. A step size of 1.9 mm was used for the transverse measurements and a step size of 2.5^o was used for the view angles. There were 47 transverse steps and 72 view angles. The ratio of N_θ to N_s was 1.53. This is just under the minimum specified value of 1.57 for proper reconstruction using the FBP technique. However, no discernible image quality dropoff was detectable in the previous experiment on the aluminum block when the ratio dropped from 2.25 to 1.125. Consequently, the minimal undersampling during this experiment should not produce any noticeable image degradation. Meanwhile, overall data acquisition time was decreased since fewer measurements were taken. The photon count time for each measurement was 240 seconds. This count time produced a photon count range within the data set of 21958 to 9770. The overall data acquisition time for the entire data set was approximately 10 days.

5.4.1 Experimental Results

The reconstructed image of the aluminum cylinder is shown in Figure 5-14. The cylinder geometry is very well defined. The outside diameter of the cylinder is roughly 33 to 35 steps. This translates to a size of 64.8±1.9 mm. This compares very well with the actual cylinder diameter of 64 mm. The contrast between the aluminum and air is very distinct,

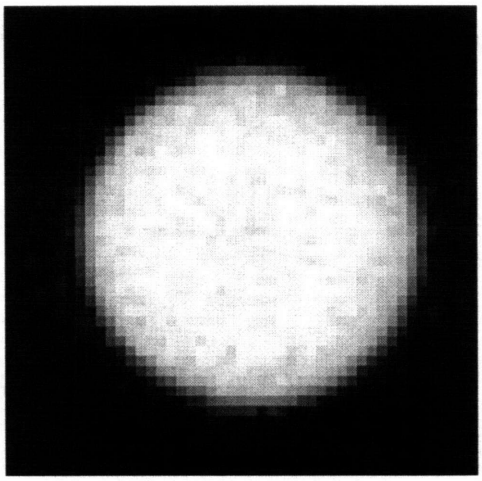

Figure 5-14: Reconstructed Image of an Aluminum Cylinder. Parameters: 240 second count time, 47 transverse steps, 1.9 mm transverse step size, 72 view angles, first order ramp filter, 0.9 cutoff frequency

but the image is not completely uniform within the aluminum cylinder, as we would expect. This variation does not have any discernible pattern. Thus, it does not appear to be an artifact, as may be encountered by such an effect as beam-hardening. The variation is entirely attributed to the statistical error from the photon count, appearing as noise in the image. A second set of experiments was carried out to examine the degree to which this noise affects the image.

5.4.2 Sampling Time Effects

As discussed in Chapter 3, noise in a CT image can be decreased by increasing the number of photon counts. To examine the effect of photon count on image quality, three additional experiments were conducted with the aluminum cylinder. Each of the experiments was identical to the one described in the previous section, with the exception of count time. The count time per measurement was 60 seconds, 120 seconds, and 180 seconds for the first, second, and third experiment, respectively. For the first experiment, the photon count within the data set varied from 5621 to 2393. For the second experiment, it varied from 11026 to 4848. For the third experiment, it varied from 16547 to 7303. Each of the three

data sets was reconstructed. Figure 5-15 shows the images of the aluminum cylinder, along with the previous reconstruction (which had a count time of 240 seconds per measurement).

The progression of the four images shows that the variation within the aluminum cylinder decreases as count time increases. This effect is primarily evident when comparing the 60 second count time image to the 240 second count time image. The decrease in noise with increased count time occurs because a larger number of photons are measured, thus reducing the statistical uncertainty of the count itself. As the error in the count measurement decreases, the noise in the image decreases. However, as count time becomes longer and longer, the amount of decrease in the uncertainty becomes smaller and smaller.

As described in Chapter 3, the statistical standard deviation in the photon count is equal to the square root of the mean:

$$\sigma = \sqrt{n} \tag{5.6}$$

As a result, the error is the standard deviation of the measurement divided by the measurement itself:

$$Error = \frac{\sqrt{n}}{n} = n^{-1/2} \tag{5.7}$$

By applying Equation 5.7 to the high and low photon count measurements for each of the four experiments, an error distribution of the photon count was plotted in Figure 5-16. As seen from the graph, the error in the photon count decreases with increased photon time. However, the error is proportional to time to the $-\frac{1}{2}$ power. For these results, the curve fit is:

$$Error = 1.69t^{-\frac{1}{2}} \tag{5.8}$$

Consequently, there is a diminishing return on the amount by which the error decreases. Also, as count time is increased, the overall data acquisition time is increased, degrading system performance.

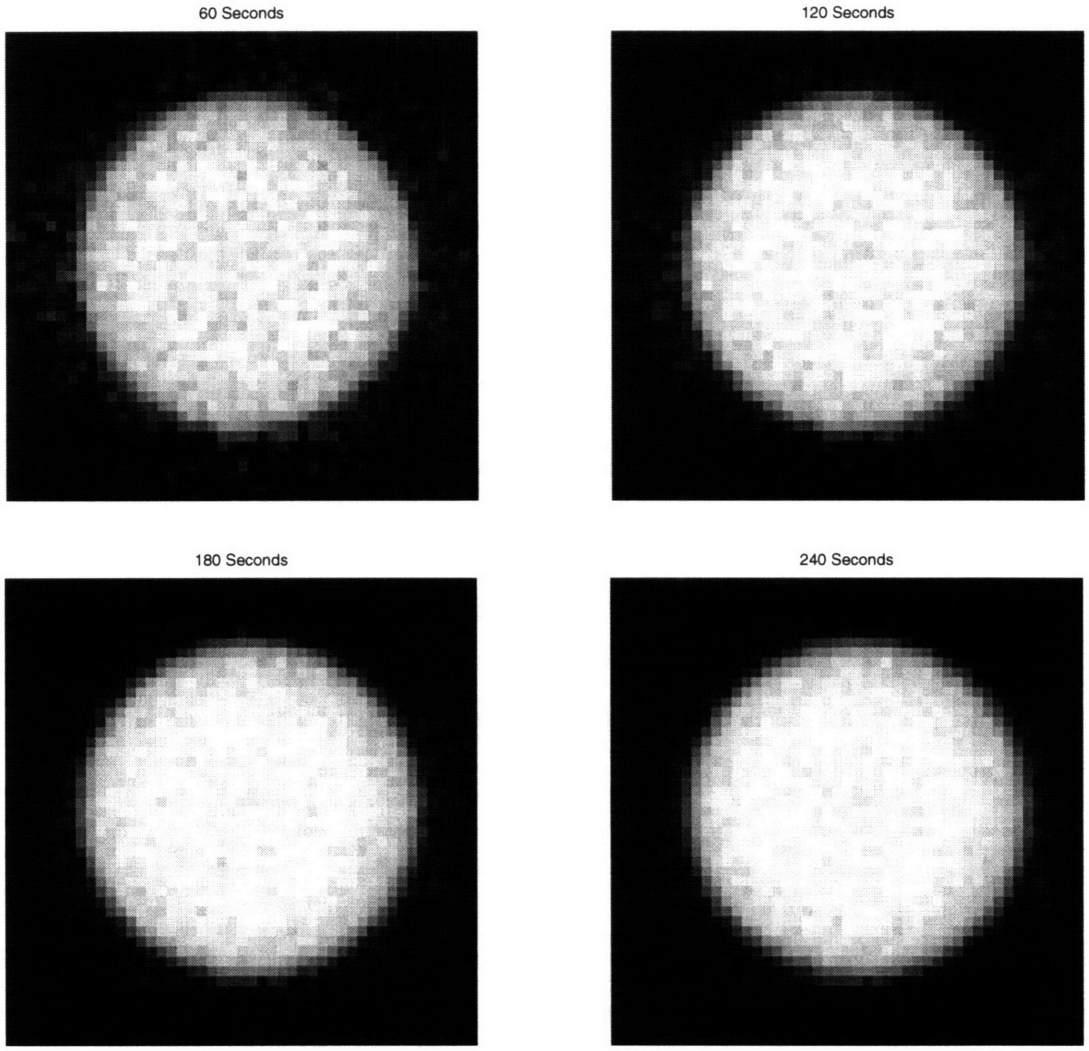

Figure 5-15: Effect of Changing Count Time on Reconstructed Image of Aluminum Cylinder. Parameters: 47 transverse steps, 1.9 mm transverse step size, 72 view angles, first order ramp filter, 0.9 cutoff frequency, count time as indicated.

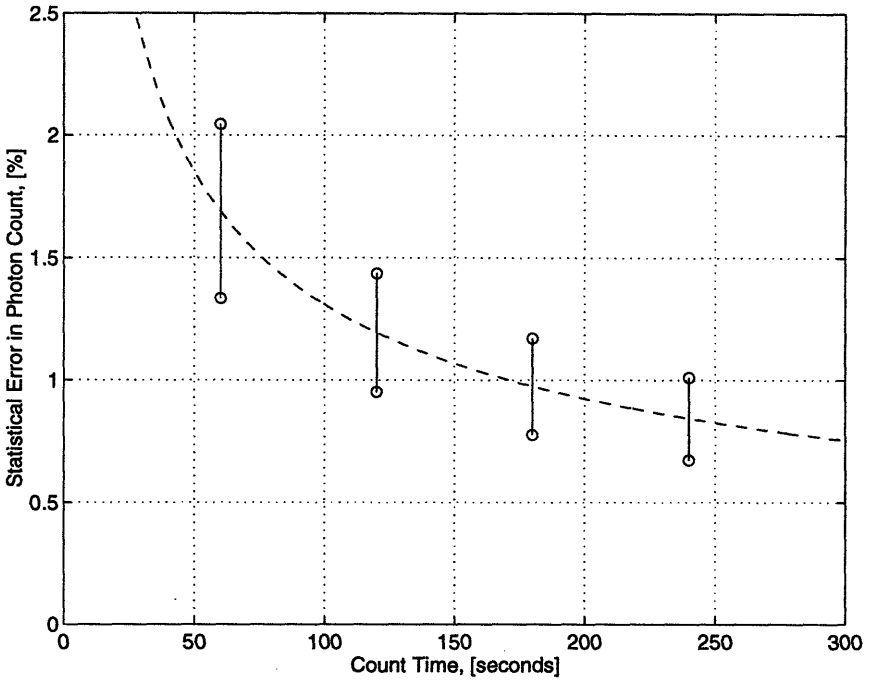

Figure 5-16: Statistical Error in Photon Count for Various Count Times for the Aluminum Cylinder

The results of the CT experiment performed on the aluminum cylinder show the experimental system to be operating properly. The size of the cylinder in the image accurately matches the dimensions of the real object. No discernible artifacts appear in the image. The noise within the image is a function primarily of count time. Future experiments will require adequate count time to reduce the uncertainty in the photon count, and thus the image noise.

5.5 Image Reconstruction of Tin Cylinder in Steel Annulus

The third experiment involved a CT reconstruction on an uniform, solid tin cone surrounded by a uniform, solid steel annulus. The detailed construction of this test object is shown in Appendix D. The test object was created by boring out a tapered cavity in a steel cylinder, filling the cavity with molten tin, and allowing the tin to solidify. A cross-section through the object, perpendicular to the axis of the cylinder, reveals a tin circle surrounded by a steel ring. Differenct cross-sections through the cylinder revealed a tin/steel interface of different diameters.

This test object is an ideal mock-up of a solidifying casting. The density difference between solid tin and solid steel is approximately 6% to 7%; the same as the density difference between liquid and solid steel. The geometry of the test object represents the solidification front of a steel cylinder as if it were being continuously cast. The tin represents the liquid core of metal in the casting. The geometry of this mock-up, in particular the interface between the tin and steel, does not vary in time, as a real casting might. Consequently, the test object serves as a perfect test of the resolution capabilities of the experimental CT system–the ability to detect a 6% to 7% density difference and resolve a finite interface.

A setup of the experiment is shown in Figure 5-17. The steel annulus had an outside diameter of 64 mm. The CT scans were performed 51 mm from the top of the cylinder. This produced a steel annulus with a tin center 38 mm in diameter. The source-to-object distance was 215 mm. A step size of 1.9 mm was used for the transverse measurements and a step size of 2.5^o was used for the view angles. There were 47 transverse steps and 72 view angles, identical to the parameters of the experiment performed using the uniform aluminum cylinder. The photon count time was 300 seconds. This count time produced a photon count range within the data set of 36471 to 7049. The overall data acquisition time for the entire data set was approximately 12 days.

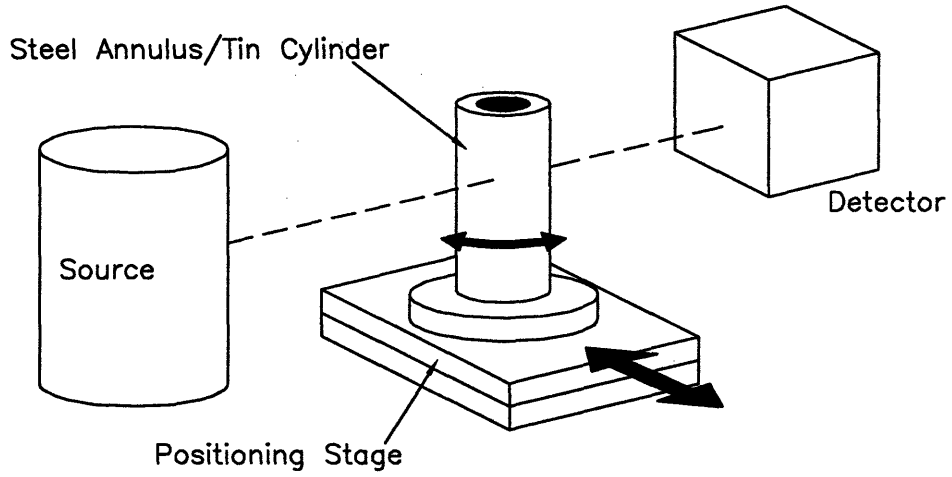

Figure 5-17: Schematic of Setup for Imaging of Steel Annulus and Tin Cylinder

5.5.1 Experimental Results

The reconstructed image of the steel annulus and tin cylinder is shown in Figure 5-18. A contrast difference can be seen between the steel and tin materials, although the interface between the two is blurred. The outside diameter of the steel annulus is roughly 33 to 35 steps. This is equivalent to the experiment conducted on the aluminum cylinder with the same outside diameter. The step size translates to an outside diameter size of 64.8±1.9 mm. This compares very well with the actual cylinder outside diameter of 64 mm. The inside diameter of the steel annulus is more difficult to estimate because of the blurring in contrast between the steel and the tin, as well as the relatively low spatial resolution. The inside diameter was estimated to be 18 to 20 steps. This translates to a inside diameter size of 36.2±1.9 mm. The actual size of the outside diameter is 38 mm. Even though the interface between the steel and tin is blurry, the image still provides a good representation of the actual geometry of the system, given the spatial resolution.

In this experiment, the contrast difference between the steel and tin was the critical parameter. The density difference between steel and tin is approximately 6% to 7%, representative of the density difference between the two phases of steel during solidification. As seen from Figure 5-18, the difference between the two materials could be identified, and the interface found with a reasonable degree of accuracy. Because the contrast resolution is

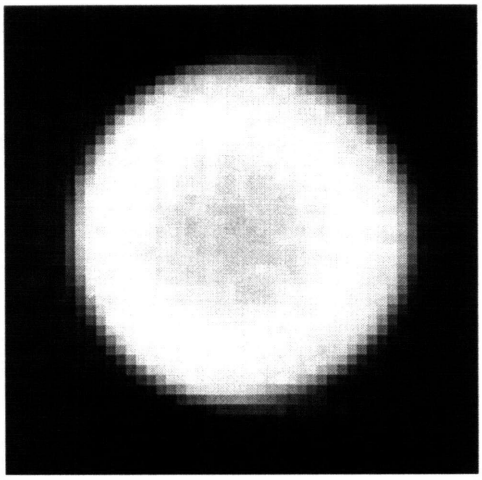

Figure 5-18: Reconstructed Image of Tin Cylinder in Steel Annulus. Parameters: 300 second count time, 47 transverse steps, 1.9 mm transverse step size, 72 view angles, first order ramp filter, 0.9 cutoff frequency

such a critical factor in properly distinguishing between materials of different density, several more experiments were conducted to examine how it is affected by parameter changes. The first two of these experiments related image quality to sample size and count time, two effects examined in previous sections. The last of these experiments involved changing image reconstruction and display parameters by varying the reconstruction filter. The evaluation of the final image quality is often quite subjective, and must be judged in terms of the needs of a particular CT system.

5.5.2 Sampling Size Effects

As discussed previously, the FBP algorithm requires that the ratio of view angles to transverse steps be at least 1.57. However, the previous experimental results have shown that lower ratios also produce adequate image quality while reducing the overall data acquisition time. The data set of the steel annulus and tin cylinder with a 72 view angle sampling was manipulated to produce data sets with fewer view angles. The number of transverse steps was maintained at 47. Five different undersampled data sets were produced, having 9, 12, 18, 24, and 36 view angles. These represented a view angle step size of 20^o, 15^o, 10^o, 7.5^o,

and 5^o, respectively. None of the altered data sets satisfied the criterion of Equation 3.17. In addition, none of the altered data sets had a view angle to transverse step ratio larger than 1. The five undersampled data images are shown in Figure 5-19 along with the original image having 72 view angles.

As seen in Figure 5-19, the contrast resolution is very low and the noise is very high for images with less than 36 view angles. At 36 view angles, the structure of the interface between the steel and tin begins to take shape. However, there is still a fair degree of noise in the image. It is not until 72 view angles that the noise is decreased sufficiently for good image quality. Undersampling at a view angle to transverse step ratio below 1 yields very poor results, with high noise and poor contrast resolution.

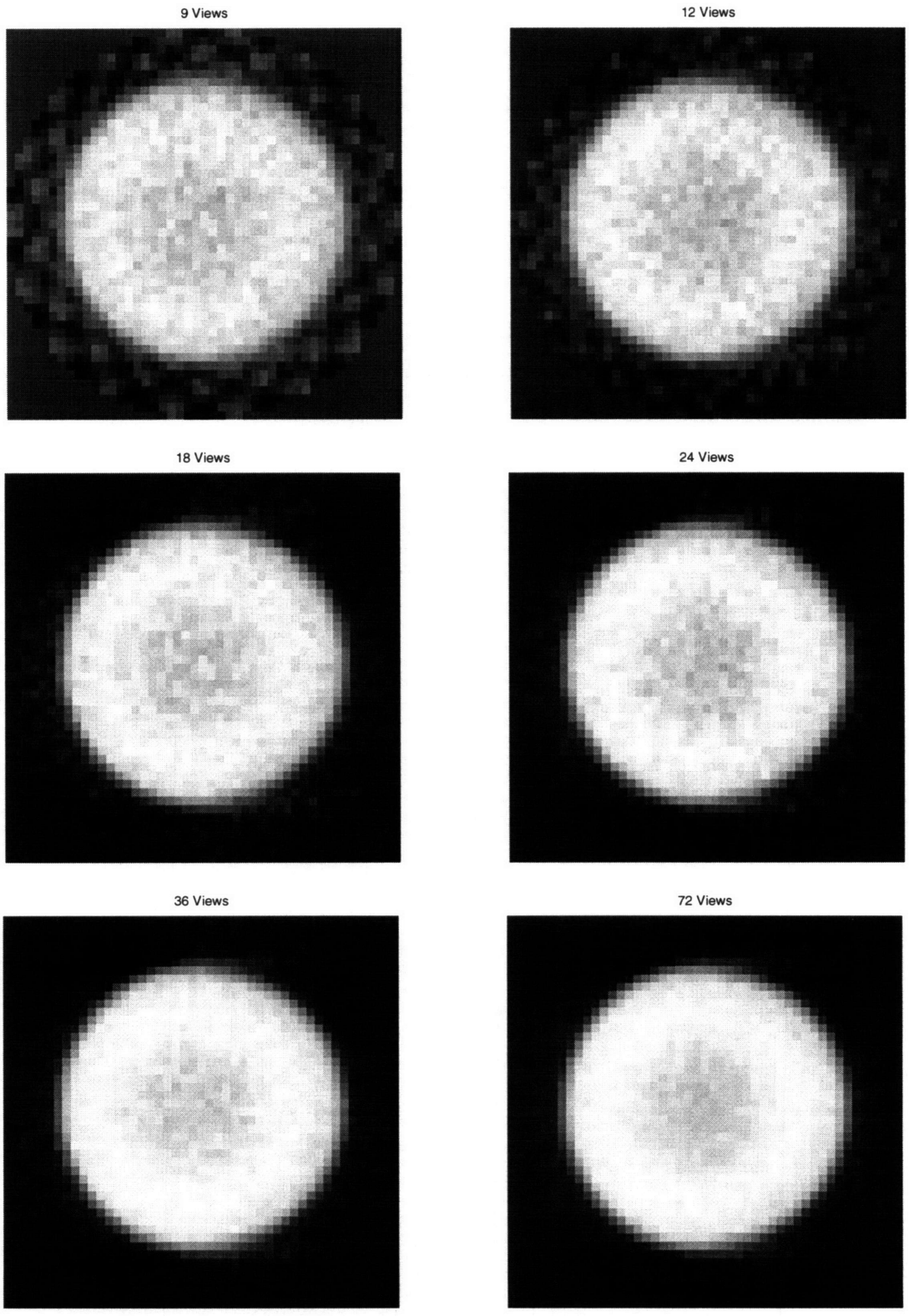

Figure 5-19: Effect of Changing Number of View Angles on Reconstructed Image of Tin Cylinder in Steel Annulus. Parameters: 300 second count time, 47 transverse steps, 1.9 mm transverse step size, first order ramp filter, 0.9 cutoff frequency, number of view angles as indicated.

5.5.3 Sampling Time Effects

To examine the effects of count time on image quality, with particular respect to contrast resolution, four additional experiments were conducted with the steel annulus and tin cylinder. Each of the four experiments was identical to the original experiment described previously, with the exception of count time. The count time per measurement was 60, 120, 180, and 240 seconds for the first, second, third, and fourth experiment, respectively. For the first experiment, the photon count within the data set varied from 7435 to 1413. For the second experiment, it varied from 14690 to 2887. For the third experiment, it varied from 21936 to 4230. For the fourth experiment, it varied from 29110 to 5547. Each of these data sets was reconstructed. Figure 5-20 shows the images of the steel annulus and tin cylinder, along with the previous reconstruction (which had a count time of 300 seconds per measurement).

As is evident from the five images, the noise decreases as the count time increases. This is particularly apparent when comparing the 60 second count image to the 300 second count image. However, the decrease in noise is not very dramatic from image to image, especially from the 240 second count image to the 300 second count image. Using Equation 5.7, the error distribution of the photon count for the different count times was plotted in Figure 5-21. In it, the decrease in photon count error is large between the 60 second count time and the 120 second count time. This translates to a noticeable decrease in noise in the matching images. For each subsequent count time, the decrease in noise is less and less. This diminishing return causes a less and less discernible decrease in image noise. As a result, the images for the 180, 240 and 300 second count time all look relatively similar. Overall data acquisition time can be dramatically decreased by properly choosing a count time which produces an image of adequate quality without excessive sampling.

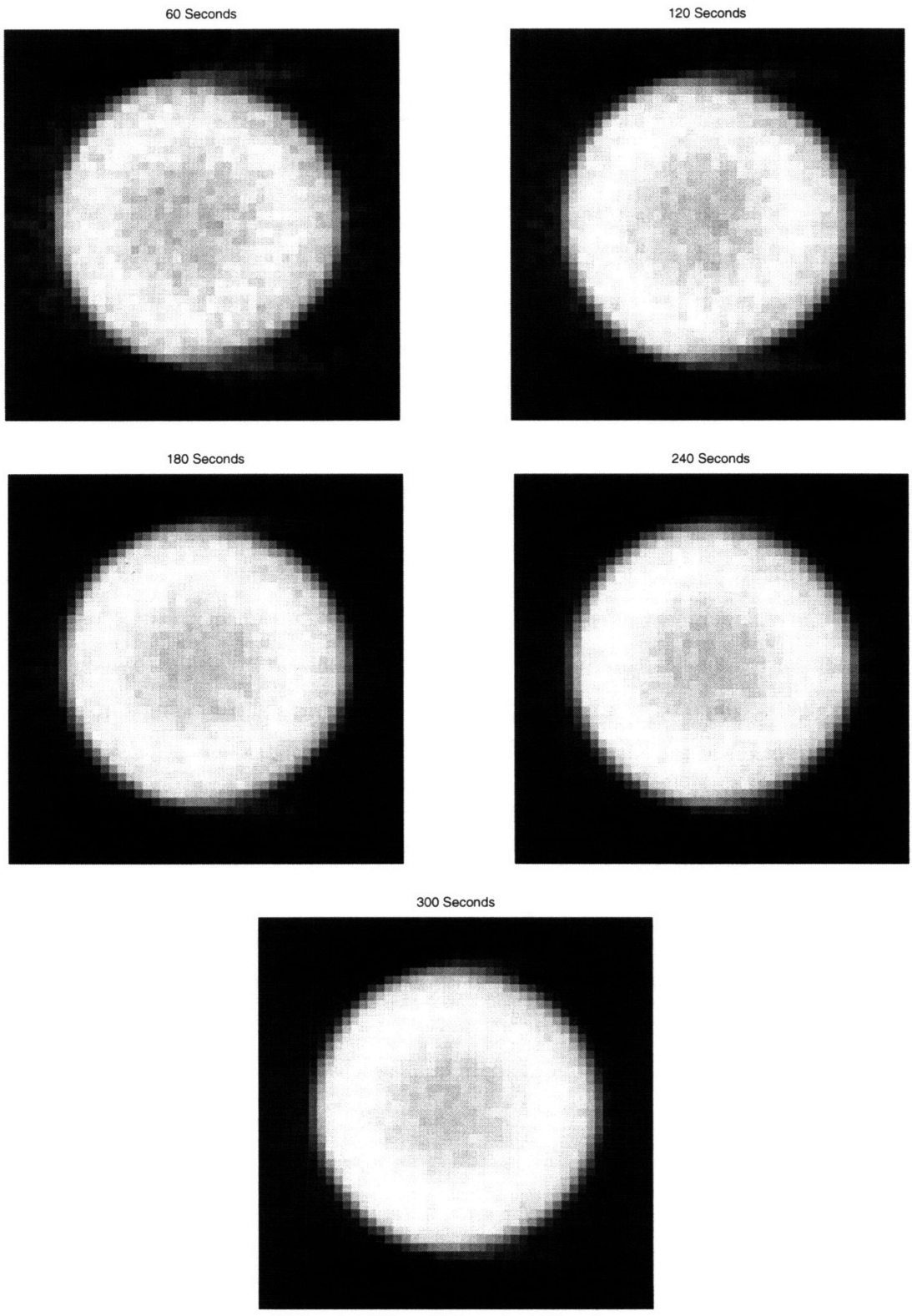

Figure 5-20: Effect of Changing Count Time on Reconstructed Image of Tin Cylinder in Steel Annulus. Parameters: 47 transverse steps, 1.9 mm transverse step size, 72 view angles, first order ramp filter, 0.9 cutoff frequency, count time as indicated.

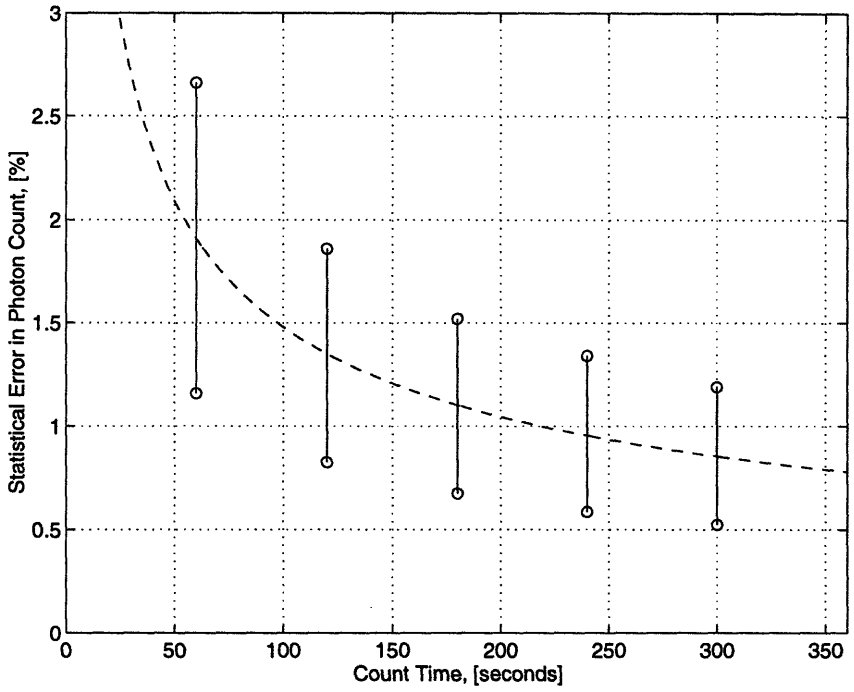

Figure 5-21: Statistical Error in Photon Count for Various Count Times for the Tin Cylinder in Steel Annulus

5.5.4 Image Filter Effects

All of the CT images have been thus far reconstructed using the FBP algorithm with a first order ramp filter and 0.9 cutoff frequency. This choice of filter and cutoff frequency produces the sharpest image quality. However, because it is a high-pass filter, image noise is amplified. There are other combinations of filters and cutoff frequencies which can be applied during the FBP reconstruction to produce dramatically different image results. Three of those filters, ramp, hamming, and Parzen, are examined in this section.

Figure B-2 shows the response characteristics of various filters available for use with the FBP algorithm. The ramp filter's high pass characteristic tend to produce very sharp edges at the expense of noise amplification. The Parzen filter attenuates noise, but has a blurring effect on the image, reducing spatial resolution. The hamming filter is a compromise between the ramp and the Parzen filters.

The original CT data set of the steel annulus and tin cylinder was used to show the effects of different filter and cutoff frequency choices. Figure 5-22 shows results of using a

first order ramp, hamming and Parzen filter with cutoff frequencies of 0.25, 0.5 and 0.75.

The filter effects which are to be expected are present in Figure 5-22. The noticeable features are the loss of image sharpness and attenuation of image noise as one moves from a ramp to a hamming to a Parzen filter. At a given cutoff frequency, the edge resolution is very prominent for the ramp filter image, while much edge blurring occurs with a Parzen filter at the same cutoff frequency. A second noticeable feature is the amplification of noise as the cutoff frequency is increased. This is apparent for all three filters. A point of caution when choosing a filter type is the generation of artifacts in the image. One type of artifact effect is seen in the ramp filter image with a 0.25 cutoff frequency, where a set of concentric rings has appeared.

The choice of filter in the FBP reconstruction is entirely at the user's discretion. Usually, the application of the CT system determines the filter. For example, in an application for which merely distinguishing the presence of dissimilar materials is important, a Parzen filter may be the best choice since precise feature identification may not be necessary. However, for an application such as a solidification front monitor, the location of a discrete interface is critical. Thus, a ramp filter may be a more suitable choice. For applications where both contrast and spatial resolution are important, a compromise filter such as a hamming filter should be used. The cutoff frequency can be adjusted to attenuate image noise.

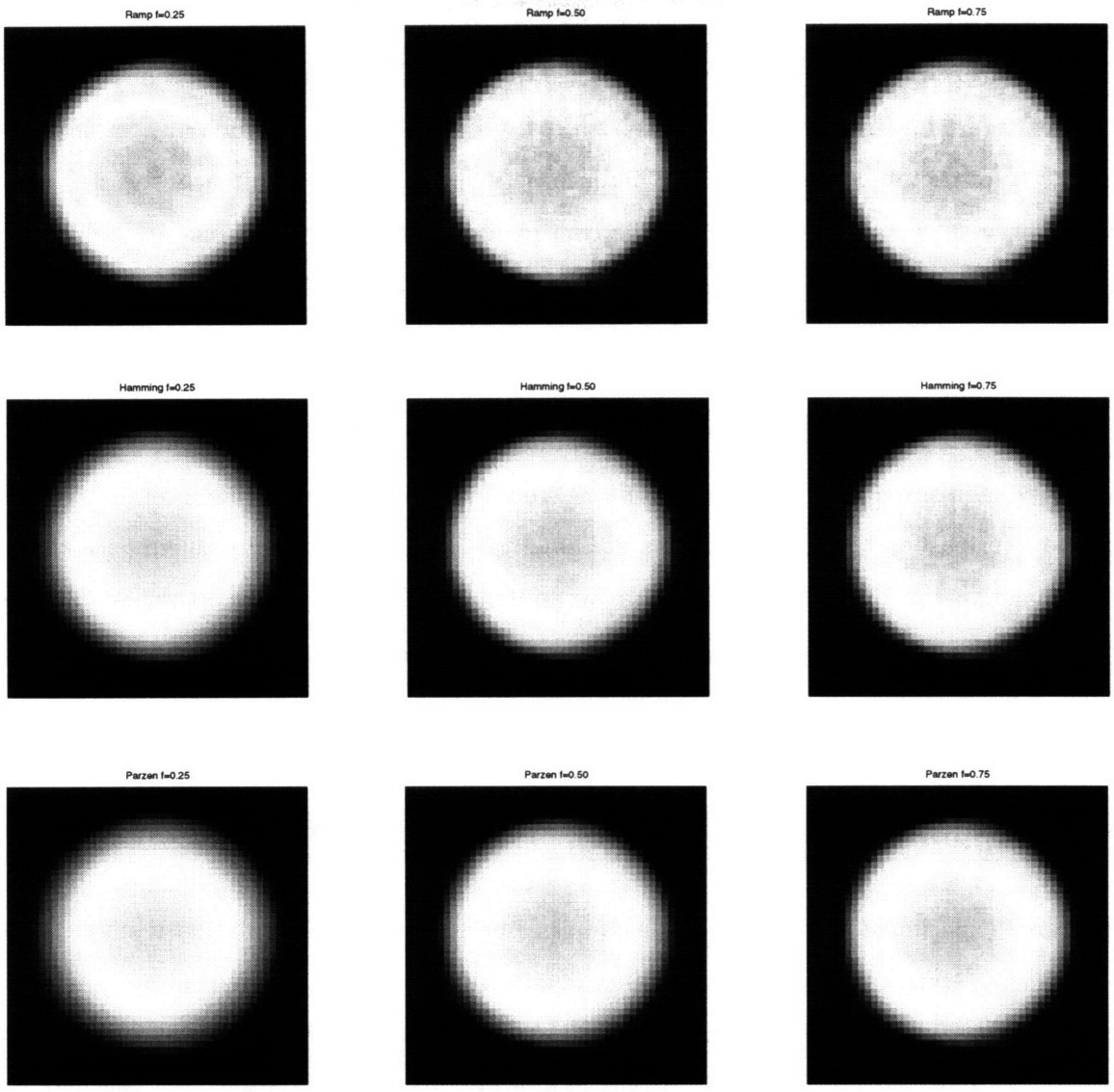

Figure 5-22: Effect of Changing Filter on Reconstructed Image of Tin Cylinder in Steel Annulus. Parameters: 300 second count time, 47 transverse steps, 1.9 mm transverse step size, 72 view angles, first order filter and cutoff frequency as indicated.

The results of the CT experiment on the steel annulus and tin cylinder show that the system can accurately image, with good spatial resolution and contrast resolution, a density difference of 6%. Even though the steel/tin test object did not have molten portions, the geometry of the object and density difference between the steel and tin are well representative of what would be expected in the continuous casting of steel. Consequently, these results confirm the feasibility of using CT to monitor such a process. This experiment again shows the critical dependence on adequate photon count and sampling to produce a viable image. The trade-offs between proper sample size, photon count, and overall data acquisition time are also very evident. As the number of samples and photon counts increases, the data acquisition time becomes quite long, to an almost unmanageable level. This issue must be seriously addressed in future system designs. Finally, the ability to enhance either the image spatial or contrast resolution by applying different filtering operations during reconstruction is seen. The choice of filter is usually application-specific, and there is once again a trade-off between high spatial resolution and high contrast resolution.

5.6 Image Reconstruction of Two-Phase Tin

The final experiment was the reconstruction of pure tin metal in a two-phase state. This experiment served as a test of the feasibility of detecting the solidification front in a partially solidified metal using the principles of CT. The setup of this experiment is shown in Figure 5-23. The pure tin was contained in a graphite crucible. The graphite crucible had an outside diameter of 64 mm and an inside diameter of 51 mm. It was approximately 152 mm long. The tin was melted and poured into the crucible. A 500 W ceramic cartridge heater, enclosed in a copper sheath, was mounted inside the crucible. The sheath was 102 mm long and had an outside diameter of 14 mm. The cartridge heater was used to melt a portion of the tin. Several heater positions were tested, with an offset heater design used for the final experiment. The crucible rested in a recess of a water-cooled aluminum chamber. The water cooled chamber acted as a heat sink, which solidified a portion of the tin inside the crucible. By varying the current to the heater and the water flow rate to the pressure vessel, the amount of liquid tin in the crucible, and thus the position of the solidification front, could be varied. A set of 16 chromel-alumel thermocouples were mounted at a height of 95 mm from the top of the crucible. They were used to monitor the location of the

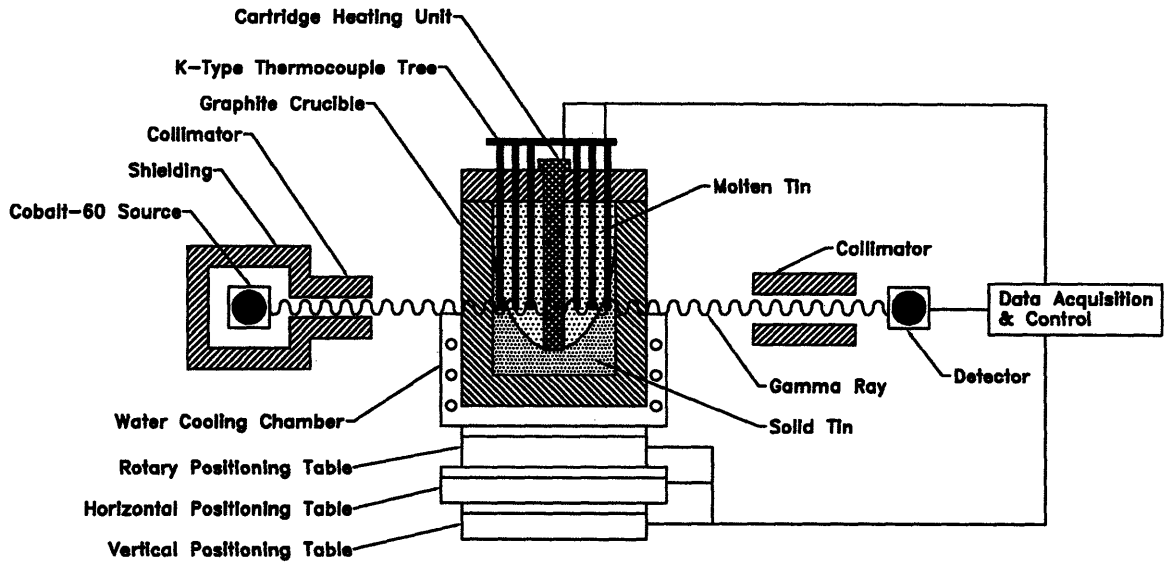

Figure 5-23: Schematic of the Two-Phase Tin Experiment

solidification front.

The CT scans were started when the solidification front of the two-phase tin reached a quasi-steady-state. The source-to-object distance was 215 mm. Projection measurements were taken at a height through the middle of the crucible, in-line with the ends of the thermocouples. A step size of 1.9 mm was used for the transverse measurements and a step size of 3^o was used for the view angles. There were 67 transverse steps and 60 view angles. The ratio of N_θ to N_s was 0.89. This was a less than ideal ratio for proper image reconstruction, but was necessary since the data acquisition time was already extremely long. A photon count time of 300 seconds was used. This count time produced a photon count range within the data set of 25220 to 4629. The photon count error ranged from 0.63% to 1.47%. The overall data acquisition time for the entire data set was approximately 14 days.

5.6.1 Experimental Results

Two reconstructed images of the experiment using two different colormaps are shown in Figures 5-24 and 5-25. These images are the best results from several experiments conducted. Figure 5-24 uses a wider range color bar. In this image, the crucible geometry, the top

portion of the aluminum pressure vessel, and six steel cap screws are very distinguishable. The real position of the six steel screws and the diameter of the aluminum chamber match the image quite well. In addition, the crucible geometry from the image was estimated to be 32 to 33 steps for the outside diameter and 25 to 26 steps for the inside diameter. This is equivalent to an outside diameter size of 61.9±1.0 mm and an inside diameter size of 48.6±1.0 mm, comparing very well to the actual dimensions. However, the image contrast within the interior of the crucible is poor. Figure 5-25 uses an alternate colormap which better identifies structures inside the crucible. In Figure 5-25, the cartridge heater is well defined. A rough outline of the solidification front is also discernible. Figure 5-25 was modified by filtering all structures outside of the crucible to better identify the solidification front. The results are shown in Figure 5-26. In this image, the position of the liquid pool of tin is better defined, but the overall contrast is still rather poor.

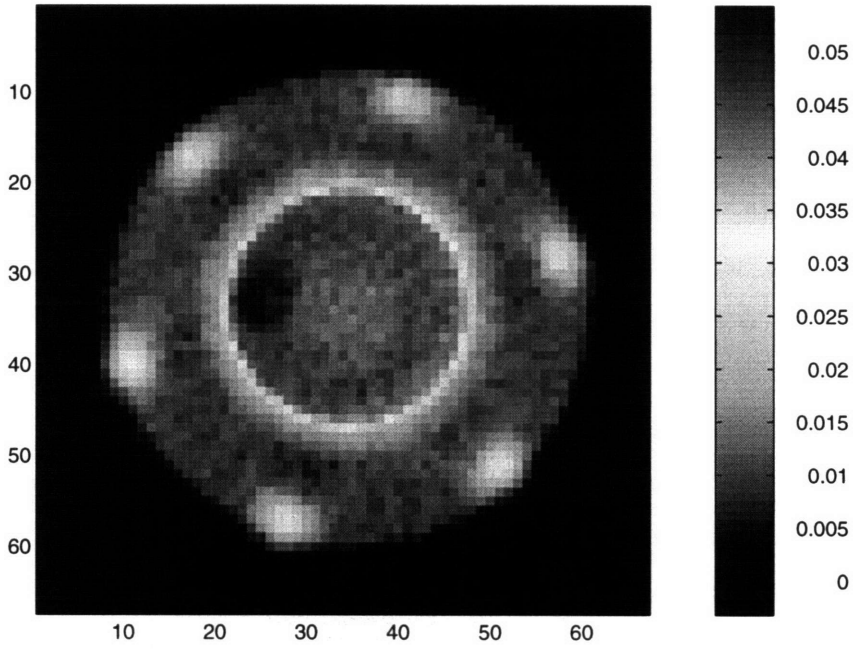

Figure 5-24: Reconstructed Image of Two-Phase Tin Experiment. Parameters: 67 transverse steps, 1.9 mm transverse step size, 60 view angles, first order ramp filter, 0.9 cutoff frequency, 300 second count time, colormap 1

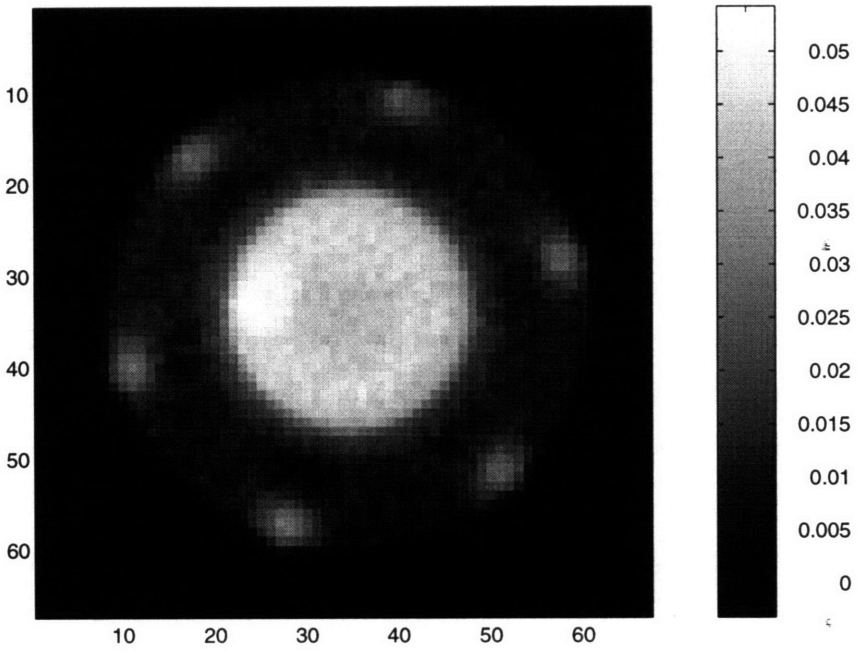

Figure 5-25: Reconstructed Image of Two-Phase Tin Experiment. Parameters: 67 transverse steps, 1.9 mm transverse step size, 60 view angles, first order ramp filter, 0.9 cutoff frequency, 300 second count time, colormap 2

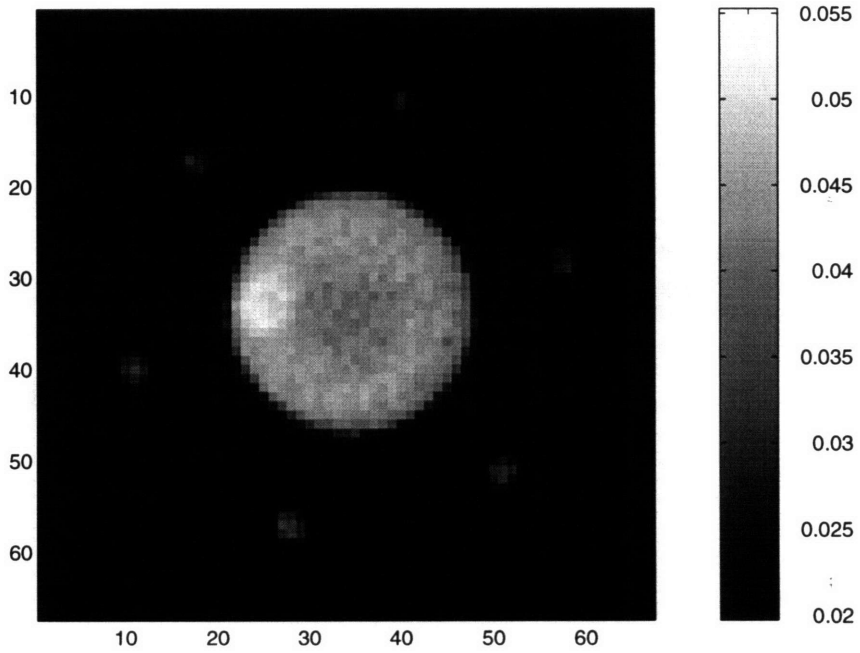

Figure 5-26: Reconstructed Image of Two-Phase Tin Experiment with Extraneous Data Removed

5.6.2 Thermocouple Measurements

During the course of the data acquisition, the 16 thermocouple temperatures were recorded at each photon count measurement. Thermocouple temperature versus time is plotted in Figure 5-27. The data acquisition period for this experiment was 14 days, and as is evident from the data, there was a tremendous amount of temperature fluctuation. This fluctuation significantly altered the location of the solidification front over the course of the experiment. Consequently, the location of the solidification front cannot be measured with any degree of accuracy. However, by taking the average of the thermocouple measurements, some insight on the liquid pool shape was gained. The thermocouple position within the crucible and the average temperature of each thermocouple is shown in Figure 5-28. From these rough measurements, an estimate of the time-averaged position of the solidification front was made.

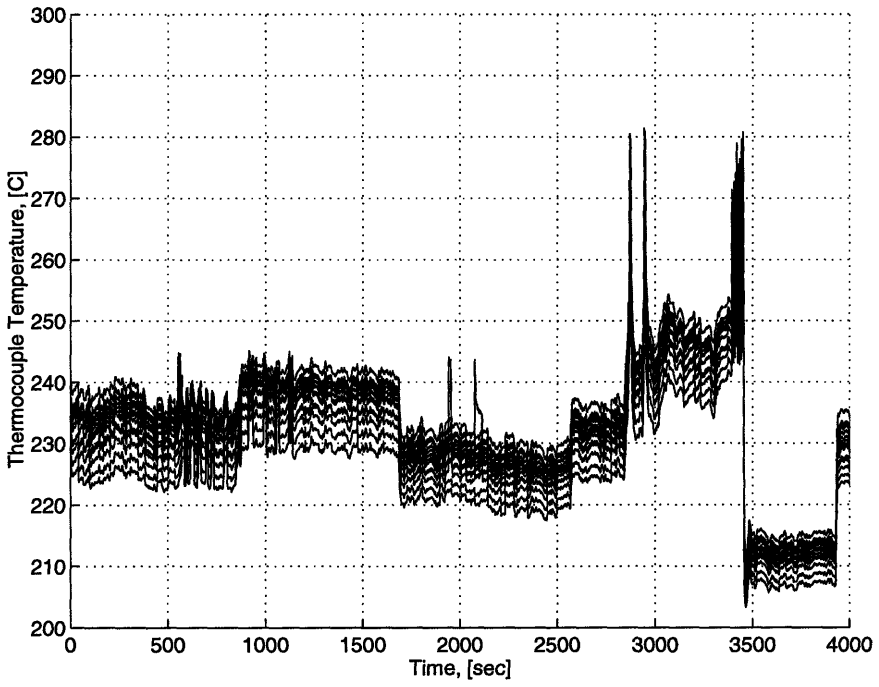

Figure 5-27: Thermocouple Measurements of Tin during Two-Phase Experiment

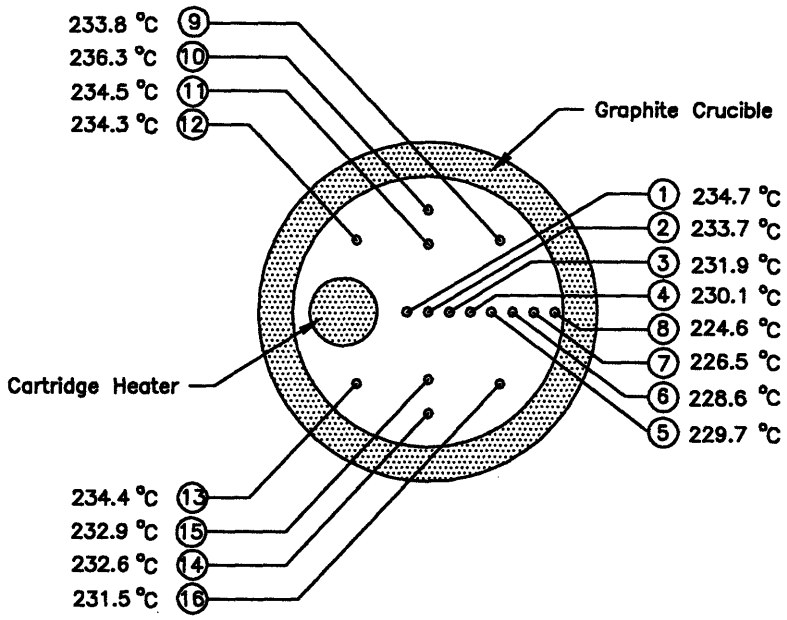

Figure 5-28: Thermocouple Location and Average Temperature within Crucible during the Two-Phase Tin Experiment

Figure 5-29 is an estimate of the liquid tin pool size based on the time-averaged thermocouple measurements. Figure 5-30 is the CT reconstructed image of the two-phase tin experiment. Comparison of the two images reveals a smaller liquid pool size present in the CT image than predicted by the thermocouple measurements. There are many reasons for this weak correlation between the predicated and actual solidification front position.

The largest source of error is the fluctuation in melt temperature over the course of the data acquisition. For reasonable statistical data (1.47% maximum photon count error), a long photon count time was used (300 seconds). Consequently, the data acquisition required 14 days for a 67 transverse step by 60 view angle data set to be completed. This scan time is extremely long by normal CT standards. A constant melt temperature was difficult to maintain, even with a temperature controller. Thus, the temperature within the crucible fluctuated, causing the solidification front position to fluctuate. A time-average of the thermocouple measurements was necessary, giving a very poor predication of the solidification front position. In addition, the CT image also produced a time average of the solidification front position. A second source of error is the poor statistical count. The highest error is through the thickest portion of the object, which also happens to be the area

where the solidification front is located. The last source of error is the undersampled data set. As shown in the previous experiments, an undersampled data set lowers the spatial and contrast resolution of an image. This phenomenon is definitely present in this image since the ratio of view angles to transverse scans was only 0.89. The low ratio had been deemed acceptable for the experiment since a higher ratio would have further lengthened an already long data acquisition time.

This experiment was plagued with many sources of error, but the image of the two-phase tin in Figure 5-30 is the best of several trials performed. Although the position of the solidification front cannot be properly validated using the thermocouple measurements, and the CT reconstruction of the two-phase tin is a time-averaged image, the most important factor is that a contrast difference *is* visible inside the crucible. This contrast is the difference in density between the liquid and solid tin phases. Based on the prior experiments using the aluminum cylinder and steel annulus/tin cylinder, the CT system was found to be performing correctly. Consequently, the contrast difference in the tin is not an artifact. It is, in fact, the time average of the solidification front position over the course of the 14 day data acquisition. Although this position cannot be verified using the thermocouples, it is present, and as shown in the image, detectable using the principles of CT.

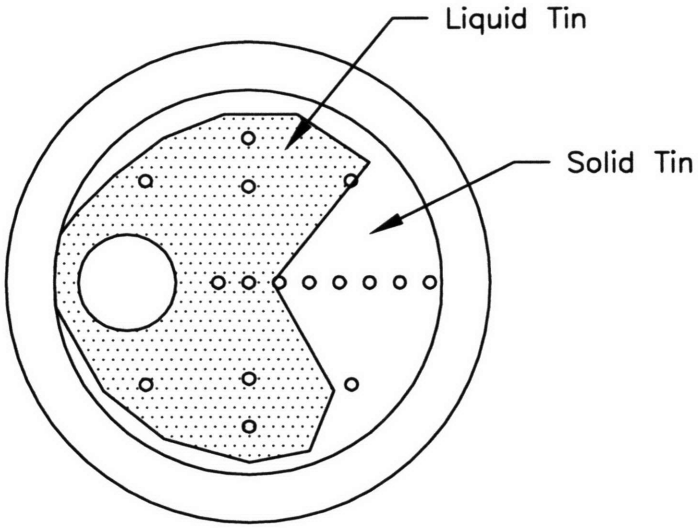

Figure 5-29: Estimated Position of Solidification Front Based on Average Thermocouple Measurements

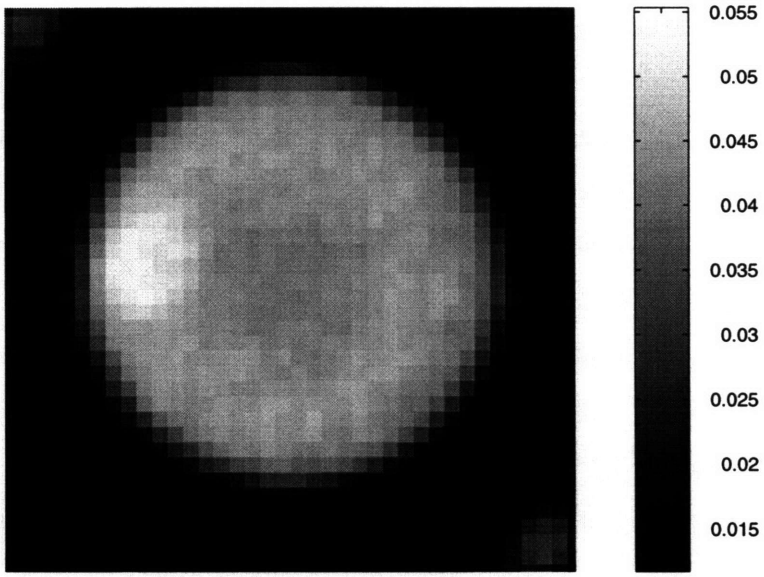

Figure 5-30: Experimental Position of Solidification Front Based on CT Reconstruction. Parameters: First order Hamming filter with 0.9 cutoff frequency

Chapter 6

Conclusions

The findings of this feasibility study are:

- Based on the liquid path length experiment, radiation transmission measurements are a viable method of determining the thickness of liquid or solid sections of a solidifying casting.

- Comparisons of the actual objects with the reconstructed images of the aluminum block, aluminum cylinder, and steel/tin sample show the first-generation experimental CT system to be functioning correctly.

- Based on the reconstructed image of the steel/tin sample, a density difference of 7% was well detected using the experimental CT system.

- Despite a great deal of temperature fluctuation due to the long data acquisition time, the reconstructed image of the solidifying tin sample does show a time averaged position of the solidification front and distinguishes the 4% density difference between the metal's phases.

The principles of CT are well suited to detecting the liquid/solid interface in solidifying metals. The reconstructed CT images of the two-phase tin in the graphite crucible show a liquid pool surrounded by a solid shell. The interface of the solid and liquid portions was not well confirmed by the thermocouple measurements since there was a great deal of temperature fluctuation in the crucible during the data acquisition. Consequently, the CT image gives a time average of the position of the solidification front. Although smaller than predicted, a solidification front *does* exist in the image. It is not an artifact since the previous experiments with the system, identical in setup, using the aluminum cylinder and the steel annulus/tin cylinder, did not show any artifact generation.

The greatest problem encountered during this study was the immensely long data acquisition time for the CT system. This is due to the low photon flux produced by a Co^{60} radioisotope. Obviously, such a system does not have real-time capability. However, the use of a source with a large flux, such as an x-ray linac, will dramatically decrease data acquisition time, possibly to the point of real-time performance. If real-time full data set imaging is not a feasible alternative, attention should focus on the use of limited data set reconstruction to monitor the solidification process. Limited data reconstruction speeds up processing time and when incorporated with any already-known parameters, such as object geometry or material density, may make a viable real-time detection system possible. In any event, the results of this work do show that the different phases of a solidifying metal are detectable using the attenuation principles of high energy photons. Further application of this technology seems quite viable, whether it be by use of CT or some alternate information feedback system.

6.1 Feasibility of a Full-Scale System

The advantages of a sensor to detect and monitor the solidification front in metals are quite evident. Such a sensor would complement and verify current solidification modeling techniques and non-destructive evaluation methods, such as eddy current technology. It would create a tool for process and product design, aiding in the development of future casting machines through better understanding of the fundamental processes in solidification. As real-time processing is implemented, this sensor would allow for closed-loop process control, reducing breakout accidents in continuous castings, as well as improving metal casting quality and production rates.

Although the advantages of such a sensor are widespread, there are still many issues which must be addressed before a real-time CT scanner for continuous casting becomes reality. These issues include system performance, design criteria, and safety.

6.1.1 System Performance

In order for this technology to be beneficial to industry, the sensor must operate at a level at which real-time results are achievable. Due to the large cross-section thickness and high material density of continuous castings, the use of a high-energy radiation source, such as

a linac, is a requirement. A high-energy linac, operating in the 2 MeV to 8 MeV range, should have a photon flux high enough to generate statistically noise-free data in a short period of time. In addition, alternate scanning methods must be implemented to increase the data acquisition speed. These include multiple detectors in a fan-beam, or even a cone-beam, configuration. Finally, limited data set reconstruction algorithms may be required to bring the sensor to a real-time performance level. CT using limited data techniques is a burgeoning area of research; it may well be a feasible technology in the coming years.

6.1.2 System Design Criteria

Appropriate component selection for an industrial CT sensor is highly dependent on the type of performance required from the system. The choice of an appropriate radiation source (here, a linac) determines the amount of photon flux through the object over a given period of time. Consequently, the photon flux determines the spatial and contrast resolution of the system. Performance curves for a full-scale CT sensor design for continuous casting have been developed by Kim [37]. Figure 6-1 shows an example of these performance curves as applied to a steel casting with a 200 mm cross-section. The upper graph relates the required photon flux to achieve a given spatial and density resolution for a single measurement through the casting. The lower curve predicts the required linac parameters (dose rate and energy) for a given photon flux through the casting. Using the information from these curves for a particular casting material and geometry, the proper selection of linac source size and strength can be made for a chosen spatial and density resolution.

For example, to achieve a spatial resolution of 1 mm and a density resolution of 1%, the flux through the steel casting should be approximately 2×10^6 photons. As a result, a 2 MeV linear accelerator should have a dose rate of approximately 45 rad/second to achieve this required photon flux.

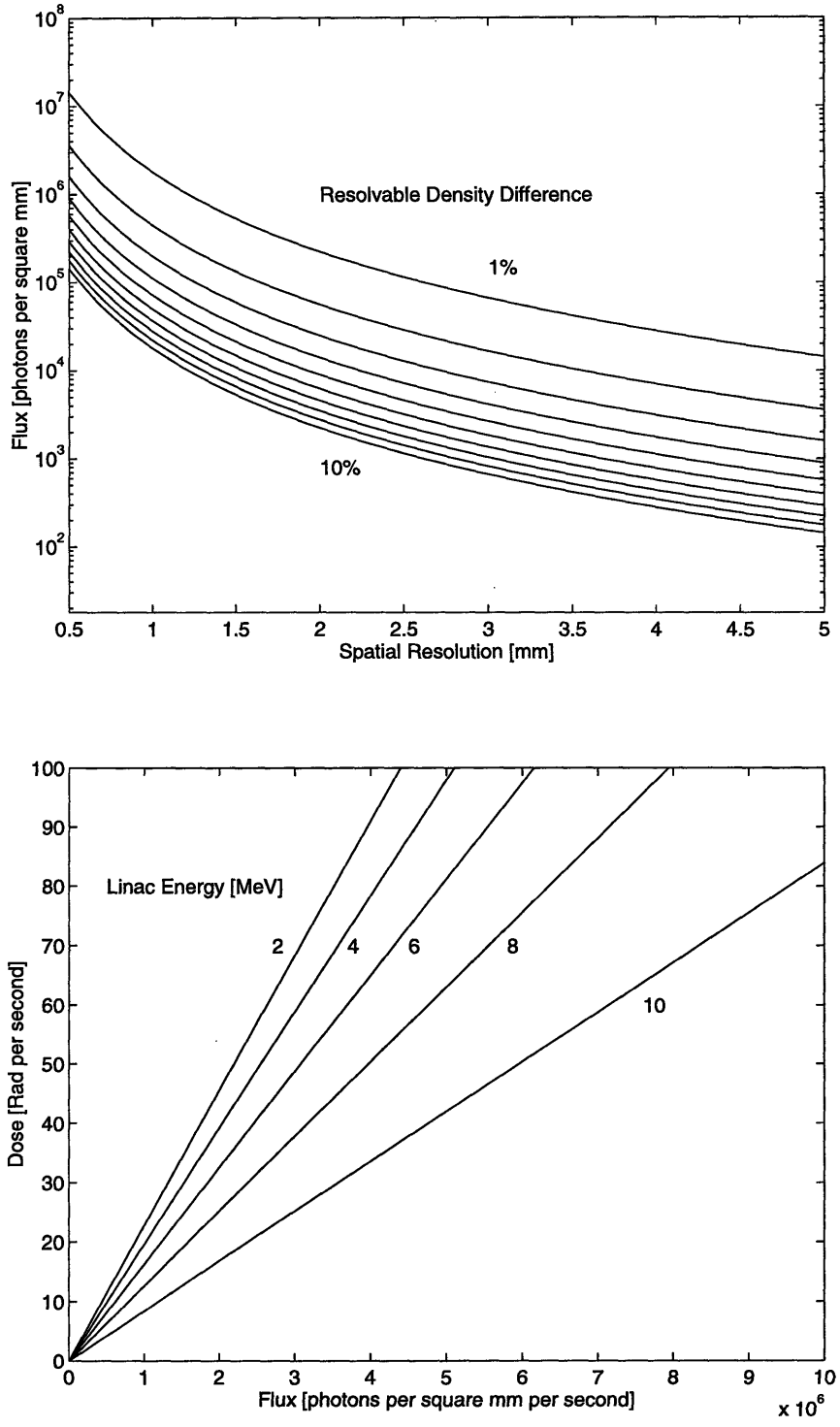

Figure 6-1: Performance Specifications for a CT Solidification Monitor Applied to a Steel Casting with a 200 mm Thickness

6.1.3 Safety Issues

One issue which has not been significantly addressed during this research is that of safety. Because of the low energy and low flux of the Co^{60} radioisotope used during the experiments, radiation safety and shielding was a relatively simple process. However, if this technology is implemented in an industrial environment or factory setting, safety is of critical concern. Since a linac will be used in future efforts, radiation shielding becomes a significant chore. It will require several feet of concrete to properly isolate the sensor from workers. In addition, radiation safety training will be required of workers.

6.2 Future Work

The future research and development of CT technology will involve development of a full-scale detection and imaging system using a high-energy x-ray linac. A high-energy source will enable laboratory testing on near-net-size aluminum and steel castings. A larger controlled solidification platform will be developed for these metals of higher melting points. To take advantage of the capabilities of the linac, a fan beam or cone beam detection system will be implemented. This will dramatically speed up data acquisition time, ideally to a level where real-time performance is feasible. As performance is evaluated, the possibility of using limited data image reconstruction will be examined. Eventually, prototype system testing will be conducted in an industrial continuous casting facility.

References

[1] J. A. Bakken and T. Bergstrom. Heat Transfer Measurements During DC Casting of Aluminum. In R. E. Miller, editor, *Light Metals 1986*, pages 883–889. The Metallurgical Society, 1986.

[2] M. Bhatia. *Wavelet Transform-Based Multi-Resolution Techniques For Tomographic Reconstruction and Detection.* Doctoral project, Massachusetts Institute of Technology, Department of Nuclear Engineering, September 1994.

[3] M. Bobadilla, J. M. Jolivet, J. Y. Lamant, and M. Larrecq. Continuous Casting of Steel: A Close Connection Between Solidification Studies and Industrial Process Development. *Materials Science and Engineering A*, 173:275–285, 1993.

[4] R. Bossi and G. Georgeson. X-Ray Computed Tomography Analysis of Castings. In Euel R. Cutshall, editor, *Light Metals 1992*, pages 901–905. The Minerals, Metals & Materials Society, 1992.

[5] L. E. Brownell. *Radiation Uses in Industry and Science.* United States Atomic Energy Commission, Washington, D.C., 1961.

[6] T. F. Budinger and G. T. Gullberg. Three-Dimensional Reconstruction in Nuclear Medicine Emission Imaging. *IEEE Transactions on Nuclear Science*, NS-21:2–20, June 1974.

[7] T. F. Budinger and G. T. Gullberg. Transverse Section Reconstruction of Gamma-Ray Emitting Radionuclides in Patients. In *Reconstruction Tomography in Diagnostic Radiology and Nuclear Medicine*, pages 315–342. University Park Press, 1977.

[8] P. Burstein. Performance Issues in Computed Tomography Specifications. *Materials Evaluation*, pages 579–593, May 1990.

[9] Continuous Caster Roundup. *Iron and Steelmaker*, pages 16–27, November 1994.

[10] J.M. Caille and G. Salamon, editors. *Computerized Tomography.* Spinger-Verlag, Berlin, 1980.

[11] S. E. Chidiac, J. K. Brimacombe, and I. V. Samarasekera. A New Transient Method for Analysis of Solidification in the Continuous Casting of Metals. *Applied Scientific Research*, 51(3):573–597, October 1993.

[12] Z. H. Cho. General Views on 3-D Image Reconstruction and Computerized Transverse Axial Tomography. *IEEE Transactions on Nuclear Science*, NS-21:44–54, June 1974.

[13] J. Chun, R. C. Lanza, and N. Saka. Solid/Liquid Interface Detection in Continuous Casting Processes by γ-Ray Attenuation. Massachusetts Institute of Technology, Cambridge, MA, US Patent Pending, Serial No. 08/296,342.

[14] J. Chun, R. C. Lanza, N. Saka, and M. Hytros. On-Line Monitoring of the Solidification Front in Metal Casting. *Annals of the CIRP*, 44:181–184, 1995.

[15] G. S. Cole. Inhomogeneities and Their Control Via Solidification. *Metallurgical Transactions*, 2:357–370, February 1971.

[16] D. C. Copley, J. W. Eberhard, and G. A. Mohr. Computed Tomography Part 1: Introduction and Industrial Applications. *Journal of Metals*, pages 14–26, January 1994.

[17] A. J. Dalhuijsen and A. Segal. Comparison of Finite Element Techniques for Solidification Problems. *International Journal for Numerical Methods in Engineering*, 23:1807–1829, 1986.

[18] G. N. Deryabina and A. G. Ripp. Measuring the Ratio of Liquid and Solid Phases in a Continuously Cast Ingot. Zhdanovsk Metallurgical Plant, January 1980.

[19] Q. Z. Diao and H. L. Tsai. Modeling of Solute Redistribution in the Mushy Zone During Solidification of Aluminum-Copper Alloys. *Metallurgical Transactions A*, 24:963–972, April 1993.

[20] J. Dijk, D. Manneveld, and J. M. Rabenberg. In Plant Assessment of Steel Cleanliness in Continuously Cast Slabs and Hot Rolled Coils. *Ironmaking and Steelmaking*, 20(1):75–80, 1993.

[21] D. Ekenhorst, J. Goebbels, and V. Wolf. Applications of Microcomputer Tomography for Optimizing the Manufacture of Fibre Composites. *DKG*, (10):557–560, 1993.

[22] R. D. Evans. *The Atomic Nucleus.* McGraw-Hill, Inc., New York, fourteenth edition, 1972.

[23] K. M. Fisher. The Effects of Fluid Flow on the Solidification of Industrial Casting and Ingots. *PhysicoChemical Hydrodynamics*, 2(4):311–326, 1981.

[24] M. C. Flemings. *Solidification Processing.* Materials Science and Engineering Series. McGraw-Hill, Inc., New York, 1974.

[25] A. F. Giamei. Solidification Process Modeling: Status and Barriers. *Journal of Metals*, pages 51–53, January 1993.

[26] M. E. Glicksman, R. N. Smith, S. P. Marsh, and R. Kuklinski. Mushy Zone Modeling with Microstructural Coarsening Kinetics. *Metallurgical Transactions A*, 23:659–667, February 1992.

[27] M. B. Goldschmit, J. C. Gonzalez, and E. N. Dvorkin. Finite Element Model for Analysing Liquid Slag Development During Continuous Casting of Round Bars. *Ironmaking and Steelmaking*, 20(5):379–385, 1993.

[28] G.W. Grodstein. X-Ray Attenuation Coefficients From 10 KeV to 100 MeV. NBS Circular 583, National Bureau of Standards, United States Department of Commerce, 1971.

[29] R. I. L. Guthrie and H. C. Lee. On-Line Measurements of Inclusions in Steelmaking Operations. *Steelmaking Conference Proceedings*, pages 799–805, 1992.

[30] R. H. Hammerton. *Applied Science in the Casting of Metals*, chapter 4, pages 133–155. Pergamon Press, New York, 1970.

[31] G.T. Herman, editor. *Image Reconstruction From Projections - Implementation and Applications.* Number 32 in Topics In Applied Physics. Springer-Verlag, Berlin, 1979.

[32] S. H. C. Hughes. Nonuniformity of Spatial Resolutions in Computed Tomography Scanners. *Materials Evaluation*, pages 562–565, May 1990.

[33] K. Inoue, T. Koezuka, and H. Arita. Parallel Image Recognition System and Its Application to Steel Making Process. *Proceeding of the Sixth International Iron and Steel Congress*, pages 121–128, 1990.

[34] W. R. Irving. *Continuous Casting of Steel.* The Institute of Materials, London, 1993.

[35] J. L. Jones, Y. D. Harker, W. Y. Yoon, J. M. Hoggan, and G. J. McManus. Pulsed Photonneutron Interrogation: The GNT Demonstration System. Technical report, Idaho National Engineering Laboratory, Idaho Falls, ID, October 1994.

[36] S. Kalpakjian. *Manufacturing Engineering and Technology.* Addision-Wesley, Reading, MA, second edition, 1992.

[37] D. Kim. Master's project, Massachusetts Institute of Technology, Department of Mechanical Engineering, work in progress.

[38] G. F. Knoll. *Radiation Detection and Measurement.* John Wiley & Sons, New York, second edition, 1989.

[39] C. V. Kropas, T. J. Moran, and R. N. Yancey. Effect of Composition on Density Measurement by X-Ray Computed Tomography. *Materials Evaluation*, pages 487–490, April 1991.

[40] R. W. Lewis and P. M. Roberts. Finite Element Simulation of Solidification Problems. *Applied Scientific Research*, 44:61–92, 1987.

[41] B. London, R. N. Yancey, and J. A. Smith. High-Resolution X-Ray Computed Tomography of Composite Materials. *Materials Evaluation*, pages 604–608, May 1990.

[42] W. Loser, S. Thiem, and M. Jurisch. Solidification Modelling of Microstructures in Near-Net-Shape Casting of Steels. *Materials Science and Engineering A*, 173:323–326, 1993.

[43] T. Matsumiya, W. Yamada, T. Ohashi, and O. Nittono. In Situ Observation of Solidification of Silicon Steel by Synchrotron Radiation X-Ray Topography. *Metallurgical Transactions A*, 18:723–727, April 1987.

[44] E. W. McFarland. Non-Destructive Evaluation Using Tomography: Physical Principles and Mathematics. University of California, Santa Barbara.

[45] J. J. Munro, R. E. McNulty, R. Link, R. Grimm, W. Nuding, C. Sauerwein, and H. Wiacker. Mobile Computed Tomography Systems for Industrial Applications. *Materials Evaluation*, pages 568–572, May 1990.

[46] F. Natterer. *The Mathematics of Computerized Tomography.* John Wiley & Sons, New York, 1986.

[47] S. M. Nelko. High Speed Sensor/Probe Revolutionizes Steel Analysis. *Iron and Steelmaking*, pages 33–35, August 1994.

[48] M. W. Nichols, W. C. Bilski, R. D. McGinnis, and J. W. Weyant. Development and Implementation of a Thermocouple Based Breakout Detection System for the Slab Caster at Lukens Steel. In *1992 Steelmaking Conference Proceedings*, pages 789–794, 1992.

[49] A. Notea, U. Feldman, E. Segal, and M. W. Vannier. Imaging Problems Using Medical Computed Tomography for Industrial Applications. *Materials Evaluation*, pages 1066–1072, September 1992.

[50] Office of Technology Assessment. Benefits of Increased Use of Continuous Casting by the U.S. Steel Industry, October 1979.

[51] K. Omura, Y. Otsuka, and M. Konishi. Diagnostic Expert System for Mold Level Control Equipment. *Proceeding of the Sixth International Iron and Steel Congress*, pages 62–68, 1990.

[52] M. R. Ozgu, D. H. Bright, and D. L. Watkins. Experimental and Mathematical Study of Ingot Solidification, Mold Wall Deflection and Ingot-Mold Interfacial Gap Formation. In *Proceedings of the 68th Steelmaking Conference*, pages 315–329, Detroit, April 1985. Iron and Steel Society, Inc.

[53] J. B. Ross and K. McQueeney. Computed Tomography Imaging of Turbine Blades. *Materials Evaluation*, pages 1270–1273, October 1990.

[54] J. Schade, K. D. Ives, and W. A. Brown. Operating Experiences With a Liquid Core Detection System at AK Steel's Ashland Slab Caster. *Iron and Steelmaking*, pages 31–38, September 1994.

[55] D. J. Schneberk, S. G. Azevedo, H. E. Martz, and M. F. Skeate. Sources of Error in Industrial Tomographic Reconstructions. *Materials Evaluation*, pages 609–617, May 1990.

[56] L. A. Shepp and J. A. Stein. Simulated Reconstruction Artifacts in Computerized X-Ray Tomography. In *Reconstruction Tomography in Diagnostic Radiology and Nuclear Medicine*, pages 33–48. University Park Press, 1977.

[57] S. Shi. *An Accelerator-Based Neutron Imaging System and Its Application to Detection of Corrosion in Aircraft.* Doctoral project, Massachusetts Institute of Technology, Department of Nuclear Engineering, May 1995.

[58] E. A. Sivers and M. D. Silver. Performance of X-Ray Computed Tomographic Imaging Systems. *Materials Evaluation*, pages 706–713, June 1990.

[59] C. J. Smithells. *Metals Reference Book*, volume 3. Plenum Press, New York, fourth edition, 1967.

[60] D. L. Snyder and J. R. Cox Jr. An Overview of Reconstructive Tomography and Limitations Imposed by a Finite Number of Projections. In *Reconstruction Tomography in Diagnostic Radiology and Nuclear Medicine*, pages 3–32. University Park Press, 1977.

[61] S. R. Stock, A. Guvenilir, T. M. Breunig, J. H. Kinney, and M. C. Nichols. Computed Tomography Part 3: Volumetric, High-Resolution X-Ray Analysis of Fatigue Crack Closure. *Journal of Metals*, pages 19–23, January 1995.

[62] S. R. Story, R. B. Mahapatra, P. A. Woodberry, R. H. Davies, P. Larkin, and R. Serje. Liquid Core Detection Through Segment Load Measurements. In *1993 Steelmaking Conference Proceedings*, pages 405–413, 1993.

Appendix A

Theoretical Principles of Gamma Radiation Interaction

Over the energy range of 0.01 MeV to 10 MeV, there are three main mechanisms by which gamma radiation interacts with matter. These are the photoelectric effect, Compton scattering, and pair production. These mechanisms are a function of photon energy and incident material, as shown in Figure A-1 [22]. An overview of the three interaction mechanisms is presented in this appendix.

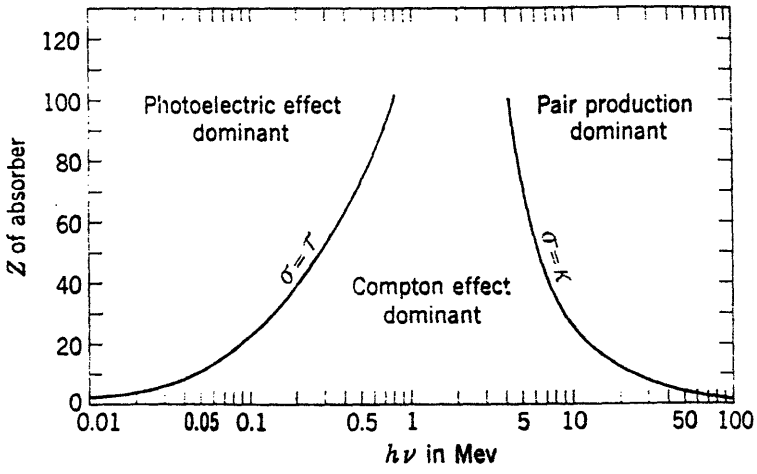

Figure A-1: Graph of relative Gamma-Ray Interaction Mechanisms for Various Energies

A.1 Photoelectric Effect

During the photoelectric effect, a gamma photon is completely absorbed by a bound electron in an atom. A photoelectron, otherwise known as an Auger electron, is ejected from the bound shell during this process, carrying away the majority of the original photon's energy. The shell vacancy which the photoelectron creates is quickly filled by capture of free electrons or by electron shell rearrangement. This generates some low-energy characteristic γ-rays which are often reabsorbed by the atom.

The photoelectric effect is the dominant interaction process for low-energy γ-rays (<0.1 MeV) and is enhanced by materials with high atomic numbers, Z. The probability of photoelectric absorption per atomic cross-section, τ, can be roughly approximated as:

$$\tau \approx const \times \frac{Z^n}{E^{3.5}} \tag{A.1}$$

where the value of the exponent, n, varies from 4 to 5 depending on the γ-ray energy.

A.2 Pair Production

Pair production may occur when the γ-ray energy exceeds 1.02 MeV, twice the rest-mass energy of an electron. The rest-mass energy, E_{rm}, is defined as:

$$E_{rm} = m_o c^2 \tag{A.2}$$

where m_o is the rest-mass of an electron and c is the speed of light. In practice, pair production does not occur with great frequency until the energy exceeds several MeV. Therefore, the interaction process is limited to high-energy γ-rays (>10 MeV). During pair production, the gamma photon is absorbed by the coulomb field of an atom. It is replaced by a electron-positron pair, which has a kinetic energy equal to the energy of the photon minus twice the electron rest-mass energy. As the electron-positron pair loses this energy and slows down, it vanishes via an annihilation process. The probability of pair production per atomic cross-section, κ, is dependent on the energy of the γ-ray photon, and is approximated as:

$$\kappa \approx \frac{Z^2 r_o^2}{137}\left[\frac{28}{9}\ln\left(\frac{2E}{E_{rm}}\right) - \frac{218}{27}\right] \tag{A.3}$$

$$\text{for } E_{rm} \ll E \ll 137 E_{rm} Z^{-\frac{1}{3}}$$

and:

$$\kappa \approx \frac{Z^2 r_o^2}{137}\left[\frac{28}{9}\ln(183 Z^{-\frac{1}{3}}) - \frac{2}{27}\right] \tag{A.4}$$

$$\text{for } E \gg 137 E_{rm} Z^{-\frac{1}{3}}$$

where the classical electron radius, r_o, is equal to 2.818×10^{-13} cm.

A.3 Compton Scattering

The interaction mechanism for γ-ray photons in the energy range of most industrial tomography (1 MeV to 10 MeV) is Compton scattering. During Compton scattering, an incoming gamma photon collides with an electron of an atom, deflecting the photon through an angle θ from its original path. Energy is transferred from the photon to the electron during the collision. Since various scattering angles are possible, the amount of energy transferred can vary significantly. In the limiting case where $\theta = \pi$, the incident photon still retains some of its original energy. The probability of Compton scattering per atomic cross-section, σ, is:

$$\sigma = 2\pi r_o^2\left[\frac{1+\alpha}{\alpha^2}\left(\frac{2+2\alpha}{1+2\alpha} - \frac{1}{\alpha}\ln(1+2\alpha)\right) + \frac{1}{2\alpha}\ln(1+2\alpha) - \frac{1+3\alpha}{(1+2\alpha)^2}\right] \tag{A.5}$$

where α is the photon energy to electron rest-mass energy ratio, defined as:

$$\alpha = \frac{h\nu}{m_o c^2} = \frac{E}{E_{rm}} \tag{A.6}$$

Appendix B

Background on Radon Transform Solution Techniques

B.1 The Radon Transform

In CT, the line integrals of the attenuation measurements over various angles about an object are reconstructed into a single-plane image of the object. A single two-dimensional plane through an object must first be chosen. This image plane has two coordinate systems, as shown in Figure B-1. The first is the object coordinate system (x, y), defined in the plane of the object. The second is the projection coordinate system (s, θ), which describes the line integrals of the attenuation measurement through the object. The origin of both coordinate systems is specified as the center of rotation of the object.

The reconstruction of a two-dimensional image involves transforming the line integral measurements into the object coordinate system. By generalizing the notation of Equation 3.7, the line integral, $g(s, \theta)$, for a particular transverse position, s, and view angle, θ, takes the form [55]:

$$g(s, \theta) = \ln \frac{I_o(s, \theta)}{I(s, \theta)} = \int_L f(x, y) du \tag{B.1}$$

where L is the path over which the line integral is evaluated, and $f(x, y)$ is the distribution of linear attenuation coefficients within the object. The path length, L, can be rewritten in terms of two coordinate systems:

$$x = s \cos \theta - u \sin \theta \tag{B.2}$$

$$y = s\sin\theta + u\cos\theta \tag{B.3}$$

$$s = x\cos\theta + y\sin\theta \tag{B.4}$$

$$u = -x\sin\theta + y\cos\theta \tag{B.5}$$

By appropriate substitution into Equation B.1, the line integral becomes:

$$g(s,\theta) = \int_{-\infty}^{\infty} f(s\cos\theta - u\sin\theta, s\sin\theta + u\cos\theta)du \tag{B.6}$$

Equation B.6 is also known as the Radon transform. The coordinate system (s,θ) is known as the Radon domain. For a fixed view angle, θ, the value of $g(s,\theta)$ is known as a projection. The reconstruction of images from projections is based on the solution of Equation B.6. The distribution of the linear attenuation coefficients, $f(x,y)$, within the object is attained by solving the Radon transform for its inverse. The density through a two-dimensional plane can thus be determined.

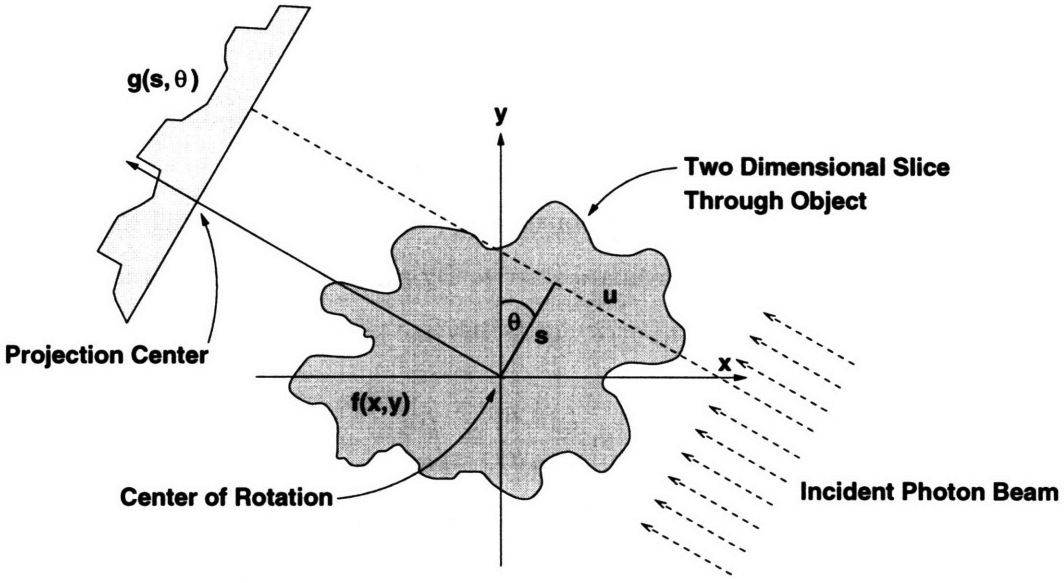

Figure B-1: Layout of Coordinate Systems of Tomographic Imaging System

B.2 Solution Methods

The direct matrix inversion method uses basic linear algebra to find the property distribution in a two-dimensional element. It takes the inverse of the projection matrix to obtain the solution of the property distribution. This technique has major limitations in computation time, the number of mathematical operations, view requirements, and noise suppression. Consequently, alternative methods for solving the inverse Radon transform are usually chosen.

As an improvement on direct matrix inversion methods, ARTs make use of iterative methods to obtain a solution of the projection equations. The ART algorithm involves guessing at values for the property element distribution and modifying the element. The modification is based on a factor which compensates for any difference between the measured value and the estimated value. Several iterations are then performed for appropriate convergence. Modifications can improve the performance of ART, including boundary condition assignment and noise compensation. The SIRT is similar in principle to ART, but offers the advantage of altering the value of the property distribution for a given iteration by using all the projection data simultaneously. Yet another iterative technique is the least-squares iterative technique. It minimizes the error between measured projections and the estimated projections at the n^{th} projection in a least-squares fashion. This algorithm offers the advantage of accommodating noisy data and errors in data accumulation.

Back-projection offers a simple and rapid method of generating a two-dimensional distribution from multiple one-dimensional projections. Each projection is superimposed on film at different display angles corresponding to the scan angle, resulting in a reconstructed image. Although simple, the method does not produce a true reconstruction, even if an infinite number of view angles is used. Each point in the reconstruction is formed by the superposition of a set of straight lines corresponding to each projected ray from the true object. This results in an image that is a convolution of the true distribution of the property function with the reciprocal of the radius from each point.

The FBP method is an improvement on the back-projection technique. The FBP algorithm performs a deconvolution between the projection and the property distribution by multiplying the Fourier transform of the projections by a high-pass filter and then back-projecting the inverse transform of this operation [7].

The FBP is divided into five operations [6]:

- Obtain a series of projections,
- Derive the back-projected image by linear superposition,
- Take the Fourier transform of the two-dimensional image,
- Multiply the Fourier coefficients by the spatial frequency radius (filtering operation), and
- Take the inverse Fourier transform of the result to obtain the true image.

The following three equations summarize calculation of the property distribution by filtered back-projection:

$$f(x,y) = \int_0^{\pi} p_\theta(x\cos\theta + y\sin\theta)d\theta \tag{B.7}$$

where

$$p_\theta(s) = \int_{-\infty}^{\infty} g_\theta(s')q(s-s')ds' \tag{B.8}$$

and

$$q(s) = \int_{-\infty}^{\infty} W(\omega)|\omega|\exp(2\pi j\omega s)d\omega \tag{B.9}$$

where ω is the Fourier frequency variable and $W(\omega)$ is a window function used to satisfy the conditions for Fourier integrals. Equation B.7 is the simple back-projection. Equation B.8 is a filtering operation applied to each projection. Equation B.9 is the inverse Fourier transform of the Fourier frequency variable. The filtered projections are represented by p_θ whereas $q(s)$ is the filtering window in the frequency domain.

Different filtering windows applied during the FBP reconstruction have different effects on the final image. Common choices of filters include ramp, Hann, Hamming, Parzen, and Butterworth. The performance magnitude of these filters is shown in Figure B-2 [7]. By specifying the type, cut-off frequency, and mathematical order of a filtering operation, optimization of the trade-offs between edge detection, noise suppression, and ringing (Gibb's phenomenon) in an image is possible. The cut-off frequency is given as a multiplier on the sampling frequency. With the exception of the Parzen filter, filtering operations enhance image edges by passing high-frequency information. However, noise is prevalent at high frequencies, and as a consequence, most filtering operations increase noise variance as well.

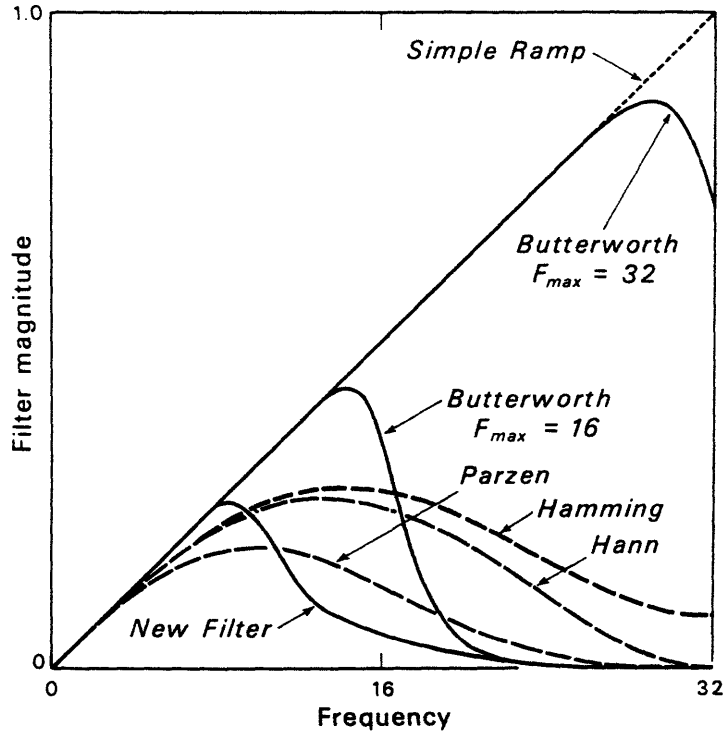

Figure B-2: Example of Response Characteristics of Various Filters

Since the operation affects the number of high-frequency noise components in the reconstructed image, spatial resolution and certain types of artifacts are dependent on the choice of filter. At one end of the spectrum is the ramp filter, best suited for edge detection, but amplifying the most noise. At the other end is the Parzen filter, which suppresses noise but sacrifices spatial resolution. A compromise between the two are the Hann and Hamming filters. The Butterworth filter aids in reduction of ringing in a image in which the object has a high degree of uniformity. As evident by their different characteristics, filtering operations greatly affect the final reconstructed image. A choice must be made with regard to the relevant image parameter before selecting a filter. In this respect, the filter used is entirely subjective, and often, no optimal filter may even exist.

Appendix C

Raw Data for the Gamma Ray Attenuation Experiment

C.1 Numerical Data

This section contains the raw data recorded during the gamma ray attenuation experiments. The first table contains the photon count data for the calibration experiment performed for various tin thicknesses. Five measurements per thickness were recorded. The second and third tables contain the photon count data for the liquid/solid path length experiment. Ten measurements for each solidification front level were recorded.

Trial No.	Free Beam	10 mm	20 mm	30 mm
1	150,441	107,376	78,658	56,831
2	150,696	107,277	79,050	56,079
3	150,859	106,953	79,131	56,654
4	150,441	106,908	79,066	56,715
5	150,460	107,428	78,644	56,214
Mean, I	150,579	107,188	78,910	56,499
Deviation, σ	190	242	238	331

Table C.1: Raw Calibration Data - Photon Count for Various Solid Tin Thicknesses

Trial No.	Exp. No. 1	Exp. No. 2	Exp. No. 3	Exp. No. 4	Exp. No. 5
1	7880	8342	7845	7974	8127
2	7741	8288	7998	7775	7969
3	7781	8264	7784	8022	8154
4	7858	8250	8010	7944	8000
5	7864	8378	7978	7958	8028
6	7784	8426	8010	7901	7949
7	7875	8342	7932	7959	8059
8	7719	8493	7909	7812	7777
9	7866	8440	8123	7936	7947
10	7827	8367	8025	7892	7973
Mean, I	7824.0	8359.0	7961.4	7917.3	7998.3
Deviation, σ	61.4	78.9	97.3	75.2	105.9

Table C.2: Raw Attenuation Data - Photon Count for Various Liquid/Solid Tin Path Lengths (Experiments 1 Through 5)

Trial No.	Exp. No. 6	Exp. No. 7	Exp. No. 8	Exp. No. 9	Exp. No. 10
1	7980	8236	8053	8009	8009
2	8061	8202	7906	7925	7929
3	8119	8080	8087	8004	7904
4	8106	8163	8048	7914	7954
5	8236	8230	8025	8046	8008
6	8266	8012	7920	8128	7948
7	8097	8158	8141	7905	8025
8	8056	8238	8028	8008	7907
9	8128	7989	7836	8034	8011
10	8202	8154	8087	7888	8086
Mean, I	8125.1	8146.2	8013.1	7984.5	7978.1
Deviation, σ	87.7	90.8	95.4	78.4	58.9

Table C.3: Raw Attenuation Data - Photon Count for Various Liquid/Solid Tin Path Lengths (Experiments 6 Through 10)

C.2 Intermediate Calculations

This section contains the spreadsheet calculations used to find the liquid path lengths for both the thermocouple technique and the γ-ray technique. The Xess spreadsheet running on a Sun workstation was used. Figure C-1 shows the intermediate calculations used to find the liquid path lengths based on the thermocouple method. Figure C-2 shows the intermediate calculations used to find the liquid path lengths based on the γ-ray attenuation method.

Melt Temp
232

Trial	TC#1 Length	TC#1 Temp	TC#2 Length	TC#2 Temp	X of	X of HIGH	X of LOW	L liq (in)	L liq HIGH (in)	L liq LOW (in)
1	0	42	0	42				0.000	0.000	0.000
2	0	300	0	300				2.828	2.828	2.828
3	0.688	258.7	0.875	226	0.841	0.857	0.826	1.504	1.527	1.484
4	0.688	253.3	0.875	223.3	0.821	0.837	0.807	1.476	1.499	1.456
5	0.875	247.1	1.063	223.9	0.997	1.018	0.980	1.725	1.754	1.701
6	1.313	232.4	1.563	214.6	1.319	1.335	1.305	2.180	2.203	2.161
7	1.063	232.1	1.313	217.5	1.065	1.085	1.049	1.821	1.849	1.799
8	0.875	234.3	1.063	218.5	0.902	0.920	0.889	1.591	1.616	1.572
9	0.688	258.1	0.875	226.8	0.844	0.861	0.829	1.509	1.533	1.487
10	0.688	257.7	0.875	226.6	0.843	0.860	0.828	1.507	1.531	1.485

	L liq (cm)	L liq HIGH (cm)	L liq LOW (cm)
1	0.000	0.000	0.000
2	7.183	7.183	7.183
3	3.820	3.878	3.769
4	3.748	3.806	3.698
5	4.383	4.456	4.321
6	5.537	5.596	5.489
7	4.625	4.697	4.570
8	4.041	4.105	3.993
9	3.832	3.893	3.778
10	3.827	3.888	3.773

Figure C-1: Spreadsheet Data of Calculations used to Determine Liquid Path Lengths based on Thermocouple Measurements

Solid Density		Mass Attenuation Coefficient		N o'																									
7300		0.004478082		7824																									
Trial	Count, N	Deviation	Standard Error	N HIGH	N Low	ln(N/N o')	ln(N/N o') HIGH	ln(N/N o') LOW	Hi Liq Temp	Low Liq Temp	Avg Liq Temp	Liq Density	Mu*Rho*Delta																
1	7824	61.4	58.2	7882.2	7765.8	0.000000	0.007417	-0.007473	42.000	42.000	42.000	7116.413	0.817																
2	8359	78.9	74.9	8433.9	8284.1	0.066143	0.075058	0.057148	439.000	330.000	384.500	6906.563	1.750																
3	7961.4	97.3	92.3	8053.7	7869.1	0.017409	0.028937	0.005747	321.800	232.000	276.900	6972.490	1.457																
4	7917.3	75.2	71.3	7988.6	7846.0	0.011854	0.020825	0.002803	317.500	232.000	274.750	6973.807	1.451																
5	7998.3	105.9	100.5	8098.8	7897.8	0.022033	0.034516	0.009393	340.300	232.000	286.150	6966.822	1.482																
6	8125.1	87.7	83.2	8208.3	8041.9	0.037762	0.047950	0.027469	371.430	232.000	301.715	6957.286	1.524																
7	8146.2	90.8	86.1	8232.3	8060.1	0.040356	0.050874	0.029725	349.720	232.000	290.860	6963.936	1.495																
8	8013.1	95.4	90.5	8103.6	7922.6	0.023882	0.035113	0.012523	330.000	232.000	281.000	6969.978	1.468																
9	7984.5	78.4	74.4	8058.9	7910.1	0.020306	0.029578	0.010947	321.400	232.000	276.700	6972.612	1.456																
10	7978.1	58.9	55.9	8034.0	7922.2	0.019504	0.026484	0.012476	321.180	232.000	276.590	6972.680	1.456																

Gamma Method	Gamma Method	Gamma Method	TC Method	TC Method	TC Method	Gamma Error	Gamma Error	Gamma Error	TC Error	TC Error	TC Error
L liq (cm)	L liq HIGH (cm)	L liq LOW (cm)	L liq (cm)	L liq HIGH (cm)	L liq LOW (cm)	High (cm)	Low (cm)	Average (cm)	High (cm)	Low (cm)	Aveage (cm)
0.000	0	0	0	0	0	0.000	0.000	0.000	0.000	0.000	0.000
3.780	4.289	3.266	7.183	7.183	7.183	0.509	0.514	0.512	0.000	0.000	0.000
1.195	1.986	0.395	3.82	3.878	3.769	0.791	0.801	0.796	0.058	0.051	0.054
0.817	1.435	0.193	3.748	3.806	3.698	0.618	0.624	0.621	0.058	0.050	0.054
1.487	2.329	0.634	4.383	4.456	4.321	0.842	0.853	0.848	0.073	0.062	0.068
2.477	3.146	1.802	5.537	5.596	5.489	0.668	0.675	0.672	0.059	0.048	0.054
2.700	3.404	1.989	4.625	4.697	4.57	0.704	0.711	0.707	0.072	0.055	0.063
1.627	2.392	0.853	4.041	4.105	3.993	0.765	0.774	0.769	0.064	0.048	0.056
1.395	2.031	0.752	3.832	3.893	3.778	0.637	0.643	0.640	0.061	0.054	0.057
1.340	1.819	0.857	3.827	3.888	3.773	0.479	0.483	0.481	0.061	0.054	0.057

Overall Average		Overall Average	
Gamma Error	0.605	TC Error	0.0464

Figure C-2: Spreadsheet Data of Calculations used to Determine Liquid Path Lengths based on Gamma-Ray Attenuation Measurements

C.3 Systematic Offset Error

A systematic offset error was present in the measurement of the liquid path lengths using the γ-ray attenuation measurements. This error is evident in Figure C-3. This systematic error is attributed to a misalignment of the photon beam with the thermocouple tree. The photon beam was offset below the thermocouple tree, producing a lower than expected measurement of the liquid path lengths. By relating the geometry of the crucible to the liquid path lengths which were found using the thermocouple method and the γ-ray attenuation method, the offset positioning error, x_{offset}, was found to be:

$$x_{offset} = (L_{liq_{TC}} - L_{liq_{\gamma}}) \sin\left(\frac{\pi}{4}\right) \tag{C.1}$$

The final measurements of the liquid path lengths using the γ-ray method were adjusted, taking account of this offset amount.

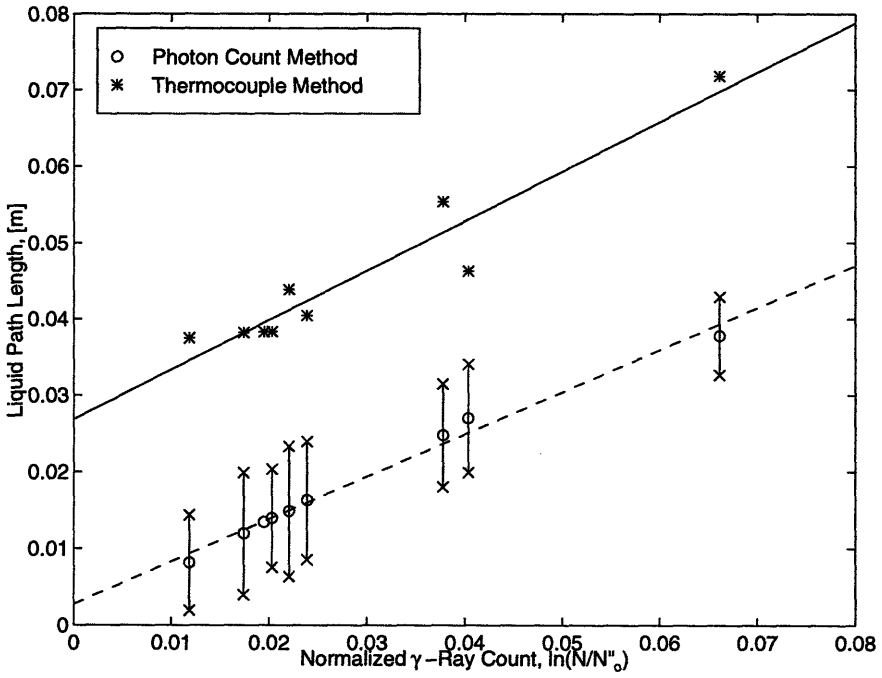

Figure C-3: Comparison of Liquid Path Length Calculations

Appendix D

Design Drawings of Experimental Apparatus Components

The following drawings are detailed descriptions of some of the components used during the various experiments in this project. These include the cooling unit, the melt crucible, and the detector collimator. Although this is not a complete set of drawings for all the parts which were fabricated during the course of this work, it comprises a large portion of them and includes all major items. These drawings were used as templates during fabrication of the experimental platform, and are as complete and current as possible. All drawings were created using AutoCad Version 12.

Figures D-1 and Figure D-2 show the controlled solidification platform and positioning system. Figures D-3 through D-16 are engineering layouts for various components.

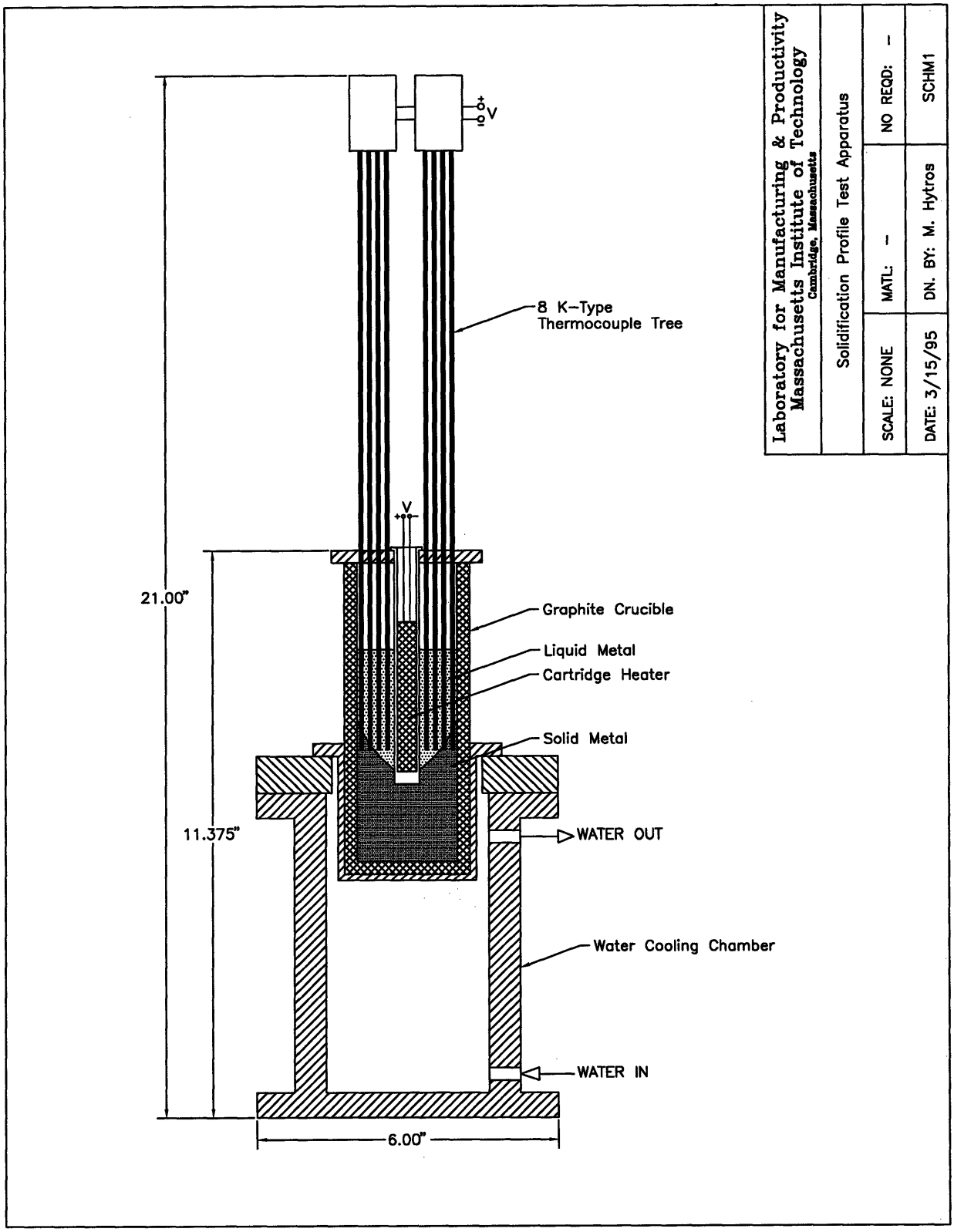

Figure D-1: Detail Drawing of Controlled Heating/Cooling Unit

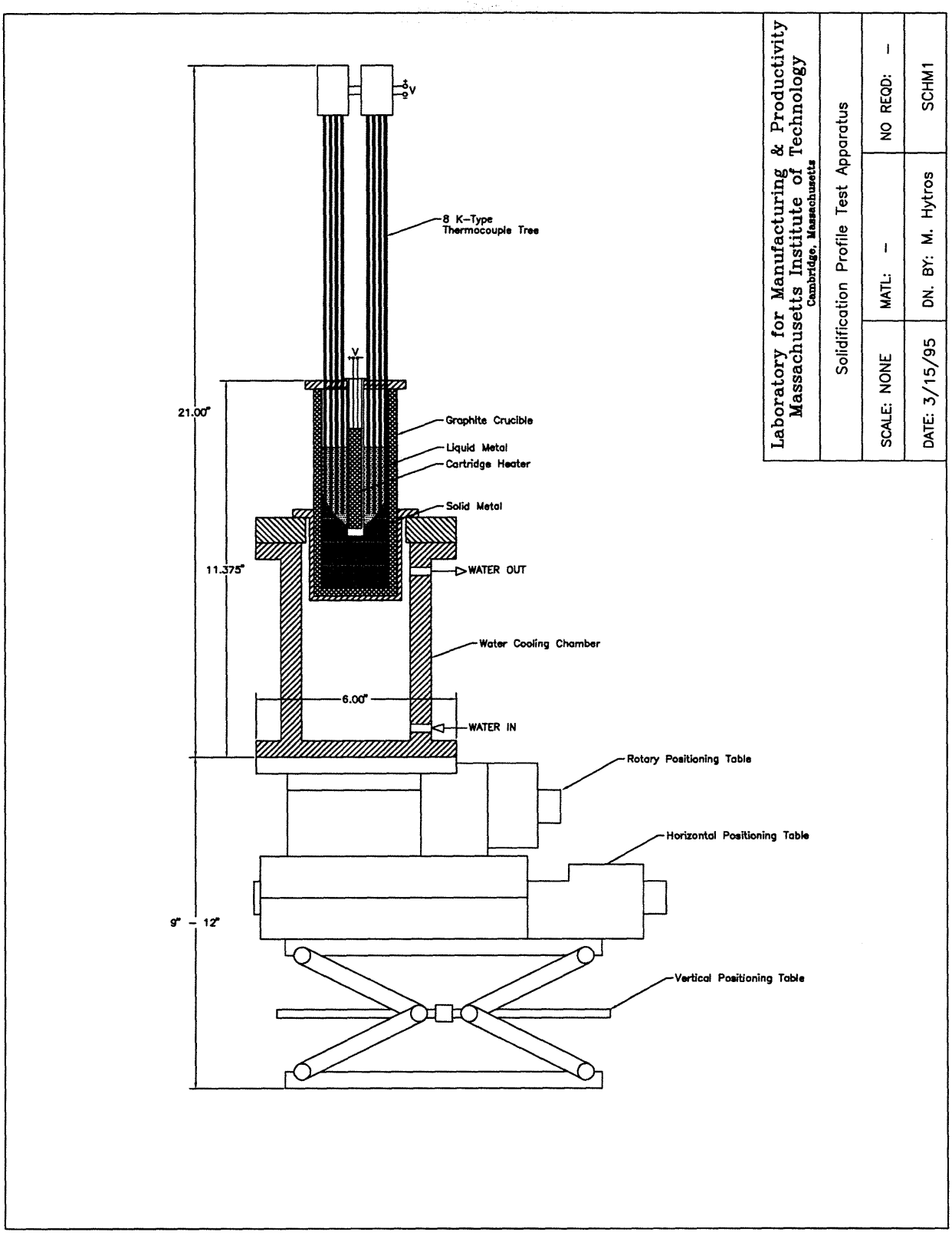

Figure D-2: Detail Drawing of Controlled Heating/Cooling Unit and Positioning System

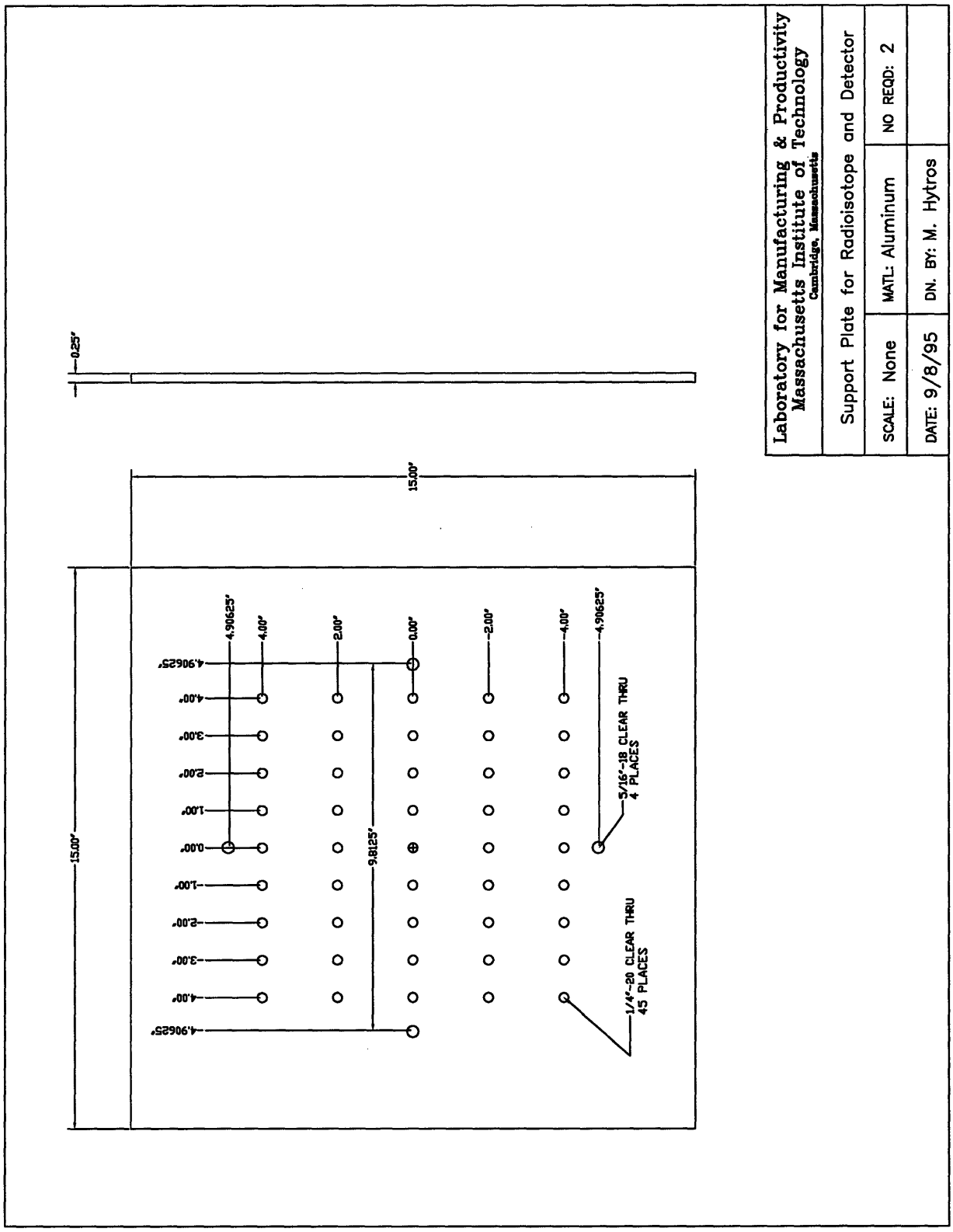

Figure D-3: Detail Drawing of Tomographic Table Mount Plate

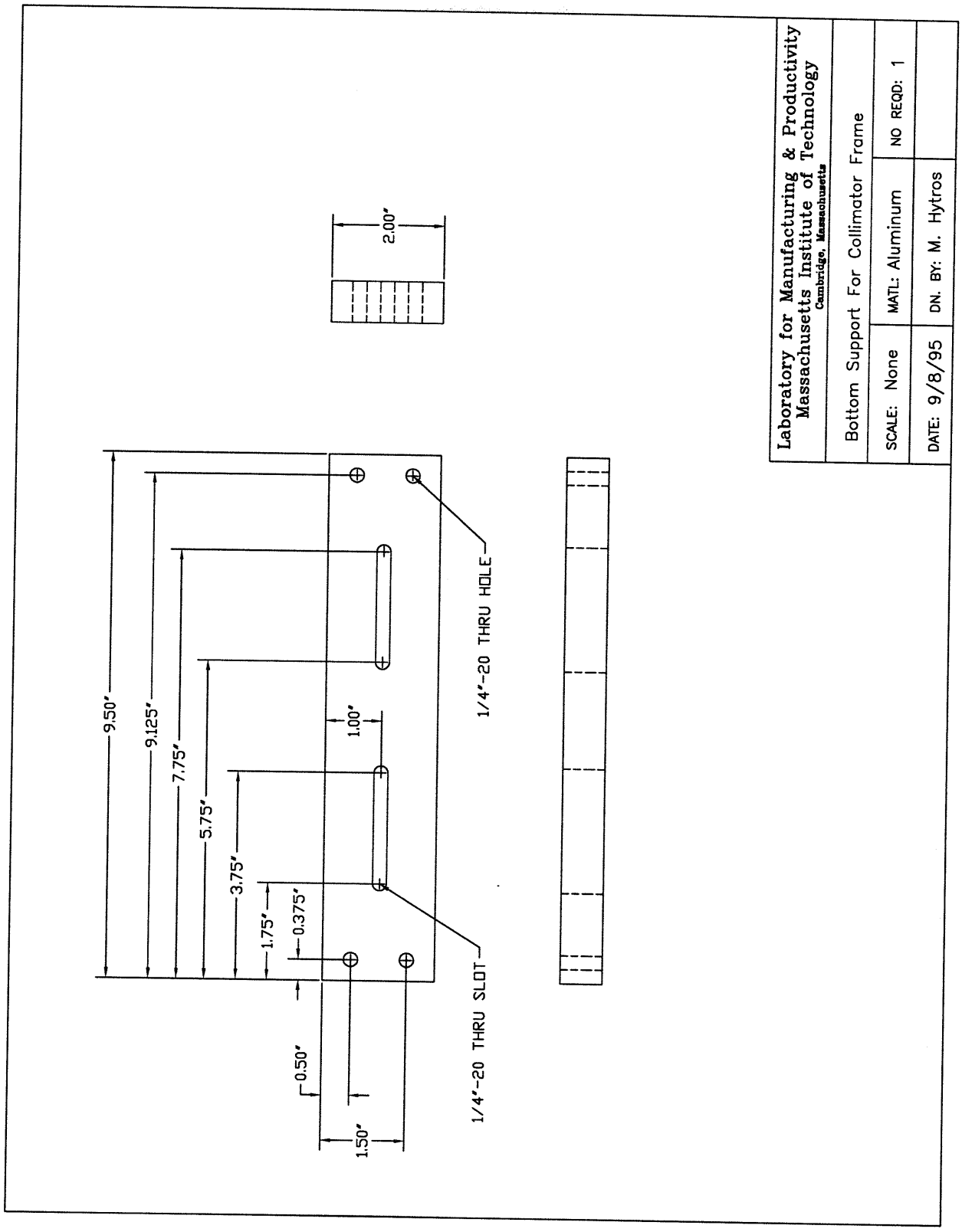

Figure D-4: Detail Drawing of Collimator Base Plate

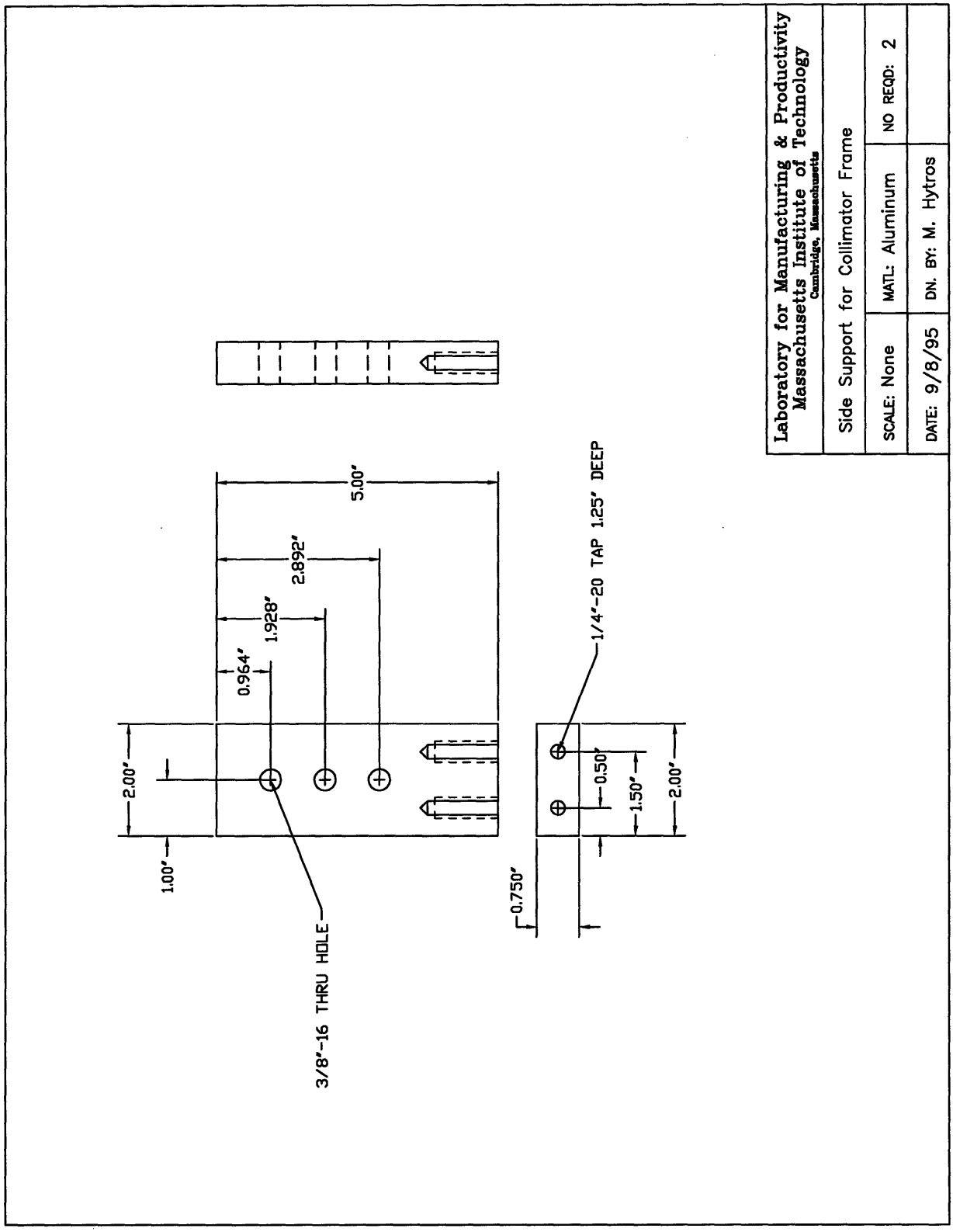

Figure D-5: Detail Drawing of Collimator Side Plate

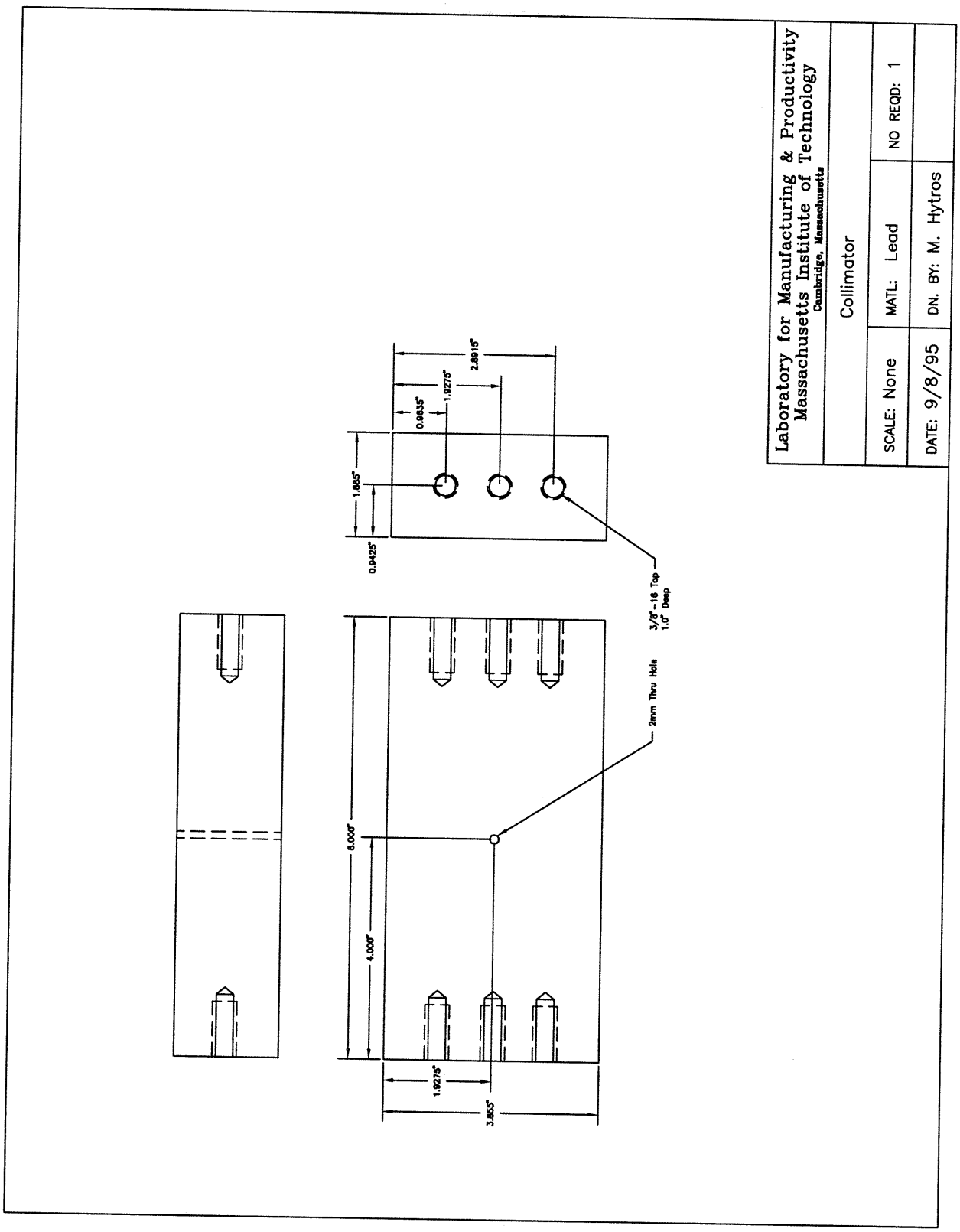

Figure D-6: Detail Drawing of Collimator

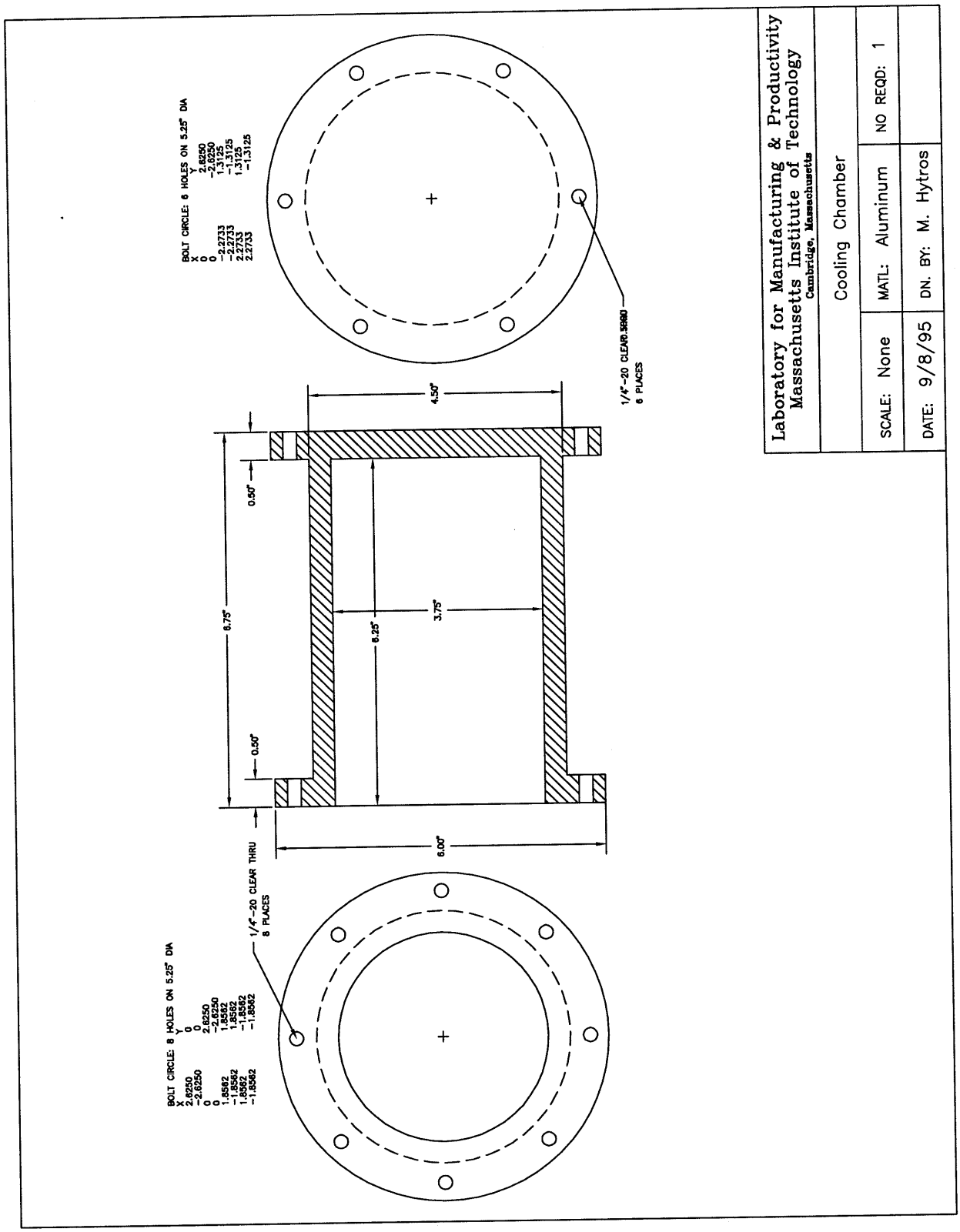

Figure D-7: Detail Drawing of Water Cooling Chamber

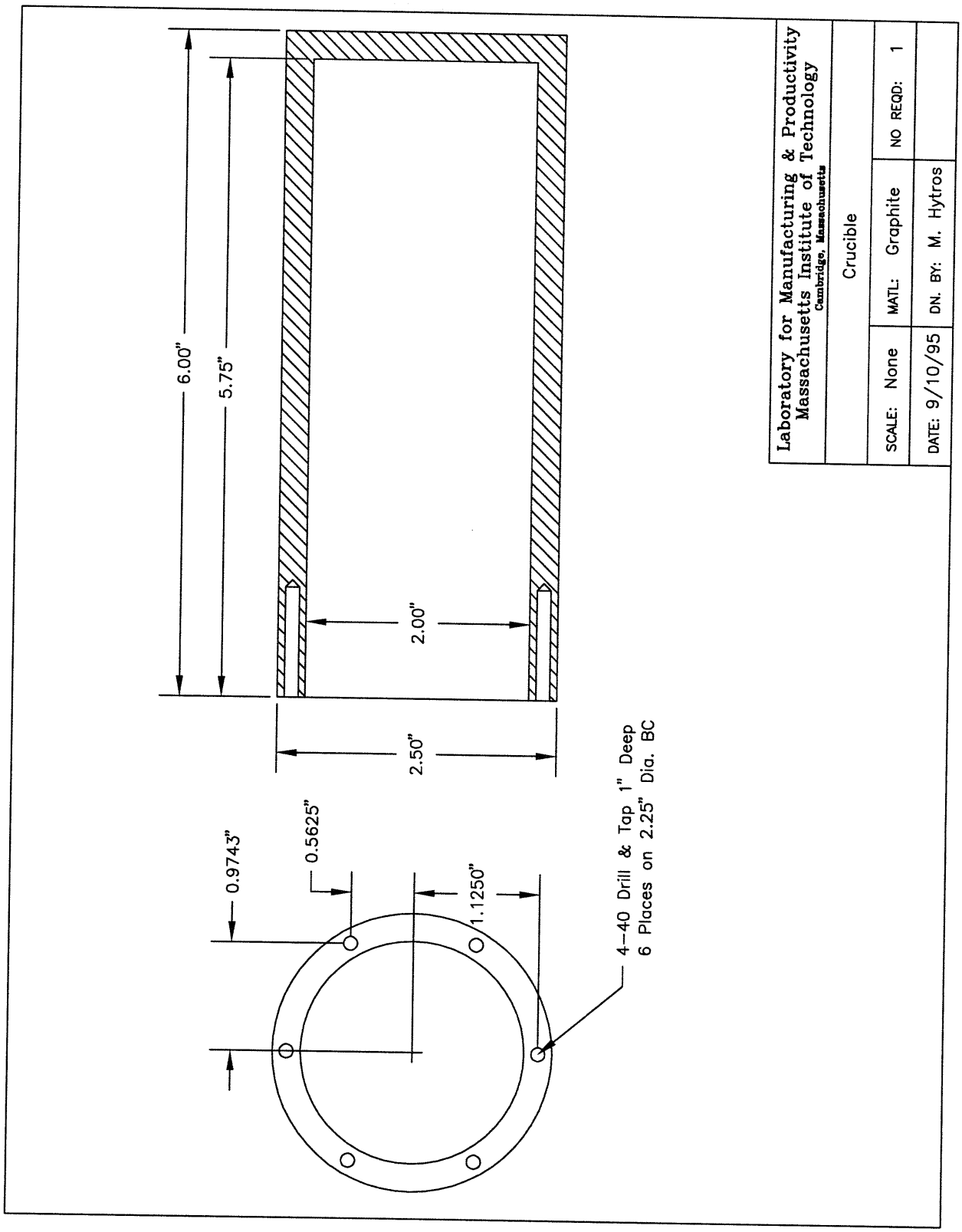

Figure D-8: Detail Drawing of Melt Crucible

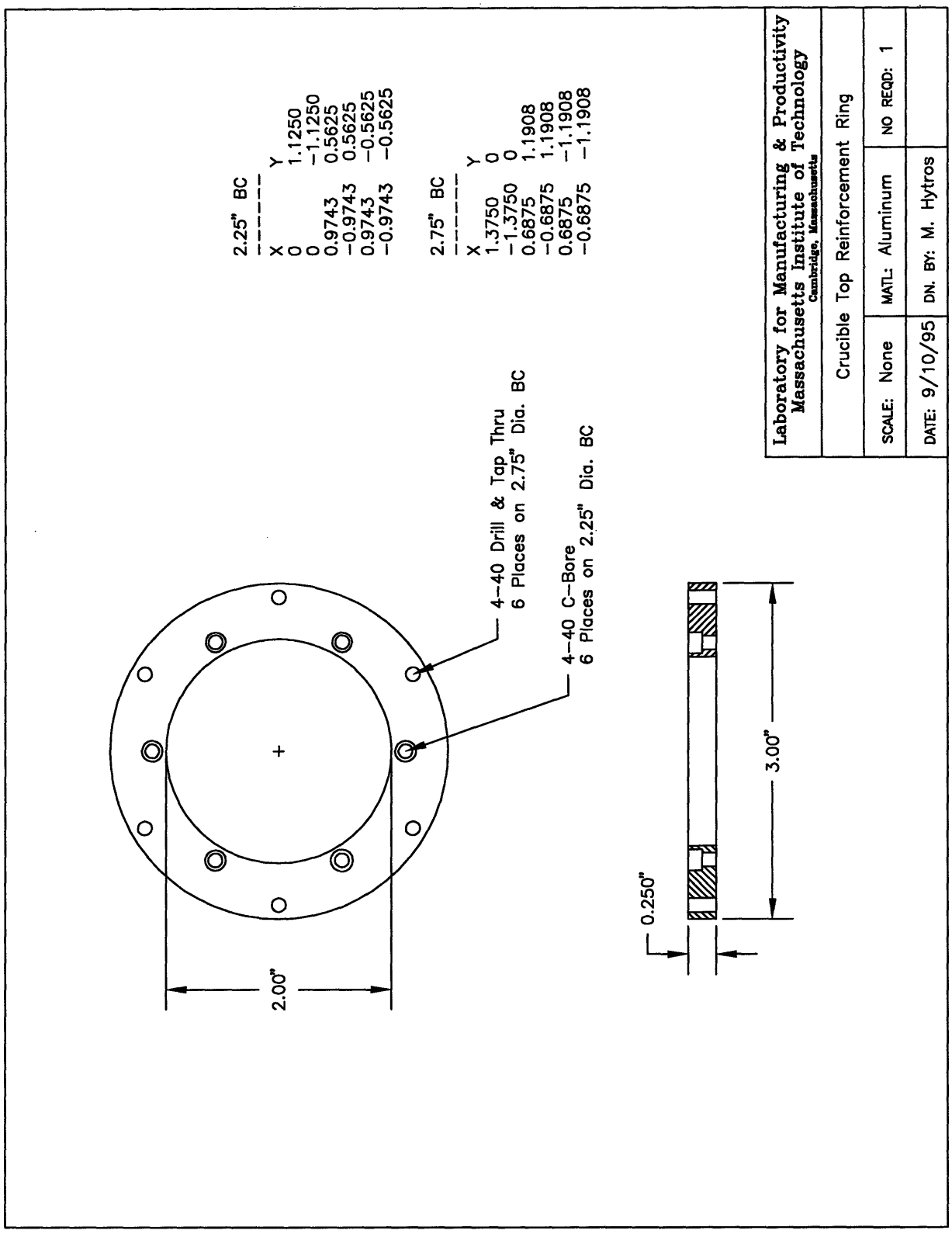

Figure D-9: Detail Drawing of Crucible Reinforcement Ring

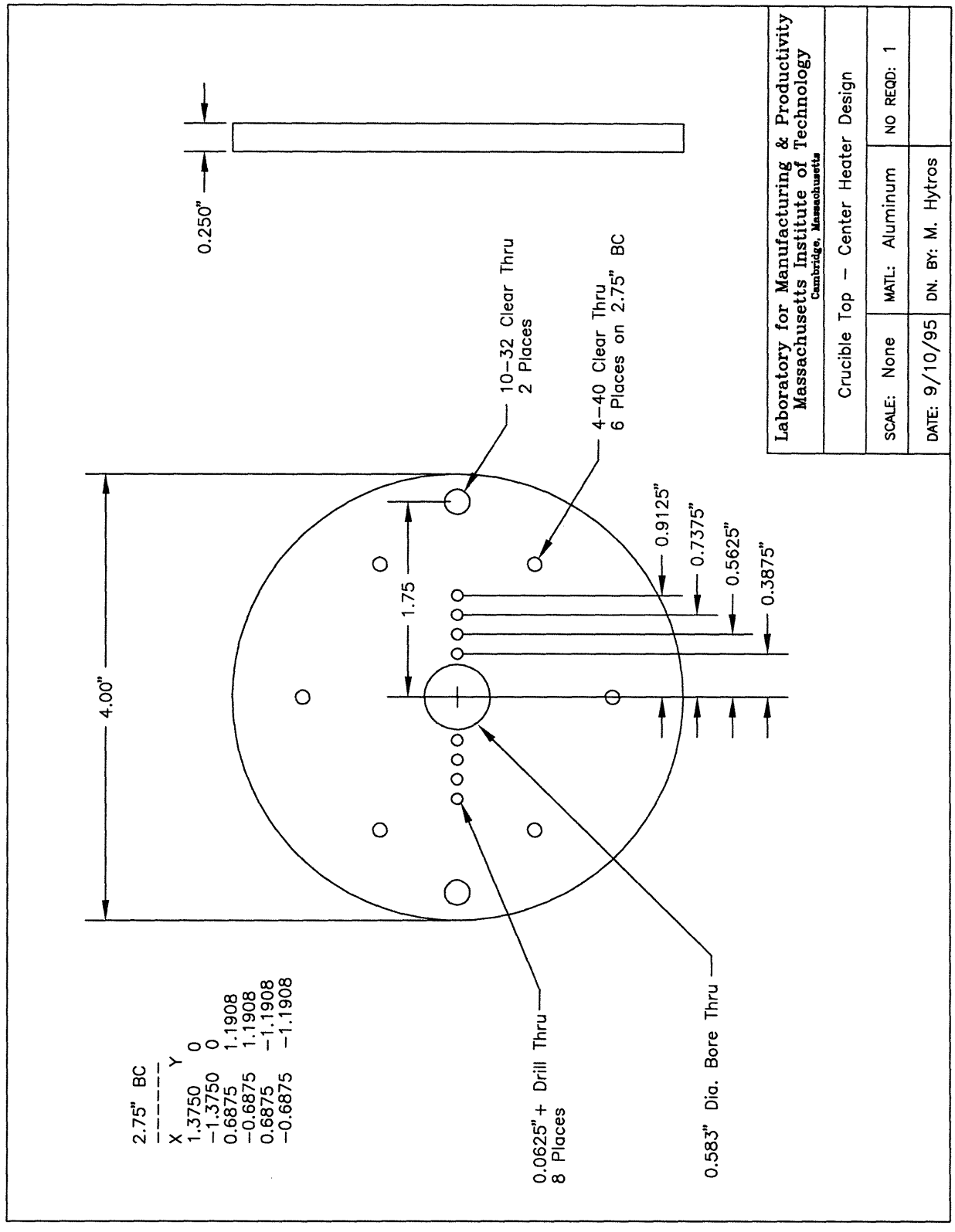

Figure D-10: Detail Drawing of Crucible Top - Center Heater Design

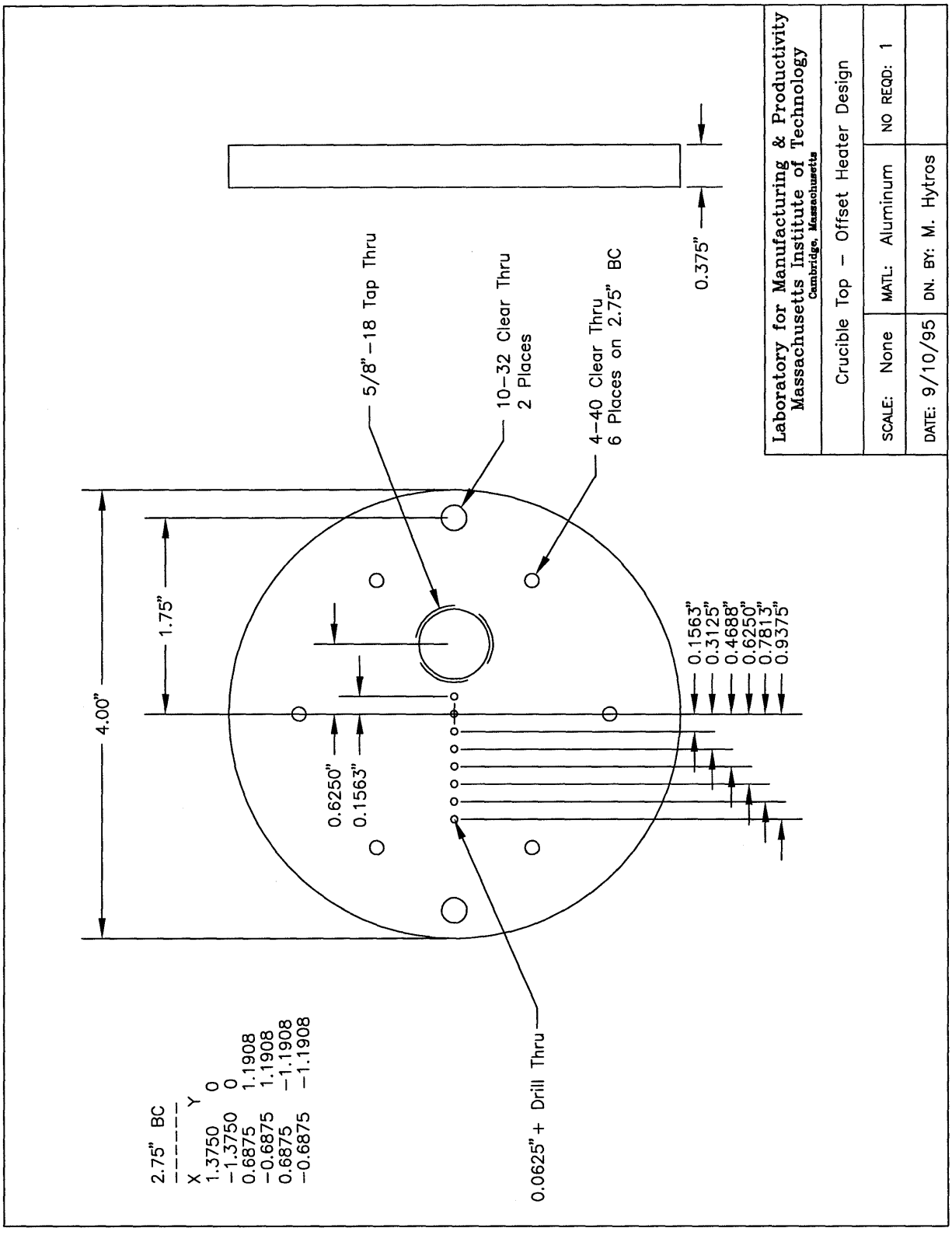

Figure D-11: Detail Drawing of Crucible Top - Offset Heater Design

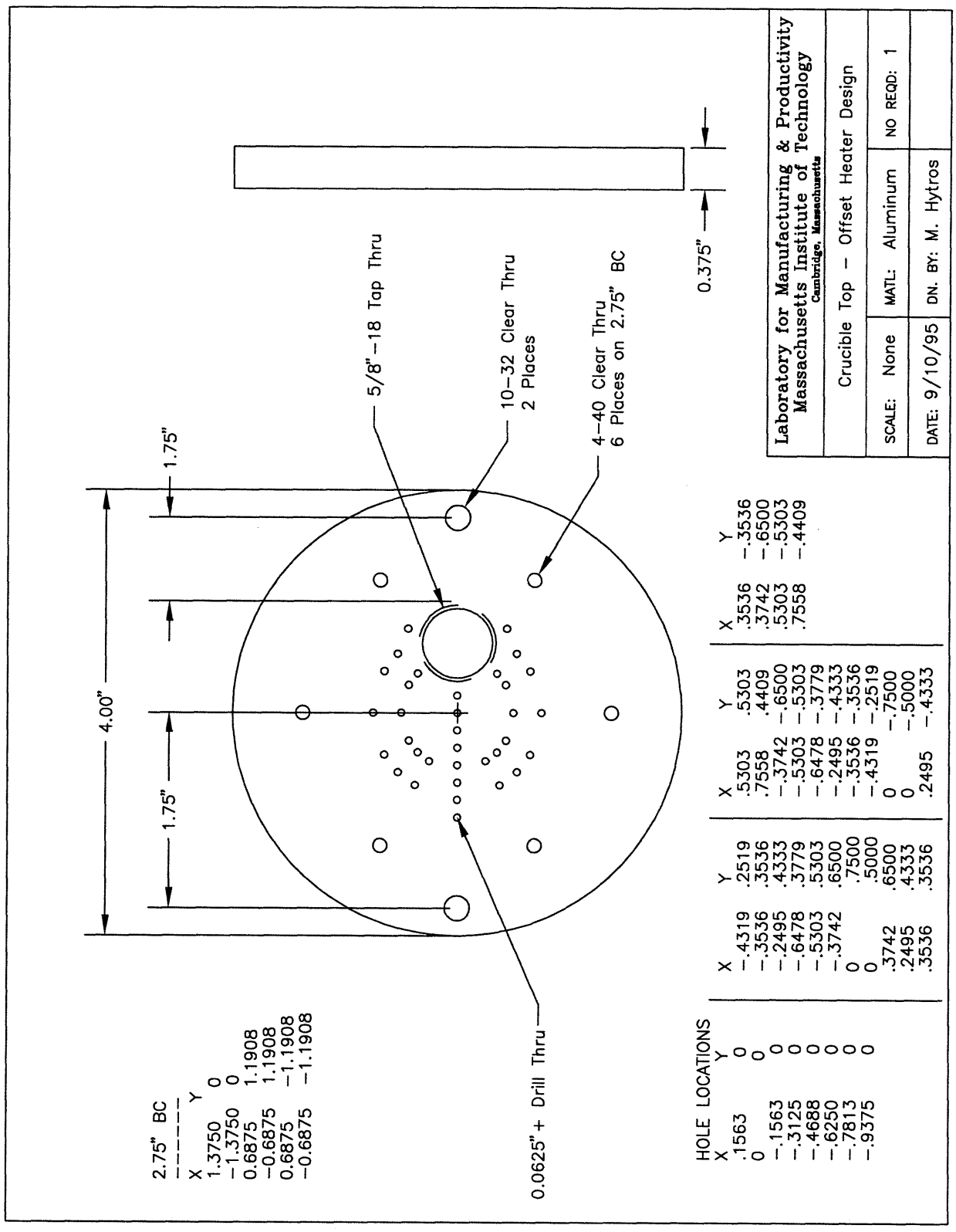

Figure D-12: Detail Drawing of Crucible Top - Modified Offset Heater Design

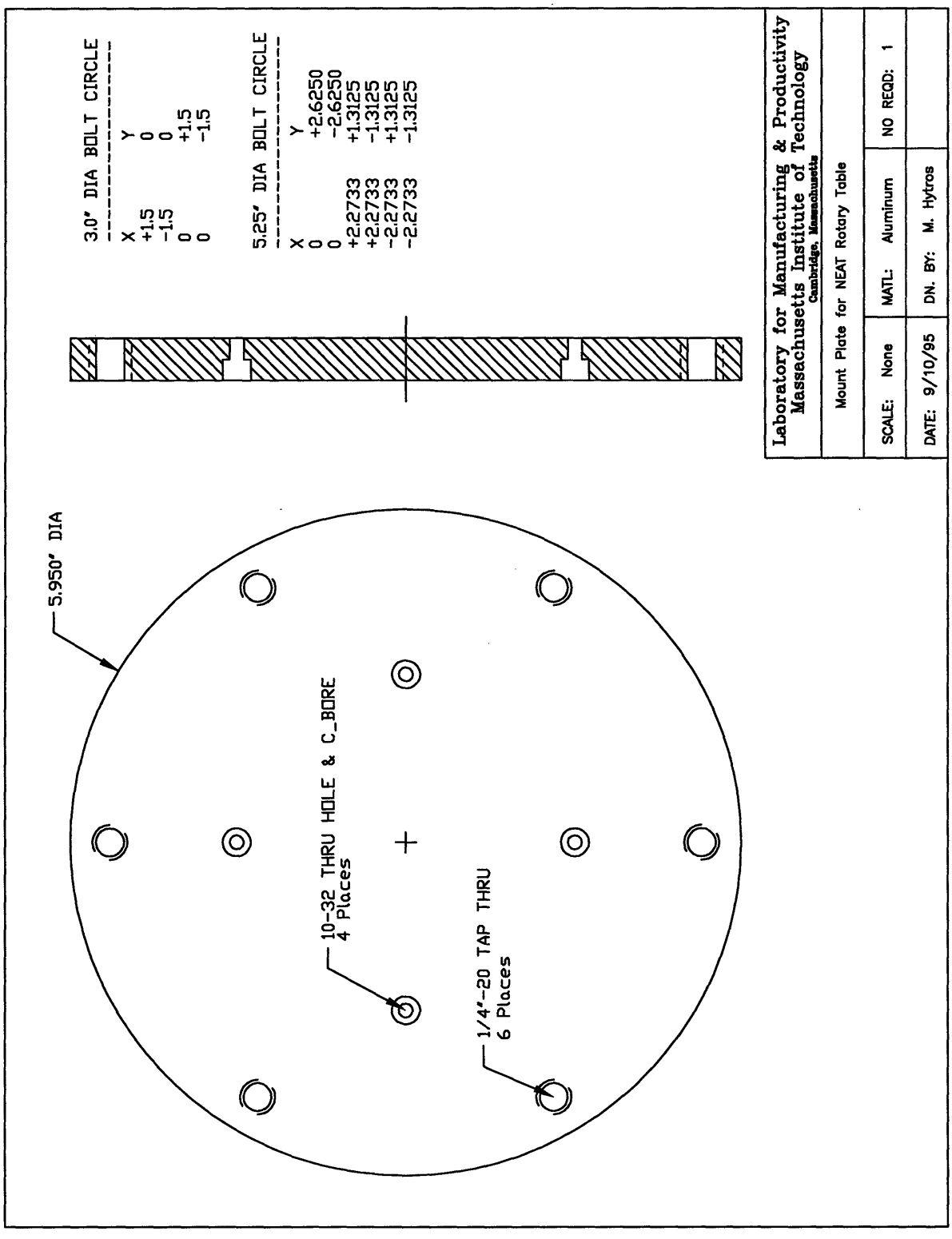

Figure D-13: Detail Drawing of Cooler Mount Plate

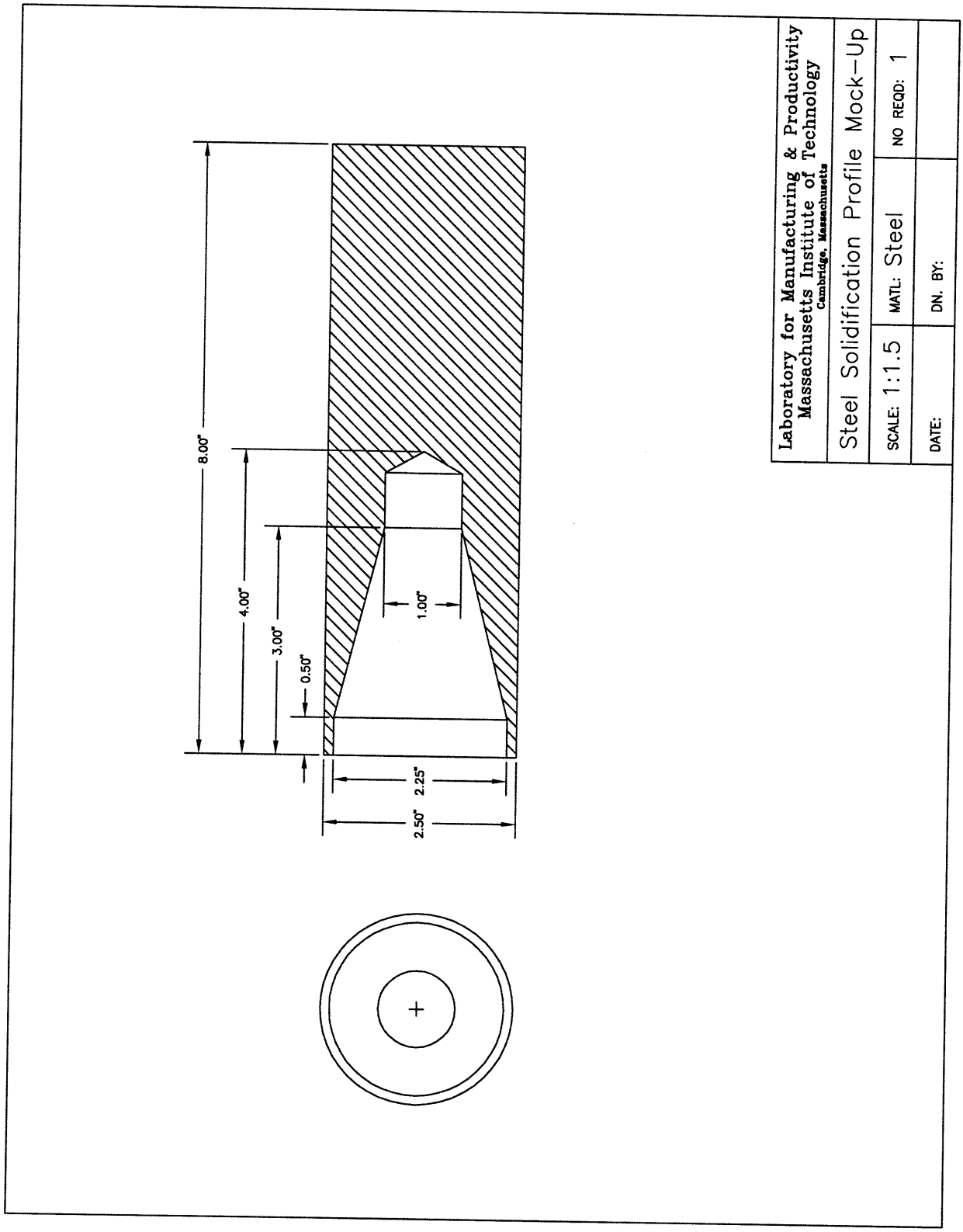

Figure D-14: Detail Drawing of Solidification Front Mock-Up

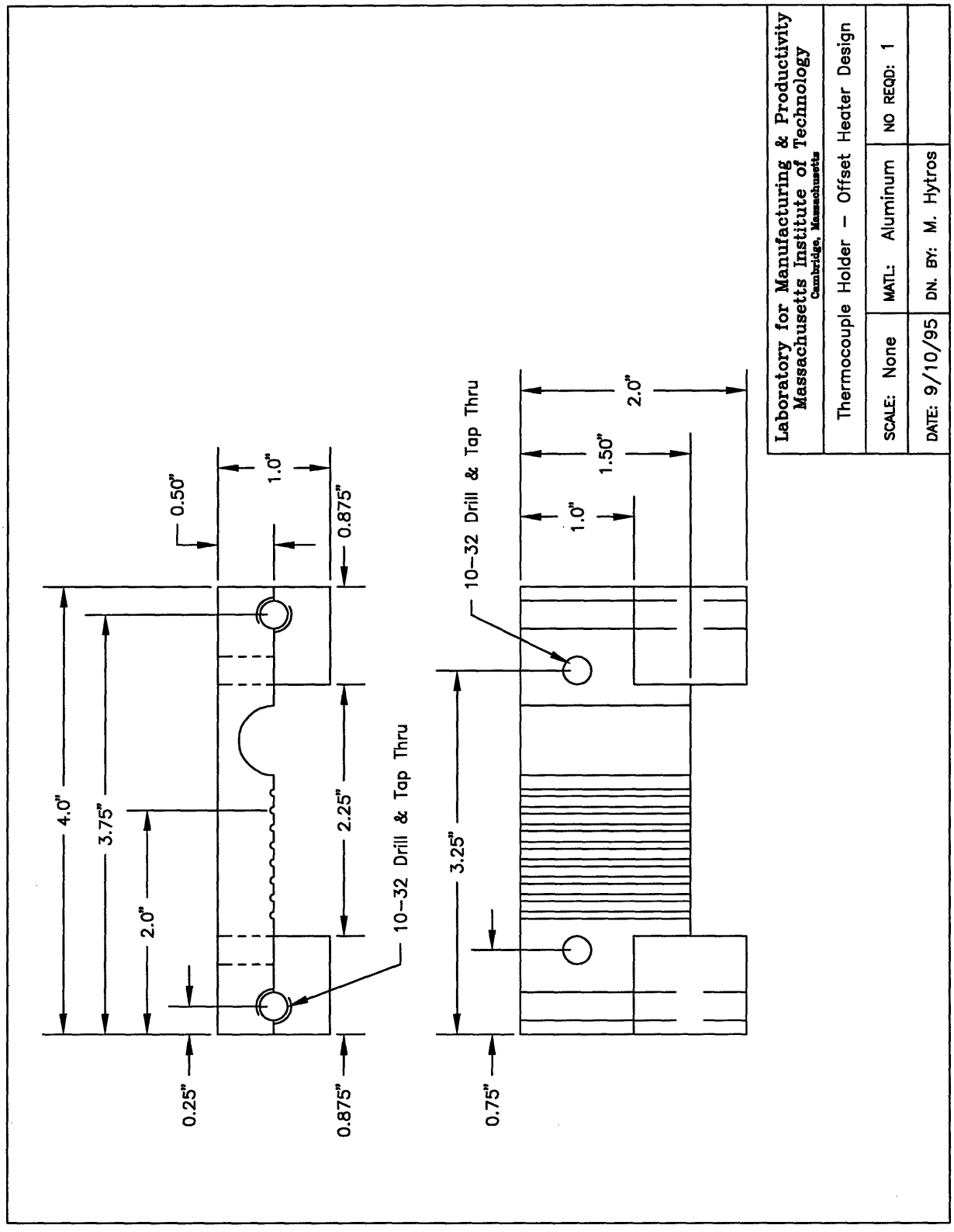

Figure D-15: Detail Drawing of Thermocouple Holder for Offset Heater Design

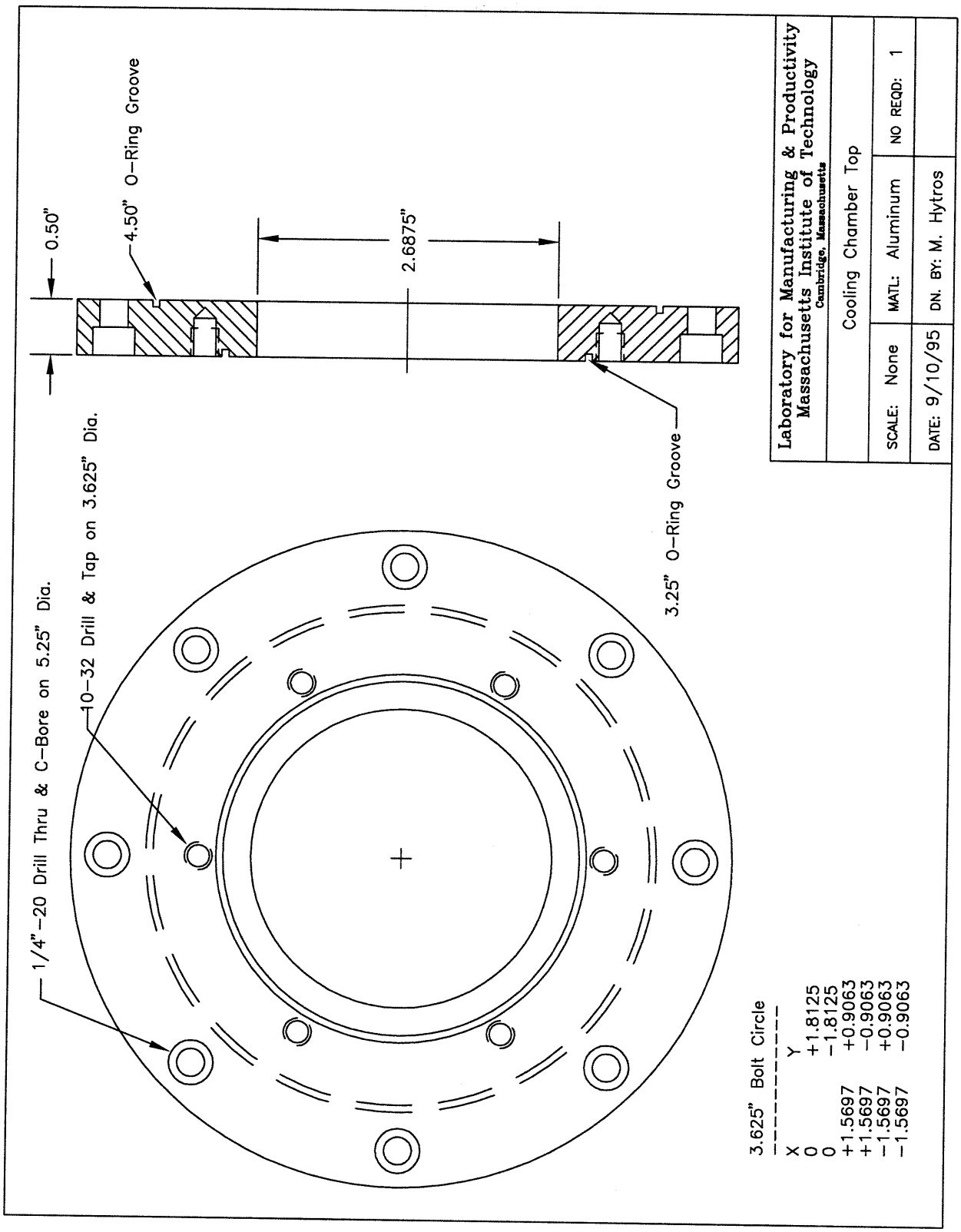

Figure D-16: Detail Drawing of Water Cooling Chamber Top Plate

Appendix E

Source Code for the Data Acquisition Programs

This appendix contains the source code for several data acquisition and manipulation programs which were used during the course of this research. They are:

- specter.c - Tomographic image data acquisition program,
- normalize.c - Tomographic image data normalization program, and
- theta.c - View angle manipulation program.

E.1 Tomographic Image Data Acquisition Program

This program is a motor control and data acquisition routine written in C and compiled using Microsoft C Version 5. This program controls the movement and records the output of a first-generation tomographic imaging system. The user inputs the linear and angular sample step increment, the photon sampling time per position, and the number of thermocouples to monitor. The program outputs an ASCII file with the measured photon count per position in the first column and the thermocouple readings per position in the remaining columns. The NuLogic PCMotion C library and Keithly-Metrabyte ASO-TC C library were used to implement the motor control and temperature recording portions of the program, respectively.

```
/* specter.c */
#include <c:/msc/include/sys/types.h>
#include <c:/msc/include/sys/timeb.h>
#include <c:/msc/include/limits.h>
#include <c:/msc/include/stdio.h>
#include <c:/msc/include/math.h>
#include <c:/msc/include/graph.h>
#include <c:/msc/include/time.h>
#include <c:/msc/include/io.h>
#include <c:/msc/include/conio.h>                                    10
#include <c:/msc/include/float.h>
#include <c:/hytros/pcMOTION.h> /* Header file for Motor Control */
#include <c:/hytros/userprot.h> /* Header file for Temperature Recording */
#define DASBASE 0X300  /* Address of Frequency counter board */
#define IP DASBASE+3
#define OP DASBASE+3
#define PROF_COMPL    0X400
#define MOTOR_OFF     0X04
#define MOTOR_RUNNING 0X80
/*****************/                                                  20
/* Function List */
/*****************/
double count_freq(int, float);
void setup_counter(int);
void setup_thermocouples(void);
int WaitForMoveComplete(WORD, WORD, BYTE, WORD);
void MoveAxis(DWORD, BYTE);
void SetUpMotors(void);
void Get_TC_Temps(int, int, FILE*, DDH);
/*****************/                                                  30
/* Main Function */
/*****************/
void main()
{
  FILE *ifp1; /* File pointer to output ascii file */
  DWORD i; /* Outer control loop for theta axis moves */
  DWORD j; /* Inner control loop for x axis moves */
  static DWORD x_step; /* Number of movements along x-axis */
```

```
static DWORD theta_step; /* Number of movements along theta-axis */
static DWORD X_CONV; /* Motor 1 parameter: steps per inch  */
static DWORD THETA_CONV; /* Motor 2 parameter: steps per degree */
static DWORD zeroPosX; /* Origin position of Motor 1 */
static DWORD zeroPosY; /* Origin position of Motor 2 */
static BYTE xAxis; /* Motor 1 axis number */
static BYTE yAxis; /* Motor 2 axis number */
static unsigned long int TarPosX; /* Target position of Motor 1 */
static unsigned long int TarPosY; /* Target position of Motor 2 */
static int err; /* Error status of temperature functions */
static int BoardNumber; /* Board number for temperature functions */
static int move; /* Current move number */
static int num_moves; /* Total number of moves */
static int temperature; /* Temperature of a thermocouple */
static double counts; /* Number of photon counts recorded */
static int refresh_rate; /* Frequency counter refresh rate */
static int count_time; /* Amount of time to record photon counts */
static int temp_num; /* Choice to perform temperature recording */
static int tc_low;  /* Starting thermocouple */
static int tc_high; /* Stopping thermocouple */
static double x_size; /* X move increment */
static double theta_size; /* Theta move increment */
static float refresh_hertz; /* Refresh rate in hertz */
static char NumberOfBoards; /* Number of temperature boards used */
DDH  DASTC_brd0; /* Handle for temperature board */
double run_time; /* Total run time for program */
double x_step2; /* Floating point value of x_step */
double theta_step2; /* Floating point value of theta_step */
double count_time2; /* Floating point value of count_time */
char filename[20]; /* Output ascii file name */
int retstat; /* Error status of motor control functions */
WORD BoardAddr; /* Motor controller board address */
WORD BoardType; /* Motor controller board type */

BoardAddr = 0X230;
BoardType = 2;
X_CONV = 2500UL;
THETA_CONV = 50UL;
xAxis = 1;
```

```
yAxis = 2;
refresh_rate = 2000;
BoardNumber = 0;                                                    80
/************************************/
/* Initialize the Thermocouple Board */
/************************************/
if((err=DASTC_DevOpen("DASTC.CFG", &NumberOfBoards))!=0){
  printf("\nError %d during TC Board Open.\n", err);
  exit(-1);
}
if((err=DASTC_GetDevHandle(BoardNumber, &DASTC_brd0))!=0){
  printf("\nError In TC Device Handle.\n");
  exit(-1);                                                         90
}
_clearscreen(_GCLEARSCREEN);
printf("Data Acquistion and Motor Control Program\n");
printf("=========================================\n");
printf("Input the count time duration [sec]:  ");
scanf("%d", &count_time);
printf("Input the step size in the x direction [inch] (0.01 min):  ");
scanf("%lf", &x_size);
printf("Input the number of movements in the x direction:  ");
scanf("%d", &x_step);                                               100
printf("Input the step size in the theta direction [degree] (0.1 min):  ");
scanf("%lf", &theta_size);
printf("Input the number of movements in the theta direction:  ");
scanf("%d", &theta_step);
temp_num=0;
while((temp_num>2) || (temp_num<1)){
  printf("Do you wish to record thermocouple readings?  [yes=1 no=2]:  ");
  scanf("%d", &temp_num);
}
if(temp_num == 1){                                                  110
  printf("Input the start thermocouple channel [1-16]:  ");
  scanf("%d", &tc_low);
  tc_low = tc_low - 1;
  printf("Input the stop thermocouple channel [1-16]:  ");
  scanf("%d", &tc_high);
  tc_high = tc_high - 1;
```

```
  if(tc_low >= tc_high){
    printf("\nStart TC must be lower than Stop TC.\n");
    printf("Input the start thermocouple channel [1-16]:  ");
    scanf("%d", &tc_low);
    tc_low = tc_low - 1;
    printf("Input the stop thermocouple channel [1-16]:  ");
    scanf("%d", &tc_high);
    tc_high = tc_high - 1;
  }
}
else{
  tc_high = 0;
  tc_low = 1;
}
printf("Input the output file name:  ");
scanf("%s",filename);
x_step2 = (double)x_step;
theta_step2 = (double)theta_step;
count_time2 = (double)count_time;
ifp1 = fopen(filename,"w");
refresh_hertz = 1e7/(float)refresh_rate/(float)refresh_rate;
setup_counter(refresh_rate);
run_time = x_step2*theta_step2*count_time2/3600;
printf("\nEstimated Run Time:  %1.2f hours\n\n", run_time);
fprintf(ifp1, "X: %d\t", x_step);
fprintf(ifp1, "THETA: %d\t", theta_step);
fprintf(ifp1, "TC: %d\n", (tc_high-tc_low+1));
SetUpMotors();
zeroPosX = 0;
zeroPosY = 0;
TarPosX = 0;
TarPosY = 0;
num_moves = theta_step*x_step;
move = 1;
for(i=0;i<theta_step;++i){
  MoveAxis(TarPosY, 2);
  for(j=0;j<x_step;++j){
    MoveAxis(TarPosX, 1);
    /* Get Frequency Count */
```

```
    counts = count_freq(count_time, refresh_hertz);
    /* Output to Screen */
    printf("Move %d", move);
    printf(" of %d", num_moves);
    printf("\tTheta:  %d", TarPosY);
    printf("\tX: %d", TarPosX);
    printf("\tCount:  %.0f\n", counts);
    /* Write Frequency Count to File */
    fprintf(ifp1, "%.0f\t", counts);
    /* Acquire and Write Thermocouple Temperatures */
    if(temp_num == 1){
      Get_TC_Temps(tc_low, tc_high, ifp1, DASTC_brd0);
    }
    fprintf(ifp1, "\n");
    TarPosX += (unsigned long int)(x_size*X_CONV);
    move += 1;
  }
  MoveAxis(zeroPosX, 1);
  TarPosX = 0;
  TarPosY += (unsigned long int)(theta_size*THETA_CONV);
 }
 MoveAxis(zeroPosX, 1);
 MoveAxis(zeroPosY, 2);
 _clearscreen(_GCLEARSCREEN);
 printf("\nData Acquisition Complete.\n");
 fclose(ifp1);
}
/************************************************/
/* Function to setup the frequency counter board */
/************************************************/
void setup_counter(int refresh)
{
 int xl;
 int xh;
 outp(0X300+15, 0X76);
 outp(0X300+15, 0XB6);
 xh = refresh/256;
 xl = refresh-256*xh;
 outp(0X300+13,xl);
```

```
  outp(0X300+13,xh);
  outp(0X300+14,xl);
  outp(0X300+14,xh);
}
/*************************************/
/* Function to return a frequency count */                                    200
/*************************************/
double count_freq(int count_time, float refresh_hertz)
{
  static int i;
  double counts;
  static int xl;
  static int xh;
  static double xl2;
  static double xh2;
  counts = 0;                                                                 210
  outp(0X300+12, 0XFF);
  outp(0X300+12, 0XFF);
  for(i=0; i<(count_time*refresh_hertz); i++){
    while(inp(0X300+3)&1);
    while(!(inp(0X300+3)&1));
  }
  outp(0X300+15,0X00);
  xl = inp(0X300+12);
  xh = inp(0X300+12);
  xl2 = (double)xl;                                                           220
  xh2 = (double)xh;
  counts = 65535-256*xh2-xl2;
  return counts;
}
/*********************************************************/
/* Function which waits for an axis to complete its move */
/*********************************************************/
int WaitForMoveComplete(WORD BoardAddr, WORD BoardType, BYTE Axis, WORD TimeOutSecs)
{
  int retstat;                                                                230
  WORD AxisStat;
  DWORD TimeOutCycles;
  DWORD i;
```

```
 if(TimeOutSecs>10000)
  return(-1);
 TimeOutCycles = 240*TimeOutSecs;
 AxisStat = 0;
 for(i=0; ((i<TimeOutCycles) || (TimeOutSecs==0)); i++){
  retstat = read_axis_stat(BoardAddr, BoardType, Axis, &AxisStat);
  if(retstat)                                                          240
   return (retstat);
  if( (AxisStat&(PROF_COMPL|MOTOR_OFF)) && (!(AxisStat&MOTOR_RUNNING)) )
   return 0;
 }
 return (-2);
}
/*************************************************/
/* Funtion to move a given axis to a given position */
/*************************************************/
void MoveAxis(DWORD Pos, BYTE Axis)                                    250
{
 static WORD TimeOutSecs;
 static WORD BoardAddr;
 static WORD BoardType;
 DWORD Present;
 int retstat;
 BoardAddr = 0X230;
 BoardType = 2;
 TimeOutSecs = 7200;  /* Two hour max wait time for move to complete */
 /* Check Which Axis Is Moving */                                      260
 if(Axis==2)
  Pos *= -1;
 /* Load Target Position */
 retstat = load_target_pos(BoardAddr, BoardType, Axis, Pos);
 if(retstat)
  printf("\nLoad Target Position Error.    Error # %d", retstat);
 /* Start Motor */
 retstat = start_motion(BoardAddr, BoardType, Axis);
 if(retstat)
  printf("\nStart Motion Error.    Error # %d", retstat);              270
 /* Wait For Move to End */
 retstat = WaitForMoveComplete(BoardAddr, BoardType, Axis, TimeOutSecs);
```

```
  if(retstat)
    printf("\nTime Out Error.     Error # %d", retstat);
  /* Read Present Position */
  retstat = read_pos(BoardAddr, BoardType, Axis, &Present);
  if(retstat)
    printf("\nRead Position Error.     Error # %d", retstat);
}
/*****************************************/                                    280
/* Function to setup the motor controller */
/*****************************************/
void SetUpMotors(void)
{
  int retstat;
  WORD BoardAddr;
  WORD BoardType;
  BYTE xAxis;
  BYTE yAxis;
  WORD PosMode;                                                               290
  WORD StopMode;
  WORD LoopMode;
  WORD MPDATA;
  DWORD StepsPerRev;
  DWORD VelX;
  DWORD VelY;
  DWORD AccelX;
  DWORD AccelY;
  WORD  AccelFact;
  LoopMode = 0X0000;                                                          300
  StopMode = 0X0001;
  PosMode = 0X0000;
  BoardAddr = 0X230;
  MPDATA = 0000000000000111;
  BoardType = 2;
  StepsPerRev = 200;
  xAxis = 1;
  yAxis = 2;
  VelX = 0X000002EE;
  VelY = 0X00000150;                                                          310
  AccelX = 0X00001F4;
```

```
AccelY = 0X0000050;
AccelFact = 0X000A;
/* Set Initial Zero */
retstat = reset_pos(BoardAddr, BoardType, xAxis);
if(retstat)
  printf("\nInitial Zero Set Error in X Axis.\n");
retstat = reset_pos(BoardAddr, BoardType, yAxis);
if(retstat)
  printf("\nInitial Zero Set Error in Y Axis.\n");                    320
/* Set Position Mode to Absolute Coords */
retstat = set_pos_mode(BoardAddr, BoardType, xAxis, PosMode);
if(retstat)
  printf("\nPosition Mode Set Error in X Axis.\n");
retstat = set_pos_mode(BoardAddr, BoardType, yAxis, PosMode);
if(retstat)
  printf("\nPosition Mode Set Error in Theta Axis.\n");
/* Set Stop Mode to Deceleration Stop */
retstat = set_stop_mode(BoardAddr, BoardType, xAxis, StopMode);
if(retstat)                                                           330
  printf("\nStop Mode Set Error in X Axis.\n");
retstat = set_stop_mode(BoardAddr, BoardType, yAxis, StopMode);
if(retstat)
  printf("\nStop Mode Set Error in Theta Axis.\n");
/* Set Loop Mode to Open Loop Control */
retstat = set_loop_mode(BoardAddr, BoardType, xAxis, LoopMode);
if(retstat)
  printf("\nLoop Mode Set Error in X Axis.\n");
retstat = set_loop_mode(BoardAddr, BoardType, yAxis, LoopMode);
if(retstat)                                                           340
  printf("\nLoop Mode Set Error in Theta Axis.\n");
/* Set Step Output Mode */
retstat = set_step_mode_pol(BoardAddr, BoardType, MPDATA);
if(retstat)
  printf("\nMode Polarity Set Error.\n");
/* Set Steps and Lines per Revolution */
retstat = load_steps_lines(BoardAddr, BoardType, xAxis, StepsPerRev);
if(retstat)
  printf("\nLine per Rev Error in X Axis.\n");
retstat = load_steps_lines(BoardAddr, BoardType, yAxis, StepsPerRev);  350
```

```
 if(retstat)
   printf("\nLine per Rev Error in Theta Axis.\n");
 /* Set Steps and Lines per Revolution */
 retstat = load_steps_lines(BoardAddr, BoardType, xAxis, StepsPerRev);
 if(retstat)
   printf("\nLine per Rev Error in X Axis.\n");
 retstat = load_steps_lines(BoardAddr, BoardType, yAxis, StepsPerRev);
 if(retstat)
   printf("\nLine per Rev Error in Theta Axis.\n");
 /* Load Velocity */                                                    360
 retstat = load_vel(BoardAddr, BoardType, xAxis, VelX);
 if(retstat)
   printf("\nLoad Velocity Error on X Axis.\n");
 retstat = load_vel(BoardAddr, BoardType, yAxis, VelY);
 if(retstat)
   printf("\nLoad Velocity Error on Theta Axis.\n");
 /* Load Acceleration */
 retstat = load_accel(BoardAddr, BoardType, xAxis, AccelX);
 if(retstat)
   printf("\nLoad Acceleration Error on X Axis.\n");                   370
 retstat = load_accel(BoardAddr, BoardType, yAxis, AccelY);
 if(retstat)
   printf("\nLoad Acceleration Error on Theta Axis.\n");
 /* Load Acceleration Factor */
 retstat = load_accel_fact(BoardAddr, BoardType, xAxis, AccelFact);
 if(retstat)
   printf("\nLoad Acceleration Factor Error on X Axis.\n");
 retstat = load_accel_fact(BoardAddr, BoardType, yAxis, AccelFact);
 if(retstat)
   printf("\nLoad Acceleration Factor Error on Y Axis.\n");           380
}
/*********************************************/
/* Function to Acquire Themocouple Temperatures */
/*********************************************/
void Get_TC_Temps(int tc_low, int tc_high, FILE* ifp1, DDH DASTC_brd0)
{
 static int k;
 static short int err;
 static float flag;
```

```
  static float temperature;                                          390
  flag = -999.99;
  for(k=tc_low; k<(tc_high+1); k++){
    err = K_ADRead(DASTC_brd0, k, 0, &temperature);
    if(err != 0)
      fprintf(ifp1, "%.2f\t", flag);
    else
      fprintf(ifp1, "%.2f\t", temperature);
  }
}
```

E.2 Tomographic Image Data Normalization Program

This program is a data normalization program which transforms the photon count data into a projection value, as defined by Equation 3.10. The program was written in ANSI-C on a Sun workstation and compiled using a GNU project C compiler. The program prompts the user for the name of the photon count ASCII data file and the number of transverse steps and view angles in the data set. The photon count data file should be a single column of numbers. For each view angle, the first and last photon count measurement in the data set are added together and averaged. This is the average of the "open-beam" photon count, and accommodates for drift in the measurements. Each photon count for a given view angle is then divided by this average "open-beam" count. The natural logarithm is taken and the result is multiplied by -1. The normalized data is then output to an ASCII data file which has the same name as the photon count data file with the addition of a "_FBP.dat" extension.

```
/* Frequency Normalization Program                          */
/* This program reads in an ASCII file of photon counts     */
/* and normalizes this data for each rotational position.   */
/* The first line of the data file should include the       */
/* number of x steps and theta steps used in the tomographic */
/* data collection.  The program outputs an ASCII data file */
/* with the filename of the input file plus an "FBP.dat"    */
/* extension.                                               */

/* Mark Hytros                                              */
/* Laboratory for Manufacturing and Productivity            */
/* October 4, 1995 */

#include <stdio.h>
#include <stdlib.h>
#include <string.h>
#include <math.h>

/*****************/
/* Main Function */
/*****************/
```

```
void main()
{
 FILE *ifp1;
 FILE *ofp1;
 char input_file[100];
 char output_file[200];
 char read_val[10];
 char extension[6];
 char *flag;
 int  i;
 int  j;
 int  x_steps;
 int  theta_steps;
 int  str_size;
 double **image_data;
 double read_num;
 double average_freq;
 double normal_freq;

 printf("\nIMAGE DATA NORMALIZATION PROGRAM");
 printf("\n================================");

 printf("\nName of input Image data file:  ");
 scanf("%s", input_file);
 ifp1 = fopen(input_file, "r");

 while(ifp1==NULL){
  printf("\nFILE NOT FOUND.  Try Again.");
  printf("\nName of input Image data file:  ");
  scanf("%s", input_file);
  ifp1 = fopen(input_file, "r");
 }

 flag = strchr(input_file, '.');
 str_size = strlen(input_file) - strlen(flag);
 flag = strncat(output_file, input_file, str_size);

 strcpy(extension, "_FBP.dat");
 strcat(output_file, extension);
```

```
ofp1 = fopen(output_file, "w");
fscanf(ifp1, "%s%d%s%d", read_val, &x_steps, read_val, &theta_steps);

/************************/
/* Read Data Into Matrix */
/************************/
image_data = calloc(theta_steps, sizeof(double *));
if (image_data == NULL){
  printf("\n\nMemory allocation error.\n\n");                    70
  exit(1);
}
for (i = 0; i < theta_steps; ++i){
  image_data[i] = calloc(x_steps, sizeof(double));
  if (image_data == NULL){
    printf("\n\nMemory allocation error.\n\n");
    exit(1);
  }
}
for (i = 0; i< theta_steps; ++i){                                 80
  for (j = 0; j < x_steps; ++j){
    if (fscanf(ifp1, "%lf", &read_num) == 1){
      image_data[i][j] = read_num;
    }
  }
}

/*******************************/
/* Normalize the Frequency Data */
/*******************************/                                 90
for(i = 0; i< theta_steps; i++){

  /* Average is the mean of the beam reading at the first and last positions in X */
  average_freq = (image_data[i][0] + image_data[i][x_steps-1])/2;

  for(j = 0; j< x_steps; j++){
    normal_freq =  (-1)*log((image_data[i][j])/average_freq);
    image_data[i][j] = normal_freq;
  }
}                                                                 100
```

```
  /**********************/
  /* Write Data to a File */
  /**********************/
  for(i = 0; i< theta_steps; i++){
    for(j = 0; j< x_steps; j++){
      fprintf(ofp1, "%f\n", image_data[i][j]);
    }
  }

                                                                    110

  free(image_data);
  fclose(ifp1);
  fclose(ofp1);
}
```

E.3 View Angle Manipulation Program

This program is a data manipulation program which transforms a photon count data set into a data set with a smaller number of view angles. The program was written in ANSI-C on a Sun workstation and compiled using a GNU project C compiler. The program prompts the user for the name of the photon count ASCII data file, the number of transverse steps, the number of view angles, and the new number of view angles, and the new data file name. The photon count data file should be a single column of numbers. The program deletes the extraneous view angles from the original data set and writes the new data set to a selected filename.

```
/* Theta Step Size Conversion Program                    */
/* This program takes an ASCII file of photon count data.    */
/* Given a photon count file with a given number of view angles,  */
/* this program manipulates and reduces the data into a user     */
/* selected lower number of view angles.                     */

/* Mark Hytros                                          */
/* Laboratory for Manufacturing and Productivity        */
/* November 17, 1995 */
                                                                10

#include <stdio.h>
#include <stdlib.h>
#include <string.h>
#include <math.h>

/*****************/
/* Main Function */
/*****************/

void main()                                                     20
{
  FILE *ifp1;
  FILE *ofp1;
  char input_file[100];
  char output_file[200];
  char read_val[10];
  int  i;
```

```
int j;
int x_steps;
int theta_steps;
int tc_num;
int theta_factor;
int new_count;
int conversion;
double **image_data;
double read_num;

theta_factor = 1;

printf("\nTHETA CONVERSION PROGRAM");
printf("\n========================");

printf("\nName of input Image data file:  ");
scanf("%s", input_file);
ifp1 = fopen(input_file, "r");

while(ifp1==NULL){
  printf("\nFILE NOT FOUND.  Try Again.");
  printf("\nName of input Image data file:  ");
  scanf("%s", input_file);
  ifp1 = fopen(input_file, "r");
}

printf("Name of output file name:  ");
scanf("%s", output_file);

ofp1 = fopen(output_file, "w");


fscanf(ifp1, "%s%d%s%d%s%d", read_val, &x_steps, read_val, &theta_steps, read_val, &tc_num);

printf("The number of angles is:  %d", theta_steps);
printf("\nHow many angles would like to convert to:  ");
scanf("%d", &theta_factor);
```

```
conversion = theta_steps/theta_factor;

if ((theta_steps%theta_factor)!=0){
  printf("Conversion must be an integer.");
  printf("\nHow many angles would like to convert to:  ");
  scanf("%d", &theta_factor);
}

fprintf(ofp1, "%s%d%s%d\n", "X: ", x_steps, " THETA: ", theta_factor);



/*************************/
/* Read Data Into Matrix */
/*************************/
image_data = calloc(theta_steps, sizeof(double *));
if (image_data == NULL){
  printf("\n\nMemory allocation error.\n\n");
  exit(1);
}
for (i = 0; i < theta_steps; ++i){
  image_data[i] = calloc(x_steps, sizeof(double));
  if (image_data == NULL){
    printf("\n\nMemory allocation error.\n\n");
    exit(1);
  }
}
for (i = 0; i< theta_steps; ++i){
  for (j = 0; j < x_steps; ++j){
    if (fscanf(ifp1, "%lf", &read_num) == 1){
      image_data[i][j] = read_num;
    }
  }
}

/*******************************/
/* Convert the angle step size */
/*******************************/
for(i = 0; i< theta_steps; i=i+conversion){
```

```
    for(j = 0; j< x_steps; j++){
      new_count = image_data[i][j];
      fprintf(ofp1, "%d\n", new_count);
    }
  }

  free(image_data);
  fclose(ifp1);
  fclose(ofp1);
}
```
